MOLECULAR BEAM EPITAXIALLY GROWN COPPER INDIUM DISELENIDE AND COPPER GALLIUM DISELENIDE FILMS

By

SEOKHYUN YOON

A DISSERTATION PRESENTED TO THE GRADUATE SCHOOL
OF THE UNIVERSITY OF FLORIDA IN PARTIAL FULFILLMENT
OF THE REQUIREMENTS FOR THE DEGREE OF
DOCTOR OF PHILOSOPHY

UNIVERSITY OF FLORIDA

2005

To my wife, Jeongyun Yang; and my children, Yeolim, Edward, and Jake.

Copyright 2005

by

Seokhyun Yoon

ACKNOWLEDGMENTS

The author would like to thank Drs. Oscar D. Crisalle, Fan Ren, Sheng S. Li and Paul Holloway for serving as supervisory committee and thoughtful advice. He would like to present his sincere gratitude to his committee chair, Dr. Timothy J. Anderson. His encouragement and insight into the research topic have been very helpful to the candidate throughout his study.

The author also wants to show his gratitude to his predecessors including Billy J. Stanbery, Suku Kim, and Serkan Kincal for their effort in constructing the PMEE system and for the preceding study on $Cu(In,Ga)Se_2$ materials. It was also a great pleasure for the author to work with colleagues including Woo Kyoung Kim, Ryan Kaczynski, Ryan Acher and other members in the photovoltaics group and Dr. Anderson's research group. The author would also like to thank Dr. Chinho Park, who provided photoluminescence measurements. He also wishes to express his appreciation to Mr. D. Vince and Mr. J. Hinnant for their kind support for his experiments and S. Gapinski for his support of the infrastructure at Microfabritech where the PMEE reactor is located. He also believes that the staff members in the departmental office deserve his gratitude. The author would like to thank the LG Chemical Research Park for the support during his doctorate study.

Finally, the author would like to thank his wife, Jeongyun Yang; his parents, Gumja Park and Sungjung Yoon; and his mother-in-law, Sukhee Ahn. Without their support, encouragement, and love, he could not have succeeded.

TABLE OF CONTENTS

Page

ACKNOWLEDGMENTS iv

LIST OF TABLES viii

LIST OF FIGURES xi

ABSTRACT xx

CHAPTER

1 INTRODUCTION 1

1.1 Theoretical Background 1
1.1.1 History of Solar Cells 1
1.1.2 Device Physics 3
1.1.3 $CuInSe_2$ and $CuGaSe_2$-based photovoltaic devices 7
1.1.4 Thermochemistry and structural properties of CIS or CGS materials 8
1.1.4.1 Chalcopyrite or α-CIS 11
1.1.4.2 Sphalerite or δ-CIS 13
1.1.4.3 β-CIS ($Cu_2In_4Se_7$ and $CuIn_3Se_5$) 14
1.1.4.4 CuAu-like CIS 14
1.1.5 Defects in chalcopyrite CIS or CGS 15
1.1.5.1 Defects in CIS 17
1.1.5.2 Defects in CGS 18
1.1.5.3 Comparison of defects in CIS and CGS 21
1.1.5.4 Na and CIGS 23
1.1.5.5 First principles calculation of defect energies 27
1.1.5.6 Summary of Defect States and Energy Levels in CIS and CGS 29
1.1.6 Review of the literature on the effects of grain boundaries (GBs) 31
1.1.6.1 Impact of GBs on CIGS cells 31
1.1.6.2 Studies on GB Effects using a One-Dimensional Model 32
1.1.6.2 Studies on GB Effects using a Two-Dimensional Model 35
1.1.7 GB models for CIGS cells 36
1.2 Experimental Methods 38
1.2.1 Reactor Specification 38
1.3 Scope of the Thesis work 40

2 EPITAXIAL GROWTH OF $CuInSe_2$ AT LOW TEMPERATURE 44

2.1 Backgrounds 44
2.2 Experimental Approach 45
2.3 Composition, Phase and Surface Morphology of Epitaxial Films 47
2.4 TEM Analysis of as-grown Epitaxial Films 59
2.5 Strain Analysis of Epitaxial CIS Film grown at Low Temperature 68
2.6 Summary and Conclusions 74

3 EPITAXIAL GROWTH OF $CuInSe_2$ AT HIGH TEMPERATURE 78

3.1 Introduction 78
3.2 Experimental Approach 79
3.3 Composition, Phase and Surface Morphology of CIS Films 80
3.3.1 EPMA Analysis 85
3.3.2 Cross-section SEM Images 89
3.4 XRD Analysis of CIS Films grown at High Temperature 90
3.4.1. XRD θ–2θ Scan and ω-rocking Curve Analysis of CIS Films Grown at High Temperature 90
3.4.2 Strain Analysis of CIS Films Grown at High Temperature 93
3.5 TEM Analysis of CIS Films Grown at High Temperature 96
3.5.1 TEM Analysis of Cu-rich CIS Film (W558) 97
3.5.2 TEM Analysis of In-rich CIS Film (W560) 102
3.5.3 TEM Analysis of Cu-rich and Na-dosed CIS film (W584) 106
3.5.4 TEM Analysis of In-rich and Na-dosed CIS film, W590 111
3.6 Summary and Conclusions 114

4 EPITAXIAL GROWTH OF $CuGaSe_2$ AT HIGH TEMPERATURE 117

4.1 Introduction 117
4.2 Experimental Approach 118
4.3 Composition, Phase and Surface Morphology of CGS Films 119
4.3.1 EPMA Analysis 124
4.3.2 Cross-section SEM Images 126
4.4 XRD Analysis of CGS Films grown at High Temperature 128
4.4.1 XRD θ–2θ Scan and ω-rocking Curve Analysis of CGS Films Grown at High Temperature 128
4.4.2 Strain Analysis of CGS Films grown at High Temperature 131
4.5 TEM Analysis of CGS Films Grown at High Temperature 133
4.5.1 TEM Analysis of Cu-rich CGS Film (W552) 134
4.5.2 TEM Analysis of Ga-rich CGS Film (W567) 140
4.5.3 TEM analysis of CIS film W583 144
4.6 Summary and Conclusions 148

5 STUDY OF DEFECT STRUCTURE BY PHOTOLUMINESCENCE SPECTROSCOPY 152

5.1 Introduction....152
5.2 Theoretical Background....153

5.3 Experimental Approach....157
5.4 PL Measurement of Epitaxial CGS Films....158
5.4.1 PL Spectra....158
5.4.2 Thermal Quenching of PL Peaks....167
5.4 Summary and Conclusions....170

6 STUDY OF GRAIN BOUNDARY EFFECTS IN CIS SOLAR CELLS....174

6.1 Theoretical Background....174
6.2 Electrostatics of p-n Junction Solar Cells....174
6.3 One-dimensional Simulation....179
6.3.1 Reference Case (CIS-1)....182
6.3.2 Impact of Deeper Acceptor and Compensating Donors in CIS Layer....183
6.3.3 Impact of Electron and Hole Traps and Recombination Center in the CIS Layer....184
6.3.4 Impact of Grain Boundaries....186
6.4 Two-Dimensional Simulation....189
6.4.1 The GB Effect of the Square Rectangular Grain....189
6.4.2 Effect of the GB orientation....205
6.4.2 Effect of the Junction Depletion Region on the GB Effect....210
6.5 Summary and Conclusions....216

7 CONCLUSIONS....212

7.1 Epitaxial Growth of $CuInSe_2$ at Low Temperature....220
7.2 Epitaxial Growth of $CuInSe_2$ and $CuGaSe_2$ at High Temperature....222
7.3 Photoluminescence Study of Epitaxial $CuGaSe_2$ Films....225
7.4 Study of the Grain Boundary Effect on $CuInSe_2$ Solar Cell....226

LIST OF REFERENCES....230

BIOGRAPHICAL SKETCH....237

LIST OF TABLES

Table page

1-1. Defect states and energy level above the valence band and formation energy for acceptors in CIS 29

1-2. Defect states and energy level below the conduction band and formation energy for donors in CIS....31

1-3. Defect states and energy level above the valence band and formation energy for acceptors in CGS....31

1-4. Defect states and energy level below the conduction band and formation energy for donors in CGS 31

2-1.Bulk composition of three CIS films on Mo-coated glass determined by ICP. 74

2-2 EPMA analysis for the matrix and island regions of each CIS film grown on (100) GaAs substrates. 50

2-3. EPMA analysis for the matrix and island region of each CIS film grown on (100) GaAs after etching in 10% KCN....52

2-4. Theoretical peak positions for GaAs : Space group (Fm-3m), $\lambda = 1.54056$Å 74

3-1. Bulk composition of CIS films on Mo-coated glass determined by ICP. 83

3-2. EPMA analysis for the matrix and island region of CIS film 88

3-3. ω, 2θ,φ and psi values for the GaAs (224) plane and CIS (228) plane....96

3-4. Lattice constants and lattice mismatch with GaAs for each CIS film....97

3-5. Lattice parameters of GaAs and CIS calculated from SADP at [1 -1 0] zone axis for Cu-rich CIS film (W558) 100

3-6. Lattice parameters of GaAs and CIS region for In-rich CIS film (W560) calculated from SADP at [-1 1 0] zone axis....104

3-7. Assignment of diffraction spots of In-rich CIS film (W560) for the region near the interface. 105

3-8. Lattice parameters of GaAs and CIS region for In-rich CIS film (W560) near the interface calculated from SADP at [-1 1 0] zone axis....105

3-9. Lattice parameters of GaAs and CIS calculated from SADP at [-1 0 3] zone axis..109

3-10. Lattice parameters of GaAs and CIS calculated from SADP at [-1 0 3] zone axis λL = 20.65....110

3-11. Lattice constants of GaAs and CIS calculated from SADP at [0 1 -1] zone....113

4-1. Bulk composition of CGS films grown on Mo-coated glass determined by ICP 120

4-2 EPMA analysis for the matrix and the island region of CGS film....123

4-3. (ω, 2θ,φ, psi) values for the GaAs (224) plane and CGS (228) plane....130

4-4. Lattice constants and lattice mismatch with GaAs for each CGS film....130

4-5. Lattice parameters of Cu-rich CGS film (W552) calculated from SADP at [-1 -1 2] zone axis....133

4-6. Lattice parameters of island top region calculated from SADP at [-1 -1 2] zone axis... 134

4-7. Lattice parameters calculated from SADP at [1 -1 0] zone axis in Figure 4-24....140

4-8. Lattice parameters calculated from SADP at [0 1 -1] zone axis....143

4-9. Lattice parameters calculated from SADP at [0 1 -1] zone axis....144

5-1. Peak energies and their assignments observed in CGS films in this study....170

5-2. Peak energies and their assignments observed in CGS films after Se annealing in this study....170

6-1. The electrical properties of each layer in the device....179

6-2. Properties of each cell for the study of the compensation effect....183

6-3. Performances for different acceptor level and for compensating donors....183

6-4. Properties of each cell for the study of the effect of traps....184

6-5. Performance of each solar cell for the study of the effect of traps....186

6-6. The length of the depletion region in the CIS layer and built-in potential in each doping ratio....211

6-7. The parameters for the calculation of the depletion region in the CIS with heterojunctions equations 212

6-8. The length of the depletion region in the CIS layer and built-in potential in each doping ratio with heterojunctions equations 212

LIST OF FIGURES

Figure page

1-1. Transport of carriers in p-n junction diode solar cell 4

1-2. I-V curve with and without light 5

1-3. Assessed phase diagram along the Cu_2Se-In_2Se_3 pseudobinary section of the Cu-In-Se system [Cha96a] 9

1-4. Assessed phase diagram along the Cu_2Se-Ga_2Se_3 pseudobinary section of the Cu-Ga-Se system [Ide03] 10

1-5. Unit cell of $CuInSe_2$ with chalcopyrite structure 12

1-6. Sphalerite and Cu-Au like structures of $CuInSe_2$: (a) Sphalerite structure, (b) Cu-Au like structure. Note the Se atoms are not shown in these schematics. 13

1-7. Inside view of the MEE reactor 39

1-8. Schematic diagram of the each zone in the reactor 40

2-1.SEM images of the surface of the In-rich sample Cu/In = 0.98 (W366): (a) 3,000X, (b) island region at 30,000X 48

2-2. SEM images of the surface of the In-rich sample Cu/In = 1.02 (W369):(a) 3000X, (b) island region at 30,000X 48

2-3. SEM images of the surface of the Cu-rich sample Cu/In = 1.09 (W367):(a) 3,000X, (b) island region at 30,000X 49

2-4. SEM images of the surface of the Cu-rich sample Cu/In = 0.98 (W366) after etching in 10 % KCN. (a) 3,000X, (b) island region at 30,000X 51

2-5. SEM images of the surface of the Cu-rich sample Cu/In = 1.02 (W369) after etching in 10 % KCN: (a) 3,000X, (b) island region at 30,000X 51

2-6. SEM image of the surface of the Cu-rich sample Cu/In = 1.09 (CIS3) after etching in 10 % KCN: (a) 3,000X, (b) island region at 30,000X 51

2-7. SEM images for the cross-section of the Cu-rich sample with Cu/In = 0.98 (W366):(a) 5,000X, (b) island region at 20,000X 53

2-8. SEM images of the cross-section of the Cu-rich sample with Cu/In = 1.02 (W369):(a) 5,000X, (b) island region at 20,000X....53

2-9 SEM images of the cross-section of the Cu-rich sample with Cu/In = 1.09 (W367):(a) 5,000X, (b) island region at 20,000X....54

2-10. XRD ω – 2θ scan of In-rich sample with Cu/In=0.98 (W366) after etching with 10% KCN....54

2-11. XRD ω – 2θ scan of Cu-rich sample with Cu/In=1.02 (W369) after etching with 10% KCN....55

2-12. XRD ω – 2θ scan of Cu-rich sample with Cu/In=1.09 (W367) after etching with 10% KCN....55

2-13. XRD ω–rocking curve for (008) plane of Cu-rich samples, W369 and W367 after etching with 10% KCN....56

2-14. XRD ω – 2θ scan of Cu-rich sample with Cu/In=1.09 (W367) before KCN etching 57

2-15. Grazing incidence XRD 2θ scan of Cu-rich sample W367 after etching with 10% KCN, ω = 0.4°: (a) GaAs (111) (b) CH-CIS (112)....58

2-16. Pole figure of Cu-rich sample with Cu/In=1.09 (CIS3) after etching with 10% KCN 59

2-17. TEM cross-sectional images of the Cu-rich sample with Cu/In=1.09 (W367):(a) Dark field image of island region, (b) Dark field image of matrix region....60

2-18. Dark field image of region A....62

2-19. TEM-EDX line scan of region A....62

2-20. Dark field image of region C....63

2-21. TEM-EDX line scan of region C....63

2-22. Dark field image of region B....64

2-23. TEM-EDX line scan of region B....64

2-24. Dark field image of region D....65

2-25. TEM-EDX line scan of region D....65

2-26. Dark field image of region....66

2-27. TEM-EDX line scan of region E 66

2-28. Selected area diffraction pattern for the (a) matrix and (b) island regions: (a) Matrix region:B = [-1-10], (b) island region: B = [-1-10] 67

2-29. Relation between X-ray and film in real space and the reciprocal space 69

2-30. Space map for (2 2 4) plane of GaAs and (2 2 8) plane of CIS for CU-rich CIS (sample W367) 71

2-31. ω/2θ rocking curves for (2 2 8) plane of Cu-rich sample W367 and (2 2 4) plane of GaAs at $\phi = \phi_0 + 0°$ and $\phi = \phi_0 + 180°$ 73

2-32. Suggested growth mechanism of Cu-rich CIS films (W367, W369) 74

3-1. Element depth profiles of the In-rich, Na-dosed CIS sample (W590) 81

3-2. SEM image of the surface of the Cu-rich CIS film (W558, Cu/In = 1.10): (a) 500X, (b) island region at 10,000X 82

3-3. SEM image of the surface of the In-rich CIS film (W560, Cu/In = 0.99): (a) 500X, (b) island region at 10,000X 83

3-4. SEM image of the surface of the Cu-rich, Na dosed CIS film (W584, Cu/In = 1.10): (a) 1,000X, (b) island region at 10,000X 83

3-5. AFM image of the surface of the In-rich CIS film with Na dosing (W590, Cu/In = 0.9): (a) 10 μm×10 μm, (b) 1 μm×1 μm 83

3-6. SEM image of the surface of the Cu-rich CIS film (W558, Cu/In = 1.10) after etching: (a) 3,000×,(b) island region at 10,000× 87

3-7. SEM image of the surface of the In-rich CIS film (W560, Cu/In = 0.99) after etching: (a) 3,000X, (b) island region at 30,000X 87

3-8. SEM image of the surface of the Cu-rich CIS film with Na dosing (W584, Cu/In = 1.10) after etching: (a) 1,000X, (b) island region at 10,000X 88

3-9. AFM images of the surface of the In-rich CIS film with Na dosing (W590, Cu/In = 0.9) after KCN etching: (a) 10 μmX10 μm, (b) 1 μmX1 μm 88

3-10. SEM cross-sectional images of CIS films without Na-dosing: (a) Cu-rich CIS film (W558, Cu/In = 1.10), (b) In-rich CIS film (W560, Cu/In = 0.99) 89

3-11. SEM cross-sectional images of CIS films with Na-dosing: (a) Cu-rich CIS film (W584, Cu/In = 1.09), (b) In-rich CIS film (W590, Cu/In = 0.90) 90

3-12. XRD θ – 2θ scan of CIS films. 91

3-13. XRD θ – 2θ scan of In-rich CIS film (W560) after KCN etching. 92

3-14. ω-rocking curve of (008) plane of CIS films and (400) plane of GaAs 94

3-15. Lattice constants of each CIS film in the reciprocal space....96

3-16. SADP of GaAs substrate and CIS region of Cu-rich CIS film (W558) at zone axis [1 -1 0]: (a) GaAs, (b) CIS 98

3-17. SADP at the interface of Cu-rich CIS film (W558) at zone axis [-1 1 0] 100

3-18. Dark field image by using g = (0 0 -4) diffraction vector at 50,000X magnification: (a) island region, (b) matrix region 101

3-19. SADP for one grain and many grains in island region at zone axis [1 -1 0]: (a) For one grain, (b) For many grains 101

3-20. SADP of GaAs substrate and CIS region for In-rich CIS film (W560) at zone axis [-1 1 0]: (a) GaAs, (b) CIS 102

3-21. SADP near the interface between CIS film and GaAs substrate, W560 103

3–22. Bright field and dark field image of W560 by using g = (0 0 -4): (a) Bright field image, (b) Dark field image 105

3-23. Bright field image of the TEM-EDX scan region near the interface for In-rich CIS film (W560) 105

3-24. TEM-EDX line scan of In-rich CIS film (W560) near the interface....106

3-25. Bright field image of the Cu-rich CIS film with Na-dosing (W584): (a) Bright field image of island structure, (b) Bright field image of matrix region 107

3-26. SADP of GaAs and matrix region of W584 at [-1 0 3]: (a) SADP of GaAs, (b) SADP of matrix region....107

3-27. SADP of W584 at the interface between GaAs and CIS film at [-1 0 3]. 108

3-28. SADP of island region of Cu-rich CIS film with Na-dosing (W584) at [-1 1 2] zone axis: (a) SADP of island top region ($Cu_{1.5}Se$), (b) SADP of island bottom region (CIS) 109

3-29. TEM-EDX line scans of W584 along the depth of the island structure 110

3-30. Dark field image of In-rich CIS film with Na-dosing (W590): g = (0 2 2): (a) Dark field image: Island (50,000X), (b) Dark field image: Matrix (100,000X) 111

3-31. SADP of GaAs and matrix region of In-rich CIS film with Na-dosing (W590) at [0 1 -1] zone axis: (a) SADP of GaAs, (b) SADP of CIS matrix region 112

3-32. SADP of In-rich CIS film with Na-dosing (W590) at the interface between GaAs and CIS film. 113

3-33. SADP of island region of In-rich CIS film with Na-dosing (W590) ('T' means diffraction patterns from twins.) 114

4-1. Element depth profiles of the Ga-rich, Na-dosed CGS sample (W599) 122

4-2. SEM image of the surface of the Cu-rich CGS film (W552, Cu/Ga = 1.19): (a) 3,000X, (b) island region at 10,000X 122

4-3. SEM image of the surface of the Ga-rich CGS film (W567, Cu/Ga = 0.96): (a) 3,000X, (b) island region at 10,000X 123

4-4. SEM image of the surface of the Cu-rich CGS film with Na-dosing (W583, CuGa=1.22): (a) 1,000X, (b) island region at 10,000X 123

4-5. SEM image of the surface of the Ga-rich CGS film with Na-dosing (W599, Cu/Ga = 0.81): (a) 3,000X, (b) island region at 10,000X 123

4-6. SEM image of the surface of the Cu-rich CGS film (W552, Cu/Ga=1.19) after etching: (a) 3,000X, (b) island region at 20,000X 125

4-7. SEM image of the surface of the Ga-rich CGS film (W567, Cu/Ga=0.96) after etching: (a) 3,000X, (b) island region at 20,000X 125

4-8. SEM image of the surface of the Cu-rich CGS film with Na-dosing (W583, Cu/Ga=1.22) after etching: (a) 1,000X, (b) island region at 10,000X 126

4-9. SEM image of the surface of the Ga-rich CGS film with Na-dosing (W599, Cu/Ga = 0.81) after etching: (a) 3,000X, (b) 10,000X 126

4-10. SEM cross-sectional images of CGS films: (a) Cu-rich CGS film (W552, Cu/Ga = 1.19), (b) Ga-rich CGS film (W567, Cu/Ga = 0.96) 127

4-11. SEM cross-sectional images of CGS films with Na-dosing: (a) Cu-rich CGS film (W583, Cu/Ga = 1.22), (b) Ga-rich CGS film (W599, Cu/Ga = 0.81) 127

4-12. XRD $\theta - 2\theta$ scan of CGS films (W552, W567, W583 and W599) 128

4-13. ω-rocking curve of (008) plane of CGS films and (400) plane of GaAs 130

4-14. Plot of lattice constants of CGS films in k-space 133

4-15. Z-contrast dark field image of the island region and the matrix region of W552: (a) island region, (b) matrix region 134

4-16. SADP of GaAs and the bottom part of the island structure for Cu-rich CGS film (W552) at zone axis [-1 -1 2]: (a) GaAs, (b) island bottom region (CGS) 134

4-17. SADP of the island top region and of the interface between island top and bottom regions at zone axis [-1 -1 2] for Cu-rich CGS film (W552): (a) island top region: Cu-Se phase, (b) interface between island top and bottom regions 136

4-18. SADP at two interface regions of Cu-rich CGS film (W552) at zone axis [-1 -1 2]: (a) SADP at the interface of island bottom and GaAs, (b) SADP at the interface of matrix and GaAs.....137

4-19. Z-contrast dark field image of Cu-rich CGS film (W552).....138

4-20. TEM-EDX line scan of the island structure of Cu-rich CGS film (W552).....139

4-21. TEM-EDX line scan near the interface region of Cu-rich, Na-free CGS film (W552) 139

4-22. TEM-EDX line scan at the interface between CGS film and GaAs for Cu-rich CGS film (W552).....140

4-23. Dark field image of Ga-rich CGS film (W567) with g = (200).....141

4–24. SADP of GaAs and matrix region at zone axis [-1 0 3] for Ga-rich CGS film (W567): (a) GaAs, (b) CGS region 141

4–25. SADP of GaAs and CGS region for Ga-rich CGS film (W567) at zone axis [1 -1 0]: (a) GaAs, (b) CGS region 142

4-26. SADP of spherical island structure in Ga-rich CGS film (W567): (a) SADP at [0 0 -1], (b) SADP at [1 -1 0].....143

4-27. Dark field image and SADP of interface region in Ga-rich CGS film (W567): (a) Dark field image by g = (2 0 0), (b) SADP at interface at zone axis [0 0 -1].....143

4-28. Dark field image of Cu-rich, Na-doped film (W583) by g (400).....144

4-29. SADP of Cu-rich CGS film with Na-dosing (W583) at [0 1 -1]: (a) GaAs region, (b) matrix region.....145

4-30. SADP of Cu-rich CGS film with Na-dosing (W583) at [0 1 -1]: (a) at interface between matrix and GaAs, (b) at island top region ($Cu_{1.5}Se$).....146

4-31. Observation of island region by dark field image and SADP of the top part of the island region for Cu-rich CGS film with Na-dosing (W583): (a) Dark field image of the island region: g = (400) (b) SADP of $Cu_{1.5}Se$ region.....147

5-1. PL spectrum of Cu-rich CGS film (W552) at 10 K.....159

5-2. PL spectrum of Ga-rich CGS film (W567) at 10 K.....159

5-3. PL spectrum of Cu-rich, Na doped CGS film (W583) at 10 K 160

5-4. PL spectrum of Ga-rich, Na doped CGS film (W599) at 10 K 160

5-5. PL spectrum of Cu-rich CGS film (S552) after Se annealing at 10 K 161

5-6. PL spectrum of Ga-rich CGS film (S567) after Se annealing at 10 K 161

5-7. PL spectrum of Cu-rich, Na dosed CGS film (S583) after Se annealing at 10 K 162

5-8. PL spectrum of Ga-rich, Na doped CGS (S599) after Se annealing at 10 K.....162

5-9. TEM-EDX line scan region of Cu-rich, Na-dosed CGS film (W583 164

5-10. TEM-EDX line scan of Cu-rich, Na doped CGS film (W583) before Se annealing ... 165

5-11. TEM-EDX line scan region of In-rich, Na-dosed CIS film (W590 165

5-12. TEM-EDX line scan of In-rich, Na dosed CIS film (W590) before Se annealing 166

5-13. Thermal quenching of PL peak at 1.647 eV from Cu-rich CGS films (W552) 167

5-14. Thermal quenching of PL peak at 1.646 eV from Cu-rich, Na doped CGS film (W583) 167

5-15. Thermal quenching of PL peak at 1.667 eV from Ga-rich CGS film (W567).....168

5-16. Thermal quenching of PL peak at 1.656 eV from Cu-rich, Na-dosed CGS film after Se annealing (S583) 168

6-1. Equivalent circuit of a p-n junction solar cell.....178

6-2. Solar spectrum for AM0 condition.....180

6-3. Absorption coefficient of each semiconductor layer in the device model 181

6-4. Dark and AM0 J-V curves of the reference cell, CIS-Ref.....182

6-5. Compensation effect by donor states in the absorber layer.....183

6-6. The effect of traps in the absorber layer.....185

6-7. Energy band diagrams near a grain boundary region in the p-type material with trap states before and after equilibrium is obtained.....186

6-8. Current-voltage characteristics of a solar cell with a grain boundary at the center of the absorber layer 188

6-9. Band diagram of the solar cell with a grain boundary at the center of the absorber layer with no illumination 188

6-10. Band diagram of the solar cell with a grain boundary at the center of the absorber layer with illumination 189

6-11. Consideration of grain boundaries in three-dimensional space 190

6-12. Simplification of grain boundaries solved in this study 191

6-13 Comparison of J-V characteristics for the case with (d = 200 nm) and without grain boundaries 193

6-14. Current flow line of the solar cell with grain boundaries (d = 200 nm), the length in width direction in this figure is exaggerated 194

6-15. Surface plot of the net carrier density (d= 200nm) 195

6-16. Surface plot of the potential for the cell with grain boundaries (d = 200 nm) 196

6-17. Voc of solar cells as a function of effective grain size 197

6-18. J_{SC} of solar cells as a function of effective grain size 197

6-19. Fill factor of solar cells as a function of effective grain size 198

6-20. Efficiency of solar cells as a function of effective grain size. 198

6-21. J_0 of solar cells as a function of effective grain size 199

6-22. J_0 of solar cells as a function of effective grain size in log scale. 200

6-23. Net carrier distribution along the depth of the cell without illumination 202

6-24. Net carrier distribution along the depth of the cell with illumination 202

6-25. Potential along the depth of the solar cells ($N_T = 10^{12}$ cm^{-2}, $d_{eff} = 300$ nm) 203

6-26. Potential along the depth of the solar cells ($N_T = 10^{12}$ cm^{-2}, $d_{eff} = 1200$ nm) 204

6-27 Potential variation for different trap density along the grain boundaries (d = 200 nm) 205

6-28. Schematic diagram of VGB and HGB solved in this study 206

6-29. The effect of GB orientation on V_{OC} 207

6-30. The effect of GB orientation on J_{SC}.....207
6-31. The effect of GB orientation on Fill Factor.....208
6-32. The effect of GB orientation on efficiency.....208
6-33. The effect of GB orientation on J_0.....209
6-34. The effect of the depletion region width on the GB orientation effect on V_{OC}.....212
6-35. The effect of the depletion region width on the GB orientation effect on J_{SC}.....213
6-36. The effect of the depletion region width on the GB orientation effect on F.F. 213
6-37. The effect of the depletion region width on the GB orientation effect on η 214
6-38. The effect of the depletion region width on the GB orientation effect on J_0.....214

Abstract of Dissertation Presented to the Graduate School
of the University of Florida in Partial Fulfillment of the
Requirements for the Degree of Doctor of Philosophy

MOLECULAR BEAM EPITAXIALLY GROWN COPPER INDIUM DISELENIDE AND COPPER GALIUM DISELENIDE FILMS

By

Seokhyun Yoon

May 2005

Chair: Timothy James Anderson
Major Department: Chemical Engineering

To eliminate the influence of grain boundaries, $CuInSe_2$ (CIS) and $CuGaSe_2$ (CGS) films were grown on (100) GaAs wafers. The effects of Cu to III metal ratio and dosing with Na on the growth mode and defect properties were studied at two growth temperatures. The impact of post-annealing in Se on the defect structure of CGS film was also studied. Two-dimensional simulations were used to better understand the role of grain boundary on cell performance.

For growth at 360 °C, the In-rich CIS films were polycrystalline, whereas the Cu-rich CIS films were epitaxial exhibiting a Stranski-Krastanov (S-K) growth mode. It is proposed that a Cu-Se secondary phase enhances the mobility of adatoms, allowing epitaxial growth to a critical thickness, at which point segregation at the nucleation sites became faster the rate of growth. Island structures, embedded in a matrix region, were oriented along the [01-1] directed edges with surface undulations apparent on the matrix surface with dominant {112} crystal planes.

At the higher growth temperature of 464 °C, the CIS films grew epitaxially without the need of a Cu-Se phase. Both CIS films grown at low and high temperatures were nearly relaxed. The segregation of epitaxial $Cu_{1.5}Se$ was also observed in the Cu-rich, Na-dosed CIS film, which is attributed to a surfactant effect of Na. At a growth temperature of 438 °C, CGS films showed a S-K growth mode and nearly pseudomorphic growth. Hemispherical islands with twins were observed in the Ga-rich CGS films and epitaxial $Cu_{1.5}Se$ phase were identified in the top region of the island structure. From the PL analysis of Cu-rich, Na-dosed CGS film after Se-annealing, a new defect level located 20 meV above the valence band edge was identified as Na_{Ga} acceptor state.

Two-dimensional simulation of the impact of grain boundaries on device performance showed that the short circuit current decreases sharply along with the other device parameters below a critical grain size due to the complete depletion. The increase of dark saturation current with decreasing grain size was predicted due to an increase in the recombination current.

CHAPTER 1
INTRODUCTION

1.1 Theoretical Background

1.1.1 History of Solar Cells

The conversion of sun light directly into electricity using the photovoltaic properties of suitable materials is the most elegant energy-conversion process developed by mankind. The driving force for the development of solar cell technology is the realization that the traditional fossil energy resources such as coal, oil, and gas are not only limited but they are also responsible for the unpredictable and possibly irresponsible climate changes through the emission of carbon dioxide.

Solar cells use the photovoltaic effect, which was discovered in 1839 by Becquerel, who studied the behavior of solids in electrolyte solutions. He observed that a small voltage and current were produced when he put metal plates in a suitable electrolyte and exposed it to sunlight. The first solid-state material that showed a significant light-dependent voltage between two contacts were Selenium and later cuprous oxide [Fri85, Sch28, Sch30, Smi73], which indicated that semiconductors would be the most promising class of materials for photovoltaic energy conversion. Technological development began with the development of a diffused silicon p-n junction, which was demonstrated at Bell Laboratories by Chapin *et al.* [Cha54]. It already had an efficiency of 6% that rapidly increased to 10%. Almost coincident with the beginning of silicon solar cell technology was the first development of cuprous sulfide/cadmium sulfide heterojunctions, which served as the origin for the subsequent intense research on thin film solar cell devices

[Ray54]. The first real impact of solar cells was only realized with the advent of space exploration. The demand for a reliable, long lasting power source was the major reason for the application of solar cells, and by 1958 the first silicon solar cells were used in spacecraft. Increased research effort resulted not only in further improvement of the efficiency of silicon solar cells and a considerably lower energy costs, but also in the development of new photovoltaic materials and devices.

Silicon is the most extensively studied semiconductor and was the first commercially used solar cell material. Even if Si solar cells have drawbacks such as long term stability and high cost for high efficiency cells, Si solar cell technology has benefited from the high standard of silicon technology developed for circuits and the availability of single crystal silicon with high quality. The best laboratory efficiency for single crystal silicon is now 24.5% [Gre99]. The cost problem for the monocrystalline silicon had led to the development of polycrystalline silicon solar cell and its record efficiency is reported as 14.2% by Neu *et al.* [Neu02].

Parallel with the development of solar cell technology based on crystalline silicon, other concepts were pursued to avoid the disadvantages of silicon. A wide variety of compound semiconductors, such as GaAs, CdTe, InP and CdS, have a band gap energy that is more suitable to the solar spectrum and therefore have the potential for higher efficiency. In fact, GaAs solar cells have demonstrated efficiencies of about 25% [Wei88]. Most of those semiconductors, however, cannot yet be produced inexpensively enough to be competitive. Most compound semiconductors are direct-bandgap materials with high absorption coefficients; therefore, thin films of only a few μm thicknesses are needed to absorb the light. This reduces manufacturing cost. Also in this case, the electron-hole

pairs generated by light absorption are close to the space charge region, where they can be swept by the built-in electric field and contribute to the current. Therefore, the loss of carriers due to recombination can be greatly reduced. A wide range of new semiconductor materials for bulk and thin film devices has been opened with the exploration of ternary and quaternary compounds. And, of those compounds, $Cu(In,Ga)Se_2$ compound is the most promising candidate as it has the highest absorption coefficient and good photovoltaic properties as a polycrystalline thin film.

1.1.2 Device Physics

A solar cell is a minority carrier device, which means that the device is working by the transport of minority carriers in the semiconductor. Figure 1-1 shows the structure and the band diagram of a p-n junction diode solar cell. As in Figure 1-1, when the p-type and n-type semiconductor layers are brought together, the Fermi level in each side should be equal at the equilibrium condition. In reaching equilibrium, there is a diffusion of electrons from the n-type to the p-type region and diffusion of holes in p-type region into the n-type side. The immobile charged donor and acceptor atoms left behind result in the formation of a depletion region or space charge region with an associated built-in potential. The width of the depletion region in each layer depends on the doping level of each layer.

At equilibrium, the driving force due to the carrier concentration gradient is just balanced by the electric field (constant electrochemical potential) to give no net current flow. Thus those minority carriers that are within a diffusion length (L_n or L_P) from the depletion region edge will be swept by the electric field across the depletion region to the side where they are majority carriers, and thus contribute to the current to the contact.

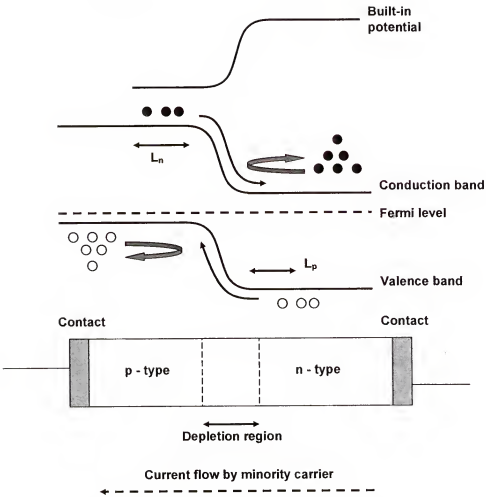

Figure 1-1. Transport of carriers in p-n junction solar cell; (●) electron, (○) hole

This is why solar cells are called minority carrier devices. Figure 1-2 shows a typical current vs. voltage (I-V) plot with and without illumination. When there is no light, electron-hole pairs are generated by thermal excitation. Under reverse bias (increased barrier potential), only minority carriers contribute to the current. This current, I_0, is called the dark saturation current and is usually very small and depends on the band gap energy, doping level, and diffusion length among other parameters. A high value of I_0 often is associated with a leakage pathway.

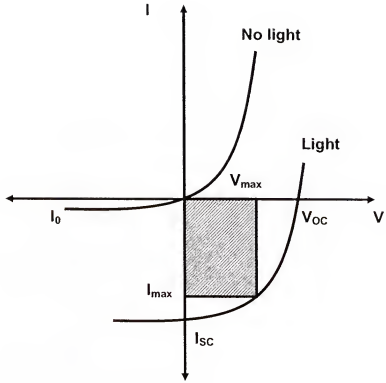

Figure 1-2. I-V curve with and without light

Upon applying forward bias, the barrier potential across the depletion region decreases. This reduction of barrier potential increases the number of electrons in the n-type region and holes in the p-type region that have sufficient energy to surmount the barrier and the amount increases in exponential manner. Therefore, the current-voltage characteristics can be represented by the following equations:

$$I = I_0(e^{qV_A/kT} - 1), \quad I_0 = qA(\frac{D_n n_i^2}{L_n N_A} + \frac{D_p n_i^2}{L_p N_D}), \quad or \quad J_0 = q(\frac{D_n n_i^2}{L_n N_A} + \frac{D_p n_i^2}{L_p N_D}), \quad (1\text{-}1)$$

where A is the area of the device, $D_{n,p}$ are the electron and hole diffusivities, n_i is the intrinsic carrier density, $L_{n,p}$ are the electron and hole diffusion lengths, $N_{A,D}$ are the doping levels of p-type and n-type regions, and J_0 is the dark saturation current density.

When there is illumination, minority carriers are generated at high rates by absorption and thus the reverse current is much larger. As the forward bias increases under illumination, the reverse current is cancelled by the forward current, which increases exponentially and the curve passes the point of no net current flow condition called the open circuit voltage, V_{OC}. In Figure 1-2, I_{SC} is the short circuit current as there is no load (V = 0) in this case. As one of the important device parameters in solar cells, the fill factor (F.F.) reflects the fraction of the power that can be produced by a solar cell given its I-V characteristic. As illustrated in Figure 1-2, the F.F. and efficiency are defined as follows:

$$F.F. = \frac{P_m}{I_{SC}V_{OC}} = \frac{I_m V_m}{I_{SC}V_{OC}}, \tag{1-2}$$

$$\eta = \frac{I_m V_m}{Photon\ \ Energy} \times 100(\%) = \frac{(F.F.)I_{SC}V_{OC}}{Photon\ \ Energy} \times 100(\%), \tag{1-3}$$

where I_m and V_m are the current and voltage that give the maximum power. Therefore, to obtain high efficiency, high values for F.F., V_{OC}, and I_{SC} are required.

The value of V_{OC} is strongly related to the electron affinity differences and the doping levels of the p-type and n-type layers. I_{SC} is determined by the transport process of minority carriers in each region as they attempt to reach the edge of the space charge region. Therefore, it is very important to find the right material for each type of semiconductor. It is important to have a high absorption coefficient to reduce the required thickness and the distance to the space charge region. Also, control of electronic point defects resulting from structural or compositional deviations from the ideal case is also very important, as these defects can affect the annihilation of minority carriers.

1.1.3 Photovoltaic Devices Based on $CuInSe_2$ and $CuGaSe_2$

A large number of ternary and quaternary semiconductors have been investigated for their potential as high performance, inexpensive solar cell absorber layers to serve as an alternative to single crystal or polycrystalline silicon. Several groups of ternary compounds with the composition of $A^{I}B^{III}X_2^{VI}$ have attracted attention because of their interesting optical, electrical, and structural properties [Gib80, Kur87]. These compounds offer a broad range of optical band gap energy and carrier mobility. The ternary compounds that have been most intensively investigated so far are the chalcopyrite compounds based on the transition elements A = Cu or Ag, B = Al, Ga, In and X = Se, S, Te. Historically, Cu-ternary compounds were the most attractive candidates because of the previous developments of a similar Cu_2S-CdS solar cell. Research on the Cu chalcopyrites has been focused on three compounds: $CuInS_2$, $CuInSe_2$ and $CuInTe_2$, of which $CuInSe_2$ has been considered the most promising semiconductor.

$CuInSe_2$ has many advantages as an absorber material including a high absorption coefficient (as high as 10^5 cm^{-1}), good stability, and a wide range of stoichiometry in the chalcopyrite structure. It is a direct band gap material with a band gap of 1.04 eV at room temperature. For CIS cells, a record efficiency of 14.5% was reported by Abushama *et al.* [Abu04] even with imperfect match of the band gap to solar spectrum.

Another ternary chalcopyrite compound, $CuGaSe_2$ (CGS), has been a promising material, especially as a top cell material in tandem cell devices. It is a direct band gap material with band gap energy of 1.72 eV and a high optical absorption coefficient ($\alpha \geq 3\times10^4$ cm^{-1}). Although it better matches the solar spectrum, the highest reported efficiency of a CGS cell is only 10.2% [Mar04]. The performance of thin-film $CuInSe_2$

based solar cells has been improved by the addition of Ga to form $Cu(In,Ga)Se_2$ absorber layers, which produced an efficiency as high as 19.5%[Sur05].

A decrease of cell efficiency, however, has been reported for CIGS cells when the addition of Ga exceeds 30%. The reason for this decrease is not fully understood, however, most of the decrease is attributed to lower values of Voc. One possible explanation is related to the band alignment between the absorber material and the buffer layer to present a barrier to carrier transport. Another possible explanation is related to the type inversion. Although a higher V_{OC} should be obtained due to the higher band gap by the addition of Ga to CIGS cells, the addition of Ga over 30% limits the CIGS absorber to only p-type conductivity. To obtain high efficiency cells, it is essential to have a very thin n-type layer near the surface region of the absorber layer. This n-type layer forms a buried junction in the absorber layer and greatly reduces the recombination at the electrical junction, which does not coincide with the metallurgical junction in this case. Therefore, excess Ga addition to CIGS absorber layer decreases the efficiency of cells.

1.1.4 Thermochemistry and Structural Properties of CIS or CGS Materials

The thermochemistry of the Cu-In-Se ternary system has been intensively studied; however, significant inconsistencies still remain. Figure 1-3 is a T-x section of the Cu_2Se-In_2Se_3 pseudobinary phase diagram assessed by Chang and coworkers [Cha96a]. There have been several efforts to find pathways with mild processing conditions (e.g., low growth temperature, low vapor pressure) to obtain CIS materials by examining the phase diagram (e.g., rapid thermal processing (RTP) to avoid formation of undesired phases, the three-stage process developed by the National Renewable Energy Laboratory (NREL) [Kar93, Ker02]).

Rapid thermal processing is a method to synthesize α-CIS from precursor films by rapidly increasing the temperature of precursor structure (e.g., the bilayers, /CuSe/InSe/ or /InSe/CuSe/). The NREL 3-stage process begins with deposition of (In,Ga)+Se, followed by a Cu+Se deposition step, and then finishes with a (In,Ga)+Se deposition step. Both processes are developed to exploit the existence of a Cu-Se eutectic liquid phase at a low temperature (~524 °C), although the presence of the liquid phase has not been verified. The liquid phase should enhance the mobility of atoms on the growth surface and increase the grain size during growth.

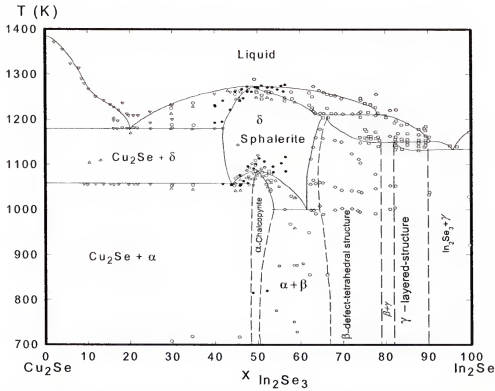

Figure 1-3. Assessed phase diagram along the Cu_2Se-In_2Se_3 pseudobinary section of the Cu-In-Se system [Cha96a]

The phase diagram of the Cu-Ga-Se ternary system is not as well characterized and more controversial than that of Cu-In-Se system. The earliest phase equilibrium study was restricted to the pseudobinary Cu_2Se-Ga_2Se_3 section of the phase diagram and suggested the existence of one high-temperature disordered phase and 4 room temperature stable phases [Jit98, Pal67]. These studies were summarized and the pseudobinary phase diagram was shown in M. Ider's work [Ide03] as shown in Figure 1-4.

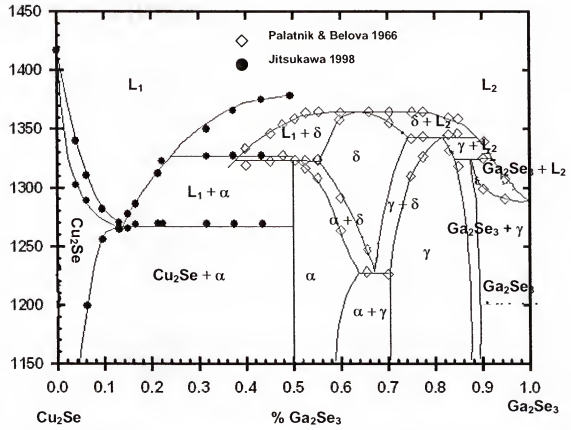

Figure 1-4. Assessed phase diagram along the Cu_2Se-Ga_2Se_3 pseudobinary section of the Cu-Ga-Se system [Ide03]

Two of the high temperature phases were solid solutions of the terminal binary compounds, one was a β-phase and the last was the δ-phase with a Gallium-rich

composition and layered structure. The study found that the stoichiometric compound $CuGaSe_2$ has a chalcopyrite (α) structure. For CIS, the homogeneous range of the chalcopyrite phase extends significantly to Cu-rich composition and the range extends to In-rich composition at high temperature. For CGS, however, this range extends to Ga-rich composition as in Figure 1-4. This range of stoichiometry gives rise to a complex defect chemistry, which is discussed in section 1.1.5. The next section reviews the structural information for the important absorber layer phases. The discussion begins with most studied and relevant phase - α-CIS.

1.1.4.1 Chalcopyrite or α-CIS

The crystal structure of chalcopyrite CIS has been determined by several researchers. It is a member of the $A^{I}B^{III}C^{VI}$ family of chalcopyrite structures with the space group I-42d. The conventional unit cell of the chalcopyrite structure shown in Figure 1-5 is equivalent to two zinc blende unit cells with sides of length a stacked in the c-direction. This structure has Cu atoms at the 4a sites with (0 0 0) position, In atoms at the 4b sites with (0 0 1/2) position, and Se atoms at the 8d sites with (x 1/4 1/8) position [Spi74]. Each anion and cation has a tetrahedral bonding and each Se anion is coordinated by two Cu and two In cations, while each cation (Cu or In) is coordinated by four Se anions as in Figure 1-5. The Se anion is located at an equilibrium position closer to one pair of cations. Therefore, the bond lengths between anion and the two different cations are not equal, $R_{AC} \neq R_{BC}$, and this bond length alternation makes the lattice constants of the chalcopyrite structure anisotropic. The nearest bond lengths for chalcopyrite CIS can be represented from the structural parameters as

$$R_{AC} = [x^2 + (1+\eta^2)/16]^{1/2} a \qquad (1\text{-}3)$$

$$R_{BC} = [(x - 1/2)^2 + (1 + \eta^2)/16]^{1/2} a, \qquad (1\text{-}4)$$

where x is the anion displacement (no displacement for x = 1/4), and the ratio, $\eta = c/2a$, is the tetragonal distortion (no tetragonal distortion when $\eta = 1$).

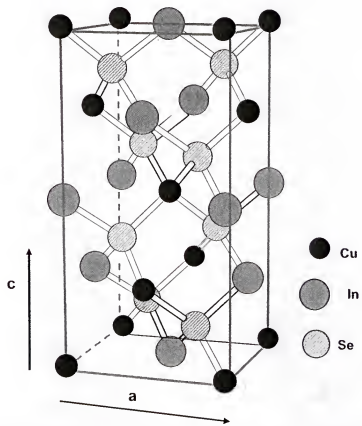

Figure 1-5. Conventional unit cell of $CuInSe_2$ with chalcopyrite structure

The lattice constants of CIS have been measured by several investigators and the early results by Spiess *et al.* [Spi74] are in good agreement with the most recent bond length measurement by EXAFS [Cha03]. The values are a = 5.784 Å, c = 11.616 Å, x = 0.224, $d_{Cu\text{-}Se}$ = 2.424 Å, and $d_{In\text{-}Se}$ = 2.598 Å.

1.1.4.2 Sphalerite or δ-CIS

δ-CIS is unstable at room temperature. From the pseudobinary phase diagram shown in Figure 1-3, it is widely agreed that it can be formed from the solidification of ternary liquid mixture or from the first order solid phase transition from α-CIS or β-CIS or a mixture of them. δ-CIS shows a congruent melting composition with 52.5 mole % In_2Se_3 at 1005 ^oC [Hor96]. The first-order α to δ solid phase transition at 50.8 mole % In_2Se_3 and 809 ^oC corresponds to the crystallographic order-disorder transition. The sphalerite structure is based on the zincblende unit cell and does not show tetragonal distortion. Additionally, there is no long-range ordering of Cu and In atoms on the cation sublattice as illustrated in Figure 1-6a.

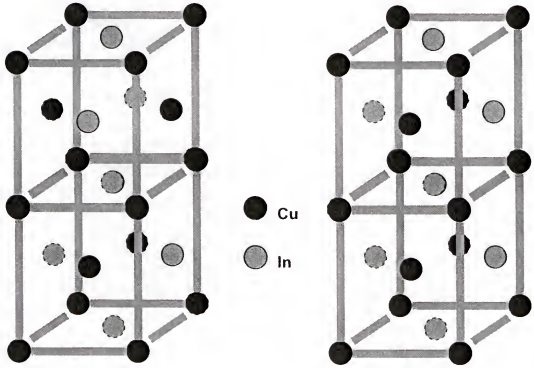

Figure 1-6. Sphalerite and Cu-Au like structures of $CuInSe_2$: (a) Sphalerite structure, (b) Cu-Au like structure. Note the Se atoms are not shown in these schematics.

1.1.4.3 β-CIS ($Cu_2In_4Se_7$ and $CuIn_3Se_5$)

The existence of the peritectoid decomposition reaction of δ-CIS to α-CIS and another In_2Se_3 rich compound (see phase diagram) requires that at least one phase lies on the tie-lie between $CuInSe_2$ and In_2Se_3 composition to satisfy the Gibbs phase rule. At least eight different compounds ($Cu_2In_4Se_7$, $CuIn_3Se_5$, $CuIn_5Se_8$, $Cu_8In_{18}Se_{32}$, $Cu_7In_9Se_{32}$, $Cu_{14}In_{16.7}Se_{32}$, $Cu_2In_3Se_5$, $Cu_3In_5Se_9$) and structures based on eight different space symmetry groups (I-4,I-42m, P23, Pm3, P432, P-43m, Pm3m, P-42c) have been proposed for β-CIS from the review by Chang [Cha99]. β–CIS compounds are sometimes called P-chalcopyrite. This designation is based on the work by Hönle *et al.* [Hön88] as they concluded that the structure possesses P-42c symmetry. These compounds are also called ordered defect compounds (ODCs). The ordering refers to the arrangement of crystallographic sites where defects are formed. Chang and coworkers [Cha03] extensively studied the local structure of $CuIn_3Se_5$ by extended X-ray absorption fine structure (EXAFS). From the least square fit of the Se K-edge EXAFS spectra, he showed that for $CuIn_3Se_5$, the Se first nearest neighbor local structure is composed of 0.8 Cu and 2.4 In atoms, while Se in $CuInSe_2$ has 2 Cu and 2 In atoms as the first nearest neighbor atoms. He also showed that the In and Cu first nearest neighbor distance in $CuIn_3Se_5$ is almost the same as that in $CuInSe_2$.

1.1.4.4 CuAu-like CIS

It had been accepted that only two equilibrium crystallographic structures exist for $CuInSe_2$, the chalcopyrite structure (α-CIS) at low temperature, and the disordered sphalerite structure (δ-CIS) at higher temperature [Cha96b]. From theoretical quantum-mechanical calculations of the α–CIS to δ–CIS order-disorder transition by Wei *et al.*

[Wei92], it was shown that the formation energy of CuAu-like (CA) CIS (Figure 1-5b) is only 0.2 meV/atom higher than that of the chalcopyrite CIS at T=0. As shown in Figure 1-6a, the equilibrium α-CIS structure consists of alternating (201) planes of Cu and In atoms on the cation sublattice, while the CA-CIS structure consists of alternating (200) planes. Both calculations and experiments have shown the red shift of the band gap energy when the material transforms from the α−CIS structure to the CuAu structure.

Experimentally, CA ordering of the Cu-III-VI_2 compounds was first reported [Su98] for $CuInS_2$ grown at low temperature. Recently, CA-ordering has been shown in $CuInSe_2$ both for Cu-rich and In-rich CIS grown on vicinal (001) GaAs substrates by migration enhanced epitaxy (MEE) [Sta02]. They analyzed CIS epilayers by both XRD and TEM to show that CIS epilayers contained CA-ordered domains. XRD spectra showed reflectance from (00n) planes with odd values of n, which can not be generated by either the sphalerite or chalcopyrite structures. Also, TEM diffraction patterns showed extra spots for the (001) plane of CA-CIS. The (001) diffraction spot, however, can be generated from double diffraction of α-CIS. Raman scattering of the vibrational mode at 185 cm^{-1} was used to probe for the existence of domains with the CA structure [Sta02].

1.1.5 Defects in Chalcopyrite CIS or CGS

When there is a deviation of the composition from their ideal stoichiometric values for CIS or CGS compounds, it can be represented by two parameters, molecularity deviation, Δm, and valence stoichiometry deviation, Δs.

$$\Delta m = \frac{[I]}{[III]} - 1 \quad , \quad \Delta s = \frac{2 \times [VI]}{[I] + 3 \times [III]} - 1 \tag{1-5}$$

In these equations, [I] and [III] represents the atomic fraction of each metal and since [I]+[III]+[VI] = 1, these two variables uniquely determine the composition of the compounds.

The usefulness of molecularity and valency deviations has been experimentally demonstrated by the conductivity studies of single crystal $CuInSe_2$ [Neu90]. Neumann and Tomlinson showed that within the range of $|\Delta m| < 0.08$ and $|\Delta s| < 0.06$, the compound shows p-type conductivity whenever $\Delta s > 0$, while it is n-type when $\Delta s < 0$.

When there is a deviation of composition, intrinsic defects are introduced into CIS or CGS to maintain the crystal structure for non-stoichiometric composition. Some of the intrinsic defects are shallow-level defects, which can be used to dope the crystal without any extrinsic doping, while others can act as traps for carriers. The set of intrinsic point defects possible in $CuInSe_2$ or $CuGaSe_2$ with the combination of substitutional atoms, vacancies, and interstitials are V_{Cu}, V_{III}, V_{Se}, Cu_{III}, Cu_{Se}, III_{Cu}, III_{Se}, Se_{Cu}, Se_{III}, Cu_i, III_i, and Se_i (III = In or Ga). Some of the defects, however, have minimal concentrations because of their high formation energy.

The point defects determine the conductivity type and the carrier density of the compound. Past work on single crystals and thin films showed that CIS can be made p-type or n-type depending on the growth or annealing conditions, which change the defect structure in the films [Iso80, Sha85]. It was also reported that it is difficult to prepare CGS with n-type conductivity, whereas CIS can easily be converted from p-type to n-type and reversed by annealing [Tel72]. Therefore, it is important to study the point defect structure of CIS and CGS since the point defects connect device processing conditions to the properties important in device performance.

The following section reviews the literatures on the point defects in CIS and CGS. The purpose is to identify each acceptor and donor sate and its corresponding energy level.

1.1.5.1 Defects in CIS

Rincón *et al.* [Rin83] studied the impurity states of as-grown n-type melt-grown CIS single crystals by PL at 7 K and determined the energy gap and the donor and acceptor levels in CIS, which were proposed as (1.023±0.03) eV, (10±2) meV below the conduction band (CB) edge, and (33±2) meV above the valence band (VB) edge, respectively. They were, however, not assigned to the specific defect states. The optical characterization of CIS films grown by molecular beam epitaxy was first reported by Niki *et al.* [Nik94, Nik95]. They reported PL peaks at E_1(1.0318), E_2(0.9689), E_3(0.9407), E_4(0.9126), E_5(0.8846), E_6(0.8567), E_7(0.8280) and attributed them to exciton-related, acceptor-to-CB transition (A-CB), longitudinal optical phonon (LO) replica of E_2, donor-to-acceptor (D-A) transition, and the 1LO, 2LO, 3LO of E_4, respectively. They assigned E_3 and E_5, E_6, E_7 to LO of E_2 and E_4, respectively because the energy differences were 27.9 meV (226 cm^{-1}) ~ 28.7 meV (232 cm^{-1}), which were similar to the reported LO phonon energy of 233 cm^{-1} [Tan92]. These phonon replicas were first reported by this group. Specific defect states, however, were not assigned to each transition peak in their study. They also investigated the PL peaks near the band edge and identified the peaks for the transition by the ground state free exciton and exciton bound to acceptor state and suggested 76 meV for the acceptor state using Hayne's rule. However, the acceptor state with an energy level of 71 ~ 76 meV observed here was not assigned and different from that observed in Rincón *et al.*'s study [Rin83], and the donor level involved in the peak at 0.9126 eV was not investigated.

Schön *et al.* [Sch97a] observed two PL peaks for p-type CIS grown by zone melting and assigned them to the D-A transition from their peak shift to higher energy with increasing excitation power. From thermal quenching of two PL peaks, an acceptor state at 40 meV from VB and a donor state at 80 meV from CB were suggested and assigned to V_{Cu} and V_{Se} in their study. PL peaks related to excitonic emission in CIS films grown by chemical vapor transport (CVT) and zone melting were also investigated by the same group [Sch98]. They calculated the binding energy of the free exciton from the PL peak energies for the ground state and the first excited state of the free exciton. They also observed bound exciton emission peaks at 1.0383, 1.0347, 1.0343, 1.0339, 1.0321, and 1.0244 eV and calculated the related defect level, E_i using, $E_{FX} = E_g - E_{FX} - cE_i$ [Hay60], where E_g, E_{FX} and E_{EX} are known. Considering the stoichiometry and conduction type of each film and the formation energy of each defect, they assigned each defect level E_i to V_{In} (24 meV), Cu_{In} (55 meV), Cu_i (80 meV), In_{Cu} (46 meV), In_i (132 meV) and V_{Cu} (41 meV). In their study of the excitonic transition, V_{Cu} defect state was observed to have a similar energy level (41 meV) with that of V_{Cu} (40 meV) in their previous study.

In summary, the major point defects in CIS are the donors V_{Se} and In_{Cu}, acceptors V_{Cu}, Cu_{In} and V_{In}. The activation energies for the defects are well established for V_{Cu} and V_{Se} but disagreement exists in the energy levels for In_{Cu}, and there are very few experimental results for Cu_{In}, In_i, Cu_i, and V_{In}.

1.1.5.2 Defects in CGS

There have also been a few PL studies on the defect structure of epitaxial or single crystal CGS films. Chichibu *et al.* [Chi94] characterized epitaxial CGS films grown by MOCVD using PL along with photoreflectance. They observed an intense peak at 1.71

eV at 77 K and a weak peak at 1.66 eV. They assigned the peak at 1.71 eV to an exciton related transition from the peak energy dependence on temperature and from the result that the full width half maximum (FWHM) varies as 1.8kT. They also assigned the peak at 1.66 eV to free-to-acceptor transition from the results of their previous study [Shi93], which were assigned to the exciton related PL and to the free-to-acceptor transition, respectively. Considering the band gap energy of 1.71 ~ 1.72 eV in this case, the energy level involved in the free-to-acceptor transition at 1.66 eV can be estimated as 50 ~ 60 meV, which can be assigned to V_{Cu} as in the case of CIS film.

Sn-doped CGS films grown by CVT were studied by PL and a V_{Cu} acceptor level with the activation energy of 53 meV was suggested from the location of the band-to-acceptor transition peak at 1.672 eV and the band-to-band peak at 1.725 eV [Sch96]. A V_{Se} donor level with 80 meV activation energy was also suggested from the peak at 1.60 eV that was assigned to the donor-acceptor transition.

The PL peak near band edge (1.713 eV) for MBE grown CGS films was studied [Yam96] and from the superlinear dependence of emission intensity on the excitation power, it was assigned to excitonic emission. From temperature dependent PL measurements and subsequent parameter fitting of the data using equation (1-6) below, they validated their assumption that the peak represents the convolution of the free exciton and bound exciton peaks and their activation energies were suggested as 16.2 and 3.3 meV, respectively.

$$I(T) = C_0 \frac{1 + rC_1 e^{-E_{a1}/kT}}{1 + C_1 e^{-E_{a1}/kT} + C_2 e^{-(E_{a1}+E_{a2})/kT}} \qquad (1\text{-}6)$$

They also suggested phonon energy of 26 meV by fitting the temperature variation of E_g to the Manoogian-Leclerc equation [Man79]:

$$E_g(T) = E_0(0) + UT^x + V/(e^{\hbar\omega/kT} - 1) \quad (1\text{-}7)$$

PL peaks at 1.714, 1.62, and 1.587 eV were also observed in their study [Yam97] and the peak at 1.714 eV was assigned to exciton recombination and that at 1.587 eV to the LO replica of the peak at 1.62 eV. They extensively investigated the peak at 1.62 eV by excitation power dependent PL and temperature dependent PL, and suggested the peak is related to the donor related transitions such as donor-VB and donor-acceptor with very shallow acceptor state. The donor level at 108 meV and acceptor level at 3.4 meV were estimated from parameter fitting of the excitation intensity using Equation (1-8).

$$I = \frac{C_1}{1 + C_2 \exp(-E_D/kT)} + \frac{C_3}{[1 + C_4 \exp(-E_D/kT)][1 + C_5 \exp(-E_A/kT)]} \quad (1\text{-}8)$$

Also, the peak at 1.71 eV was assigned to the transition of an exciton bound to this donor state from the fact that the difference from the band gap (E_g=1.73 eV at 2K), 19.5 meV, was estimated to be very close to the suggested fraction of donor states (0.18 of 108 meV). The V_{Se} defect was suggested as a donor at 108 meV and Cu_{Ga} as an acceptor state at 3.4 meV in their study. The energy level of V_{Se} defect state was different from the previous study (80 meV in Schön *et al.*'s study [Sch96]) and V_{Cu} defect state was not observed in this study, which may be attributed to the Cu-rich composition of their film that led to the formation of Cu_{Ga} defects.

Cu-rich CGS films grown by MOCVD were studied by Bauknecht *et al.* [Bau00]. From the PL spectrum, they suggested the donor level assigned to V_{Se} at 80 meV and two acceptor levels at 10 and 50 meV, which are assigned to Cu_{Ga} and V_{Cu}, respectively.

In summary, the major point defects in CGS film are the donors V_{Se}, Ga_{Cu}, and acceptors V_{Cu}, V_{Ga}, and Cu_{Ga}. The activation energies for the defects are well established

for V_{Cu} and V_{Se} but disagreement exists in the energy levels for Cu_{Ga}, and there are very few experimental data for the defects, Ga_{Cu} and V_{Ga}.

1.1.5.3 Comparison of Defects in CIS and CGS

There have been several researchers who studied the differences in the defect structures of CIS and CGS films. In particular, it is known that CGS is more difficult to make n-type. Schön *et al.* [Sch99] proposed that this difference is due to the different defect chemistry, especially the higher formation energy of Ga_{Cu} donor defect in CGS as compared to In_{Cu} in CIS. This was supported by PL measurements on CIS and CGS single crystals grown by CVT in their study. PL measurements showed that the III_{Cu} donor defect, Ga_{Cu} has a much higher activation energy of 130 meV compared to 25 meV for In_{Cu}, while the values of the activation energy for the V_{Cu} acceptor state are similar (CIS (45 meV) and CGS (60 meV)). They suggested that there are two reasons why it is difficult to make CGS n-type:(1) The lattice compression produced by the smaller Ga atom results in the movement of the conduction band upward and thus a deeper Ga_{Cu} level, and (2) the 4s energy level of Ga atom is lower than In 5s energy level further depressing the Ga_{Cu} level.

In further work [Sch00c], CIS and CGS films grown by CVT were studied by PL and the difference of the donor level activation energy was studied before and after annealing in In or Ga ambient. For CIS, they reported PL peaks at 1.04, 0.957, and 0.93 eV for as grown samples. From excitation-dependent PL for the peak at 0.957 eV and comparison of the difference (27 meV) between the peaks at 0.957 and 0.93 eV to the values reported in the literature [Tan92], they assigned them to free-exciton, donor-acceptor pair transition, and the LO phonon replica of donor-acceptor transition, respectively. For CGS, they observed peaks at 1.725, 1.678, and 1.642 eV and assigned

them to free exciton, donor-acceptor, and LO phonon replica of donor-acceptor transition by the same method used for CIS with LO phonon energy of 36 meV. From temperature quenching of donor-acceptor transition peaks, they extracted the acceptor level activation energy of 45 meV for CIS and 55 meV for CGS, and attributed them to V_{Cu} for both films, which shows good agreement with the previous studies [Chi94, Bau00, Sch97a, Sch98, Sch99]. The activation energy of the donor level in each film involved in the donor-acceptor transition was calculated from excitation-dependent PL by using Equation (1-9) and estimated to be 60 and 80 meV in CIS and CGS, respectively. Both donors were assigned to a V_{Se} defect.

$$E = E_g - (E_a + E_d) + \frac{e^2}{4\pi\varepsilon_r\varepsilon_0 r} + f(r) \tag{1-9}$$

New PL peaks at 0.985 and 1.541 eV for CIS and CGS were observed in their study after annealing in a group III element environment. For these PL peaks, the related acceptor level was found to be the same, V_{Cu}, for both materials, while the lowest defect level involved was 25 meV for CIS. This lower defect level for CIS was assigned to In_{Cu} donor level because the film showed n-type conductivity. From the peak location in CGS film, they also calculated the activation energy of Ga_{Cu} donor level as 130 meV. This value matches the activation energy suggested by Schön *et al.* [Sch99] from their PL measurements on CVT grown samples. They also attributed p-type only conductivity for CGS to the larger activation energy of Ga_{Cu} donor level along with its large formation energy.

Annealing the as-grown CIS and CGS films in an oxygen environment was reported to change the defect structure of the films [Nik01, Nik02,]. PL study of Cu-rich and In-rich CIS films before and after annealing in oxygen and in Ar environment was

performed in their study. They observed that the PL spectrum of Cu-rich CIS film was dominated by a conduction band to V_{Cu} emission. From the fact that In-rich CIS showed a similar PL spectrum to that of Cu-rich CIS only after annealing in oxygen environment, they showed that the acceptor type defect, which is assigned to V_{Cu}, is common to both Cu-rich and In-rich CIS. They also suggested that oxygen is responsible for the removal of the anion vacancy, V_{Se}, by transforming the divacancy, V_{Cu}-V_{Se}, to V_{Cu}-O_{Se} from the significant increase in oxygen concentration and the change of PL spectrum of In-rich CIS to the same pattern as Cu-rich CIS after air-annealing. For Ga-rich CGS film, PL measurements revealed the same change after oxygen annealing and it was similarly attributed to the removal of V_{Se} by oxygen incorporation.

In summary, the differences between CIS and CGS point defects are, for major acceptor type defect, V_{Cu} in CGS has a slightly deeper energy level of 50 ~ 60 meV compared to the energy level of 40 ~ 50 meV in the case of CIS. For major donor type defects, however, V_{Se} in CGS has a deeper level of 80 meV than that of CIS with 60 meV energy level. Another major donor type defect, Ga_{Cu} in CGS has much deeper energy level of 130 meV compared to an energy level of 25 meV ~ 45 meV for In_{Cu} in CIS, which makes CGS only n-type.

1.1.5.4 Na and CIGS

It has been noted that CIGS solar cells with high efficiencies are produced when grown on soda-lime glass substrate [Sto93]. This has led to the hypothesis that Na released from the glass substrate plays an important role. The mechanism behind the improvement of the device by Na incorporation, however, has been widely debated with both electrical and structural roles suggested.

There have been several studies about the effect of sodium on the electrical properties of CIGS films. Holz *et al.* [Hol94] investigated the influence of Na on the electrical conductivity of polycrystalline CIS and CIGS thin films. They observed lower values of conductivity activation energy (~ 45 meV) for CIS on soda-lime glass as compared to the value when a Na barrier was placed on the substrate (~ 75 meV). They also simulated the effect of Na diffusion from the substrate by Na implantation and observed that the conductivity activation energy of CIGS films with Na implantation is lower (~ 41 meV) than that of CIGS films on a Na-free substrate (~347 meV), but similar to that of CIGS on soda-lime glass (~38 meV). They also compared the activation energy of polycrystalline CIS with Na implantation (30 ~ 50 meV) with that of CIGS on Na-free substrates (~347 meV) and that of CIS single crystal without Na (~40 meV). From those observations, they proposed that Na implantation changes the mechanism of carrier transport from a grain boundary process to a bulk process, for example as in single crystals, by affecting the grain boundaries.

Ruckh *et al.* [Ruc94] studied the effect of substrate with and without sodium on the electrical properties of polycrystalline CIGS thin films by XRD, XPS and EDS. They observed increased electrical conductivity, reduced space charge region width and higher V_{OC} for CIGS thin films prepared on soda-lime glass as compared to those prepared on alkali-free substrates. They also observed an increase in oxygen concentration along with sodium concentration in CIGS films. They did not observe, however, an influence of sodium on the morphology of the films. They attributed the increase of V_{OC} to an increased acceptor concentration in CIGS thin films and explained it as a consequence of neutralization of donor-like Se vacancies through a promoted chemisorption of oxygen in

the presence of sodium. They also observed a similar effect when they added sodium in the form of Na_XO precursor.

There have also been studies that suggest the introduction of new defects by the incorporation of sodium in the polycrystalline CIGS thin films and their effect on the electrical properties. Rau *et al.* [Rau96] found that the incorporation of sodium led to a shallow acceptor state at about 75 meV above the valence band and an increase in the free carrier concentration in polycrystalline CIGS films, however, the defect state was not assigned. Keyes *et al.* [Key97] measured the electrical properties and PL spectra of polycrystalline CIGS thin film devices with sodium incorporation from soda-lime glass substrate and by the intentional incorporation of sodium in the form of NaF. They observed an increase in device efficiency and carrier concentration and attributed this to the removal of the shallow subgap states acting as a minority carrier trap by sodium incorporation. Niles *et al.* [Nil97] suggested that the increase of acceptor concentration by Na incorporation is due to the direct creation of acceptors such as antisite defect Na_{In}. Contreras *et al.* [Con97] explained the increase of the effective acceptor concentration by replacing the In atom of In_{Cu} defect with Na and forming inactive Na_{Cu} defect.

There have been other studies about the location of sodium in polycrystalline CIGS films and its effect on the growth or morphology of the films. Niles *et al.* [Nil99] proposed that sodium is mainly located at the grain boundaries of CIS films. This is based on the results using field emission Auger electron spectroscopy (FE-AES), which allows measurements with high spatial resolution. Braunger *et al.* [Bra00] observed that sodium influenced the growth of polycrystalline CIGS by interacting with Se. They suggested that sodium is mainly localized at the grain boundaries in the form of Na_2Se_X and serves

as a Se reservoir during oxidation of the metals in the film formation process. Granath *et al.* [Gra00] proposed that NaF should be a suitable precursor for sodium incorporation in the polycrystalline CIGS thin film solar cells and should give device performance similar to that with sodium derived from the soda-lime glass substrate. They also observed the presence of (112) surface texture, large grain size, and better efficiency for CIGS cells with NaF or soda-lime glass as a sodium source. In other study [Sch04], it was proposed that net doping of the CIGS films was observed to increase without the decrease of the compensating donors by Hall measurement though the energy levels found were not assigned to the specific defect state. In the recent review paper, A. Rockett [Roc04] proposed that Na mainly acts as a surfactant at the surface of the film during the growth and improves the bulk crystal quality without entering the bulk of the material.

Each of the studies discussed above have suggested positive effects on polycrystalline CIGS device performance when Na is incorporated. The studies, however, were complicated by the presence of grain boundaries. It has been suggested that Na resides mainly at the grain boundaries where it can influence the density of trap states in the polycrystalline CIGS films.

There have been very few studies, however, on the effect of sodium on CIGS single crystals. The effects of sodium on the electrical properties of epitaxial CIGS thin films grown by MBE were studied by Schroder *et al.* [Sch97b]. They incorporated Na in the film by either dipping as-grown film in NaOH solution or evaporating Na_2Se onto the sample surface. They found an increased Na concentration in the films after NaOH or Na_2Se treatment but no significant change in the O concentration. Two acceptor levels were identified by Hall measurement at 110 ~ 170 meV, and 34 ~ 40 meV, respectively,

above the valence band edge, but not assigned to any specific defect state. They observed an increase in the net carrier concentration at low temperature in films treated with Na and found a decrease in the concentration of compensating donors. They explained this decrease of compensation as an increase in the mobility of point defects when Na is incorporated, which enhances the clustering of oppositely charged defects instead of passivating donors directly. They also proposed that the observed compensation is not connected with the presence of oxygen. Lyahovitskaya *et al.* [Lya02] studied the Na effect in single crystal CIS film and from the annealing of the single crystal CIS in Na and Se ambient, they observed the formation of Na_2Se compound as well as the formation of Cu on the surface. They also observed the change of the conductivity type from n to p-type by annealing and attributed it to the Cu out-diffusion from the film leaving Cu vacancy instead of Se diffusion into the film by SIMS analysis. From SIMS analysis, they proposed that there is no evidence of Na presence in the bulk of the sample except for the films with many GBs or low crystal quality.

In summary, it is clear the Na reduces the effect of the grain boundaries in CIGS films either by removing the trap states at grain boundaries or by improving the crystal quality that leads to the film with less grain boundary. However, it is not as clear with respect to the effect of Na whether it introduces a new acceptor level in the films or compensates the existing compensating donor states such as In_{Cu} or Ga_{Cu} states in CIGS films.

1.1.5.5 First Principles Calculation of Defect Energies

First principles calculations have been used to study the defect physics of CIS films by several researchers. Zhang *et al.* [Zha98] first calculated defect formation energies with the conclusion that they vary considerably with Fermi energy as well as chemical

potential of the species. They also showed that defect complexes such as ($2V_{Cu}^{-} + In_{Cu}^{2+}$) and ($2Cu_{In}^{-} + In_{Cu}^{2+}$) have low formation energies and should be stable. They interpreted the formation of the ordered vacancy compounds such as $CuIn_5Se_8$, $CuIn_3Se_5$, $Cu_2In_4Se_7$ and $Cu_3In_5Se_9$ as a repeat of a single unit of ($2V_{Cu}^{-} + In_{Cu}^{2+}$) for each 4, 5, 7 and 9 units of CIS, respectively. They also attributed the very efficient p-type self-doping ability of CIS to the exceptionally low formation energy of the shallow defect, V_{Cu}. In addition the tolerance of CIS to compositional changes and different routes to synthesis and thus the large population of defects were attributed to electronic passivation of In_{Cu}^{+} defect by the $2V_{Cu}^{-}$ defect upon forming the complex.

Wei *et al.* [Wei98] also theoretically studied the effect of Ga addition to CIS film on its electronic and the structural properties. They found that the formation energies of the acceptors are similar in both CIS and CGS, however, the donor formation energy is larger in CGS than in CIS. They also found that the activation energies of acceptors are similar in CIS and CGS, but the Ga_{Cu} donor level in CGS is much deeper than the In_{Cu} donor level in CIS. The stability domain of the chalcopyrite phase was predicted to increase with Ga addition compared to the ordered defect compounds.

The effect of Na addition to CIS films was also studied by Wei *et al.* [Wei99]. Their calculation results suggest several Na effects. First, they predicted that if Na is present in relatively large excess, Na replaces Cu and forms stable $NaInSe_2$, which has a larger band gap. They proposed, however, that $NaInSe_2$ might precipitate at the grain boundaries as $Na_XCu_{1-X}InSe_2$ has a positive mixing enthalpy. They also proposed that if Na is present in a small amount, Na will form substitutional defect states on the Cu and In sites and the major effect of Na is to eliminate the In_{Cu} defect and the resulting increase

of the net hole density as the formation energy of Na_{Cu} is very exothermic. The calculations suggested the Na_{In} acceptor energy level (200 meV) is shallower than that of Cu_{In} (290 meV) calculated by Zhang *et al.* [Zha98]. They also proposed that displacing In_{Cu} as well as V_{Cu} by Na incorporation reduces the stability of ($2V_{Cu}^{-} + In_{Cu}^{2+}$) defect complex, which results in the suppression of the formation of the ordered defect compound.

1.1.5.6 Summary of Defect States and Energy Levels in CIS and CGS.

The defect levels in CIS and CGS films calculated by the first principles calculation and obtained by PL measurement are summarized as in Tables 1-1 through 1-4. In Tables 1-1 through 1-4, only the defect levels with single ionization state are displayed though there are calculated values for the defect levels with more than one ionization state.

Table 1-1. Energy levels above valence band edge and the formation energy for acceptors in CIS

Acceptor state	Theory	Experiment
Cu_{Se}		
Cu_{In}	290 meV [Zha98]/ ΔH_f=1.54 eV	55 meV[Sch98]
V_{In}	170 meV [Zha98]/ ΔH_f= 3.04eV	24 meV[Sch98]
V_{Cu}	30 meV [Zha98]/ ΔH_f = 0.60 eV	33 meV[Rin83], 40 meV[Sch97a], 41 meV[Sch98], 45 meV[Sch99, Sch00c]
Na_{In}	200 meV [Wei99]/ ΔH_f = 2.5 eV	

As reviewed in this section, there have been several studies on defects in CIS and CGS by both experimental methods and theoretical calculations. The assignments of the type and the energy level to each defect state, however, are still controversial for some of the defect states. In the Tables, it is shown that there are no values for the energy levels of the Se-related defect states (V_{Se}, Cu_{Se}) both in CIS and CGS by the theoretical calculation

though V_{Se} defect state was observed in CIS and CGS experimentally. The energy level of Na_{In} defect state was calculated as 200 meV by theoretical calculation, but there has been no experimental value reported for the energy level of that defect state. In particular, there is not much information on electrically active point defects in CGS. As summarized in Tables 1-3 and 4, the formation and ionization energies of Na_{Ga}, Cu_i, Ga_i, Cu_{Se} are not known either experimentally or theoretically but expected to be present in the material and there is only theoretical value of the energy level reported for Cu_i in CGS. Furthermore, the agreement between the experimental and predicted activation energies for donors (In_{Cu}, Cu_i, Ga_{Cu}) and acceptors (Cu_{In}, V_{In}, Cu_{Ga}, V_{Ga}, and V_{Cu} in CGS) is poor except V_{Cu} in CIS. Thus there is a need to better understand the point defects in CGS. This issue is particularly important since the difficulty of type inversion and band alignment between the buffer layer and the CGS absorber layer appears to be linked to the poor CGS cell performance. As for the Na effect on the defect chemistry of CGS film, Na_{Ga} can be proposed as the possible defect state related to Na in CGS. The defect states such as V_{Ga}, V_{Cu}, and Cu_{Ga} can be made to Na_{Cu} or Na_{Ga} with the substitution by Na atoms on the defect site, and their density may change with the Cu/Ga ratio. Also, the intensity of the transition between Na-related acceptor state, which is Na_{Ga}, and the major donor state, V_{Se}, may change by the annealing of as-grown CGS film with Se ambient.

In this research, the defect states in epitaxial CGS films were studied experimentally using PL measurement on samples in which the Cu/Ga ratio was varied. Also, the effects of Na addition and annealing in a Se ambient on the defect states were studied by comparing the PL spectra of the Na-dosed CGS films and Se-annealed CGS films with those of as-grown films. The assignment of each defect state obtained by PL

spectra was performed by comparing its energy level with the values in the Tables 1-3 and 1-4.

Table 1-2. Energy levels below conduction band edge and the formation energy for donors in CIS

Donor state	Theory	Experiment
Cu_i	200 meV [Zha98]/ $\Delta H_f = 2.88$ eV	80 meV[Sch98]
In_i	-	132 meV[Sch98]
In_{Cu}	250 meV [Zha98]/ $\Delta H_f = 3.34$ eV	46 meV[Sch98], 25 meV[Sch99, Sch00c]
V_{Se}	-	80 meV[Sch97a], 60 meV[Sch00c,Sch99]

Table 1-3. Energy levels above valence band edge and the formation energy for acceptors in CGS

Acceptor state	Theory	Experiment
Cu_{Se}	-	
Cu_{Ga}	290 meV [Zha98]/ $\Delta H_f = 1.41$ eV	3.5 meV[Yam97], 10 meV[Bau00]
V_{Ga}	190 meV [Wei98]/ $\Delta H_f = 2.83$ eV	20 meV[Sch00b]
V_{Cu}	10 meV [Wei98]/ $\Delta H_f = 0.66$ eV	53 meV[Sch96], 60 meV[Sch99], 50 meV[Bau00],55 meV[Sch00c]
Na_{Ga}	-	

Table 1-4. Energy levels below conduction band edge and the formation energy for donors in CGS

Donor state	Theory	Experiment
Cu_i	210 meV [Wei98]/ $\Delta H_f = 3.38$ eV	-
Ga_i	-	-
Ga_{Cu}	490 meV [Wei98]/ $\Delta H_f = 4.22$ eV	130 meV[Sch99, Sch00c]
V_{Se}	-	80[Sch96, Yam96, Sch99, Bau00, Sch00c], 108[Yam97]

1.1.6 Review of the Study on the Effects of Grain Boundaries

1.1.6.1 Impact of GBs on CIGS Cells

It is obvious from the above review that free-standing single crystals or epitaxial films have been used to eliminate or minimize the effects of grain boundaries (GBs) in the studies on defects in CIS or CGS. There is evidence that GBs influence cells through

their impact on the defect chemistry. It should be pointed out, however, that the highest efficiencies 19.5% [Sur05] were obtained for polycrystalline CIGS materials and there is no report on cells made from single crystal or epitaxial CIGS films that have similar efficiencies to the polycrystalline CIGS films. It is noted that it has not been reported that it is possible to convert the conductivity type of the top thin layer of the CGS epitaxial films from p-type to n-type and thus to produce a buried junction, as is believed to exist in polycrystalline CIGS materials. It thus seems interesting to study the effect of grain size and the density of trap states at GBs on the performance of cells.

1.1.6.2 Studies on GB Effects using a One-Dimensional Model

There have been several studies of GB effects on cell performance, both theoretical and by simulation. Most models assume that trap states at the GB play a dominant role in determining the electrical and photovoltaic properties by acting as carrier traps and recombination centers.

Card *et al.* [Car77] studied the effect of grain size on the device parameters theoretically by using an effective minority carrier lifetime. They calculated the open circuit voltage as a function of grain size, which showed good agreement with experimental values. Fraas *et al.* [Fra78] presented a qualitative model describing the effect of GBs in polycrystalline heterostructure solar cells. They considered possible combinations of GBs in the heterojunction structure of window and absorber layers such as GB region with the depletion of carriers, GB region with higher doping density than bulk, GB region with a different conductivity type (e.g., n-type GB region in p-type absorber layer). Their analysis suggested that GBs with high doping density (p^+) in the lightly doped absorbing layer (p^-) can produce a surface field at the GB, which results in a reduction of recombination at the GB and an increase in the short circuit current due to

the repulsion of minority carrier, electrons at GBs. Ghosh *et al.* [Gho80] studied the effects of GBs in the polycrystalline silicon solar cells by considering recombination centers localized at the GBs as distributed throughout the grains with an equivalent bulk density. They calculated the effective minority carrier life time and the diffusion length from the effective density of the recombination centers at GBs and, from these parameters and the minority carrier diffusion equation, they calculated the dark saturation current, short circuit current, open circuit voltage, and the efficiency as a function of grain size. Their results predicted an increase in V_{OC}, I_{SC}, F.F., and η with increasing grain size , but a decrease in the dark saturation current due to the recombination. Their results indicated that the recombination loss at GBs is the predominant loss mechanism in polycrystalline solar cells. Their calculations also showed excellent agreement with the experimental data.

Seager *et al.* [Sea81] performed calculations that resulted in variable barrier height and recombination velocity at the GBs with a uniform illumination by imposing a quasi-neutrality assumption. They assumed that the regions with no fixed charge (outside of the GB depletion region) are field-free and at low injection. With this assumption, they calculated the barrier height and the quasi-Fermi level self-consistently. Their calculations showed that the majority carrier currents are described by thermionic emission expressions and that the barrier height decreases with increasing injection level and its dependence decreases with decreasing barrier height. Their results also showed good agreement with the experimental results from silicon bi-crystals. Another self-consistent calculation that included the barrier height and recombination velocity with light injection was performed by Oualid *et al.* [Oua84]. In their work, it was assumed that

the minority carrier quasi-Fermi level (E_B) bends in the GB space charge and quasi-neutral regions. From their calculation, they showed that the effective recombination velocity is nearly proportional to $\exp(E_B/kT)$ when E_B is low and the quasi-Fermi level is nearly flat in the space charge region, When E_B, is high, it is limited by the thermal velocity. Chen *et al.* [Che90] performed calculations on the effect of illumination and grain size on the GB potential and minority carrier properties. They solved the coupled equations of GB potential and quasi-Fermi level by considering the dynamic balance between capture process and the emission of carriers at the GBs. From their work, they suggested that the GB potential decreases rapidly with increasing doping level and the light injection effect is much more significant for the low doping case.

The effect of vertical and horizontal GBs in both the depletion and bulk regions of a solar cell were studied by a perturbation approach in Green's work [Gre96]. The effect of the orientation of GBs was studied by varying the recombination velocity and minority carrier lifetime. The effects of GB orientation in both the quasi-neutral and depletion regions of a p-n junction were also explored. In their study, it was proposed that a GB had the largest effect when it was located in the quasi-neutral region at thermal equilibrium. Also, it was observed that the GB effect was reduced in the junction depletion region at thermal equilibrium and in the neutral region away from thermal equilibrium. It was also predicted that GB impact was greater for vertical GBs than horizontal ones. A comparison of numerical simulation results with those from semi-analytical models was performed by Edmiston *et al.* [Edm96]. DESSIS software [Des96] was used in their simulation. They showed the limitation of the concept of the effective

recombination velocity, and the recombination at the GB becomes more important when the grain boundary passes through the depletion region of the p-n junction.

In summary, one-dimensional models have shown that the GBs have an impact on all device parameters such as V_{OC}, J_{SC}, F.F., η, and J_0 through the grain size, the density of GB recombination centers or minority carrier life time. One-dimensional models, however, have limitations in considering the effect of the electric field in the junction depletion region on the effect of GBs, the effect of the orientation of GBs, and the coupled effect of the two (GB orientation effect and the effect of the junction depletion region. Thus it is necessary to explore 2 and 3-D models.

1.1.6.2 Studies on GB Effects using a Two-Dimensional Model

Current flow across GBs in polycrystalline silicon films was analyzed using two-dimensional simulations by Kimura *et al.* [Kim01a]. In this model the current paths were nearly perpendicular to the GBs and also tend to avoid the vertex of the grains, where the proximity of multiple GBs gives higher potential barriers. In another paper [Kim01b] the same group performed simulations that showed that defect states at the GBs trap free carriers as well as form potential barriers. They also investigated the effect of GBs on the energy band alignment and the carrier density through varying the defect density and grain size, as well as other parameters. Two-dimensional device simulations were also performed on the thin film silicon solar cells by Matsui *et al.* [Mat01] to investigate the effect of the GBs on the device performance. The GB effect was modeled by including a vertically oriented grain boundary in a p-i-n structure and varying parameters such as recombination velocity, thickness of the i layer, and the grain size. In their simulation, it was suggested that J_{SC} is relatively stable compared to other performance parameters

such as V_{OC}, F.F., and η. Another two-dimensional simulation was performed for silicon solar cells by Ishikawa *et al.* [Ish01] using the software package MEDICI (Avant! Co.). In their simulation, a right-cylindrical geometry was used to simulate the grains with a columnar structure. They did not solve the problem self-consistently, but rather fixed the GB recombination velocity. Their results point to a minimum recombination velocity at GB is required for the high efficiencies.

In summary, two-dimensional model showed the same tendency of the GB effect on the device parameters as that of one-dimensional model. Two-dimensional model, however, suggested that the transport of carriers is affected by GBs by showing that the current flow line is normal to the GBs. While one dimensional GB model was solved either by using recombination velocity at GBs or by solving the governing equations self-consistently, two-dimensional GB problems were only solved by using the recombination velocity and have never been solved self-consistently.

1.1.7 GB Models for CIGS cells

The GBs are usually composed of the dangling bonds or precipitates of the elements that might have a different composition from the bulk. The GB model that has been most widely used in the simulation is the recombination centers or trap states localized at the GBs [Bar47]. The dangling bond can act as a hole trap as well as the recombination center between the trapped holes and the electrons. This model suggests that there are positive charge build-up at GBs, and the band bending of both conduction band and valence band at GBs. The potential barrier at GBs was first observed in Seager and Pike's work [Sea79]. They measured the barrier potential (100 ~ 400 meV) at GBs by using accurate current-voltage measurement and conductance measurement for Si-

bicrystal. From their measurement, they proposed the existence of the GB potential due to the majority carrier traps at GB. The decrease of the GB potential with illumination was also observed in their different work [Sea81]. Recently, the potential barrier at GBs in CIGS-based solar cells with high efficiency (19.2%) was measured by scanning Kelvin probe microscope [Jia04], and the existence of the local built-in potential (~ 150 meV) at GBs and positive charge build up at GBs were proposed by them. However, this model cannot explain the reason why the polycrystalline CIGS materials with many GBs have the record efficiency that has not been achieved by single crystal or epitaxial CIGS materials with less or no GBs.

Another possible GB model is the existence of the GB barrier only to holes in the grain interior as in Persson and Zunger's work [Per03]. From the first principles calculation, they suggested the V_{Cu}-based reconstruction of the GB surface that is (112) polar surface and most stable in CIGS material. From the segregation of the V_{Cu} at GBs, they proposed the removal of the Cu atoms at GB reduces the p-d repulsion and lowers the valence band maximum at GBs, which results in the downward bending of the valence band and barrier to the holes moving to GBs. Therefore, their model can explain the GB potential without imposing a charge at GBs. By the absence of holes at GBs, they proposed that the electrons in the grain interior are free to move through GBs without recombining with holes. They attributed this to the explanation about the puzzle of having polycrystalline CIS-based solar cells with better efficiencies than their crystalline counterparts. However, their model cannot explain the decrease of GB potential with illumination.

The other possible model is the segregation of a different phase at GBs. It was observed that there is a segregation of Cu-Se phase on the surface of CIS films with Cu-rich composition [Wad97]. Also, the segregation of the $Cu_{2-X}Se$ phase at GBs was also observed by TEM-EDX analysis in our study that will be discussed in chapter 2. This $Cu_{2-X}Se$ was suggested as a p-type material in the study of $CdS/Cu_{2-X}Se$ solar cell in Mikelsen *et al.*'s work [Mic80]. In their research, the hole concentration in $Cu_{2-X}Se$ with $x = 0.26$ was measured as 4×10^{22} cm^{-3}. Therefore, it indicates that the Cu-Se phase segregated at GBs might have p^+ doping, which will repulse electrons and attract holes from the band bending due to the matching of Fermi level with the grain interior (p). This case is the best combination of GBs with grain interior studied in Fraas *et al.*'s [Fra78] work reviewed in 1.1.6.2. In this case, the recombination at GBs will be greatly reduced, and the short circuit current will increase. This model, however, cannot explain the decrease of GB potential with illumination.

The model for the GBs used in this study considers the trap states to be localized at the GB surfaces. All GB traps were assumed to be located at the midgap energy level ($E_t = E_i$), and both trapping of carriers and Shockley-Read-Hall recombination were considered at GB trap states. The effect of grain size was included in the model by considering the change of carrier lifetime as a function of grain size and effective trap density through the solution of the Poisson equation. A much more detailed description of the model used in this study is given in Chapter 6.

1.2 Experimental Methods

1.2.1 Reactor Specification

In this study, epitaxial films were grown by using a migration-enhanced epitaxy (MEE) reactor, which is a variant of molecular beam epitaxy (MBE) reactor. A photo of

the reactor is shown in Figure 1-7. This photo shows a raised bell-jar, which encloses the reactor, metal sources (Cu, In, Ga), cryoshroud, and supports the chalcogen source (Se). A pure Na source (Knudsen cell), was also installed in the reactor to dose with Na during the growth. The system includes a large rotating platen on which as many as nine 5x5 cm substrates can be loaded.

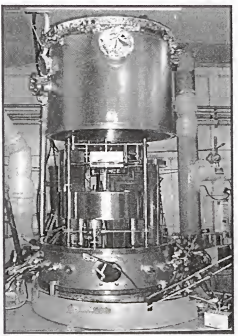

Figure 1-7. Inside view of the MEE reactor

Figure 1-8 displays a schematic diagram of each zone in the reactor. The reactor is designed so that the moving substrate sequentially encounters an impinging flux of metal (Cu and In), a fluxless zone to allow surface migration, and a flux of Se followed by another fluxless zone. By allowing time for migration between deposition zones, the long migration times for adatoms allows improved crystalline quality and the growth of epitaxial films. Standard effusion cells were used for each elemental source in an ultra-high vacuum environment to ensure a molecular-beam flux for each source. Cu and In

source were controlled by electron impact emission spectroscopy (EIES) sensors and Ga source was controlled by the source temperature.

The Na flux was controlled by supplying constant power during the growth, while the Se flux was controlled by maintaining a constant source temperature. The setting was such that the flux ratio of Se/(Cu+III) $\geq$ 5 during the growth. The direction of the platen rotation can be either clockwise or counter-clockwise, so that the sequence of deposition zones may be reversed from metal/Se to Se/metal. A much more complete description of the system and its parts can be found in the thesis of B.J. Stanbery [Sta01].

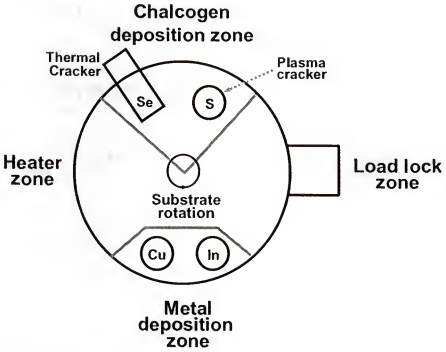

Figure 1-8. Schematic diagram of the each zone in the reactor

1.3 Scope of the Thesis Work

The MEE reactor described above is unique to CIGS growth. The enhanced migration zones along with the relatively low fluxes found in a MBE system should allow

extremely high structural quality when compared to conventional growth methods (e.g., evaporation, sputtering, CVD) at the same temperature. Alternatively, the system should allow growth of the same quality of material as other methods but at a lower growth temperature. Thus, MEE growth of CIS or CGS on single crystal substrates should be able to produce epitaxial films. This gives us the possibility of growing films that minimize or even eliminate GBs. Given this capability, this thesis investigates several objectives.

Objective 1. Grow $CuInSe_2$ epitaxial films at low temperature on GaAs substrates.

Growing epitaxial CIS films is a challenge because of the lack of a suitable substrate. GaAs has a reasonable lattice mismatch (2.26% for CIS on GaAs) and is commercially available in high quality. By lowering the growth temperature, the thermal mismatch as a result of the differences in the thermal expansion coefficients is reduced. Practical non-epitaxial applications of lowering the growth temperature include the use of a larger range of substrates (e.g. polymers) and higher throughput.

At low growth temperature, the mobility of the adatoms on the substrate may not be sufficient for the migration of adatoms and the resulting epitaxial growth. Also, when there is a large lattice mismatch between the film and the substrate, it is likely to have a three-dimensional growth after a very thin critical thickness instead of obtaining epitaxial films with layer-by-layer structure. In this study, temperature profiling (low-high-low) during the initial stage of the growth was used to promote nucleation, to enhance the migration of adatoms, and to ensure the growth by a two dimensional layer-by-layer mode as a metastable state. Also, CIS films with different Cu/In ratio were grown to

exploit the possibility of a Cu-Se secondary phase enhancing the mobility of adatoms for the Cu-rich CIS films.

Objective 2. Growth of epitaxial $CuInSe_2$ and $CuGaSe_2$ films at high temperature on GaAs substrates.

At high growth temperature, the likelihood of obtaining epitaxial CIS and CGS films should be higher. Also, it is possible to have a different growth mode from that at low growth temperature for a different Cu/III (In or Ga) ratio. The point defects of CIS or CGS films are also influenced by the compositions of the films, Na-dosing, and the annealing of as-grown films (e.g. Se ambient). It is also possible that Na may have an effect on the growth mode of films as well as on their defect structure.

In this study, both CIS and CGS films were grown at high growth temperature with different values of the Cu/In or Cu/Ga atomic ratio to exploit the possible surfactant effect of a Cu-Se secondary phase for Cu-rich films, and to compare the growth modes of films with a different Cu/In or Cu/Ga ratio. Na was dosed for CIS and CGS films using the Knudsen cell during the growth. Also, as-grown films were annealed in a Se ambient to study the change of point defect structure. All films were analyzed by X-ray diffraction Spectrometer (XRD), secondary electron microscopy (SEM), transmission electron microscopy (TEM), and photoluminescence (PL) (only for CGS).

Objective 3. Investigate the effect of GBs on the device performance of CIS solar cells

Although the effects of GBs on solar cells have been discussed by several researchers, most of these studies have been 1-D models on Si-based cells. There are very few two dimensional simulation studies on the effect of GBs and there has been no study about GB effect by using both two-dimensional simulation and solving the

continuity and Poisson equations self-consistently. Also, there has been no extensive study on the effect of grain size on cell performance parameters, especially on J_0. J_0 is thought to be related to the carrier transport mechanism for the recombination at GB traps and to show a different dependence on the grain size.

In this study, GB effects were studied by including trap states localized at GBs and considering SRH recombination as well as trapping of carriers at GB trap states. The effective grain size, d_{eff}, was defined and the dependence of J_0 on the grain size was studied to find the different carrier transport mechanism for the recombination at GBs for a different width of the GB depletion region through the grain size. The grain size for the transition of J_0 dependence was also studied by considering the carrier distribution in the grain interior.

CHAPTER 2
EPITAXIAL GROWTH OF $CUINSE_2$ AT LOW TEMPERATURE

2.1 Backgrounds

Although commercial $CuInSe_2$ (CIS)-based cells use polycrystalline thin films, the study of epitaxial CIS films allows one to minimize or avoid the complexities introduced by grain boundaries (GBs). It is well known that the electrical properties of $CuInSe_2$ (CIS) films are strongly dependent on the atomic composition, especially on the Cu-to-In metal ratio, as well as on the growth conditions [Lia02, Nik02, Tiw94]. Films grown under In-excess conditions often show high resistivity and small average grain size. In contrast, films grown under Cu-rich conditions exhibit high crystalline quality, large grain size, p-type conductivity, and typically feature a conductive Cu-Se secondary phase on their surfaces and grain boundaries.

It has been argued that the Cu-Se secondary phase plays an important role in the grain growth mechanism of these films [Roc94, Kle93]. Some researchers observed a significant difference between the surface and bulk compositions of Cu-rich CIGS polycrystalline films, and proposed a growth model in which the Cu-Se secondary phase exists as a liquid or quasi-liquid phase during the growth process, enhancing the transport of the reactants from the vapor phase to the surface of the growing CIS phase [Kle93, Tut95]. This is often referred to as the vapor-liquid-solid (V-L-S) growth mechanism. Using transmission electron microscopy (TEM), Wada *et al.* [Wad97] observed stoichiometric Cu_2Se on the CIS grain surfaces. Fons *et al.* [Fon98] have reported the formation of the same phase $Cu_{2-x}Se$, in Cu-rich CIS films grown epitaxially on (100)

GaAs. They attributed the presence of strain-related surface undulations to the presence of a thin surface layer composed of $Cu_{2-x}Se$ that led to a large grain size and better crystalline quality [Nik99].

At low growth temperature that does not provide the adatom mobility enough for the epitaxial growth, it is required to have another mechanism to enhance the mobility of adatoms on the surface of the substrate. In this study, the growth of CIS films on (100) GaAs substrate was performed with a variation of Cu/In ratio including Cu-rich CIS, In-rich CIS, and stoichiometric CIS films. It is expected that the CIS films will grow epitaxially as Cu/In ratio becomes greater than 1 since it is possible for the excess Cu to form Cu-Se secondary phase and to enhance the surface mobility of adatoms for the epitaxial growth.

2.2 Experimental Approach

Epitaxial growth of CIS films with different Cu/In ratio was tried using the MEE reactor described in Chapter 1. The direction of the platen rotation in the reactor can be either clockwise or counter-clockwise, so that the sequence of deposition zones may be reversed from Se/metal to metal/Se. From the result of the preliminary growth experiments, the direction of the rotation had negligible effect on the surface morphology of the film. In this study, counterclockwise (metal/Se sequence) direction was used at 12 rpm. The background pressure during the deposition process was in the range of 10^{-7} to 10^{-8} Torr. Further details on the deposition system are given in a previous thesis [Sta01].

Semi-insulating GaAs wafers with (001) orientation of 2° off towards the nearest [110] direction were used as the substrate to enhance the step-mediated growth. Simultaneous growth was also carried out on molybdenum-coated glass substrates to

measure the bulk composition of as-grown films. CIS films with different Cu-to-In ratios were grown on the GaAs substrates to determine the effect of the metal ratio on the phase and structural properties of the films.

As CIS and GaAs have a large lattice mismatch (2.26%) for the in-plane lattice constants and the growth temperature is relatively low, a three-temperature sequence was used during the initial stage of growth to grow epitaxial films. Film growth was initiated with a substrate temperature of approximately 360 °C. After a CIS with the thickness of ~8 nm was deposited, as determined by calibration, the substrate temperature was increased to 412 °C. Growth continued until the thickness reached 40 nm, at which point the temperature was decreased to the initial value of 360 °C and bulk growth of the film was performed. This temperature profile was designed to generate as many nucleation sites as possible during the first temperature stage, and then to enhance two-dimensional growth or layer-by-layer growth during the second temperature stage. The third step, namely the return to the initial growth temperature, was used to suppress the formation of dislocations after a considerable film thickness had been established. All CIS films were grown to a thickness of 0.5 μm with a relatively low growth rate of 0.57 Å/s.

In this study, a series of films was grown on (001) GaAs to study the influence of the Cu/In ratio on the growth mechanism and structural quality of the films. In this Chapter, 3 films were selected for detailed compositional and structural quality study. One film was In-rich (sample W366), another slightly Cu-rich (sample W369), and the other more Cu-rich (W367). The following section 2.3 summarizes the composition, surface morphology, and phase chemistry of the films. Section 2.4 shows the results of

detailed TEM analysis of the island structure, while section 2.5 summarizes the strain energy distribution in the heterostructure.

2.3 Composition, Phase and Surface Morphology of Epitaxial Films

The bulk composition of each CIS film was measured using films grown on molybdenum-coated glass at the same time by Inductively-Coupled Plasma Optical Emission Spectroscopy (ICP-OES), which has a ± 0.5 atomic % estimated error. The measured compositions are summarized in Table 2-1. Sample, W366 has a slightly In-rich composition, while sample W369 and W367 have Cu-rich composition. It is also seen that Se composition decreases as the film goes from an In-rich to Cu-rich composition, which is typically observed [Fon98]. The surface morphology of the films was investigated using a JEOL JSM-6335F field emission scanning electron microscope and the morphologies of each film at low magnification (3,000X) and at high magnification (30,000X) are shown as from Figures 2-1 to 2.3.

Table 2-1.Bulk composition of three CIS films on Mo-coated glass determined by ICP.

Sample	Cu (at. %)	In (at. %)	Se (at. %) (Δs)	Cu/In (Δm)	Growth rate (Å/s)
W366	24.90	25.34	49.76 (-0.017)	0.98 (-0.014)	0.57
W369	25.90	25.28	48.82 (0.025)	1.02 (-0.040)	0.57
W367	26.68	24.38	48.93 (0.094)	1.09 (-0.020)	0.58

The low magnification image of the In-rich film (Figure 2-1a) shows that there are two regions in the film (bright irregularly shaped spot in a grey matrix background). The brighter areas in the low magnification image are irregularly shaped with no apparent orientation. High magnification image (Figure 2-1b) reveals that the bright areas are a collection of submicron grains while, in the grey background region, the average feature

size is considerably small. Two Cu-rich films (W369 and W367) show an island structure with large faceted grains embedded in a smooth connected background region. This background matrix region appears to be textured with good orientation and the long axis of the textured structure is in the [0 1 –1] direction of the substrate. The orientation of this matrix region will be discussed in detail in section 2.5. From the higher magnification image, it is also observed that the grain size of W366 is on the order of 200 nm, while the grain size in two Cu-rich samples is in the range of 0.5 to 1 μm.

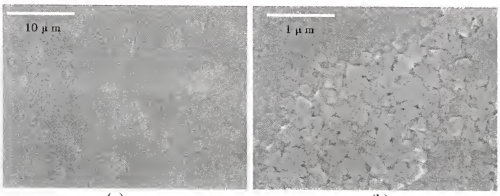

(a) (b)

Figure 2-1. SEM images of the surface of the In-rich sample Cu/In = 0.98 (W366): (a) 3,000X, (b) island region at 30,000X

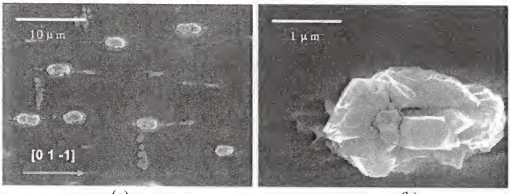

(a) (b)

Figure 2-2. SEM images of the surface of the In-rich sample Cu/In = 1.02 (W369):

(a) 3000X, (b) island region at 30,000X

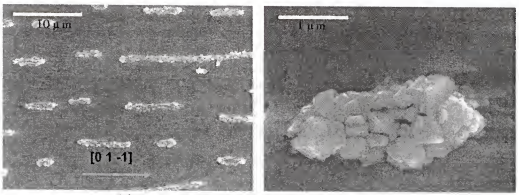

(a) (b)

Figure 2-3 SEM images of the surface of the Cu-rich sample Cu/In = 1.09 (W367) (a) 3,000X, (b) island region at 30,000X

From the previous bulk composition results and the large grain size for the Cu-rich films, it is likely that Cu-Se secondary phase exists in the Cu-rich films. Electron Probe Microanalysis (EPMA) examination of both the matrix and the island regions of the CIS films were next performed to determine if the island regions differ in composition. The results are summarized in Table 2-2, which shows the measured atomic composition and the calculated Cu-to-In ratio for each region. For EPMA, a JEOL Superprobe 733 was used with an accelerating voltage of 6 keV and with an estimated accuracy of ±0.5 at. %. At this accelerating voltage, it has an estimated probe depth of 200 nm. From the results presented in Table 2-2, it is concluded that within the estimated measurement error there is essentially no difference between the compositions of the two regions for the In-rich sample (W366). For samples W369 and W367, which have a nearly stoichiometric or slightly Cu-rich bulk composition (Table 2-1), the matrix region was slightly Cu-rich whereas the composition of island areas was highly Cu-rich (Table 2-2). It has been suggested that Cu-rich CIS films have a segregation of a Cu-Se phase [Kle02]. At this

point it was hypothesized that all or part of an island region is composed of a Cu-Se secondary phase, or that a Cu-Se phase exists at the grain boundaries in the island regions.

Table 2-2 EPMA analysis for the matrix and island regions of each CIS film grown on (100) GaAs substrates.

Sample	Matrix Region				Island Region			
	Cu (at.%)	In (at. %)	Se (at. %)	Cu/In	Cu (at. %)	In (at. %)	Se (at. %)	Cu/In Or Cu/Se*
W366	25.24	25.53	49.22	0.99	25.27	25.37	49.36	1.00
W369	25.96	24.51	49.53	1.06	48.38	7.50	44.13	1.67*
W367	26.85	23.91	49.25	1.12	50.07	6.14	43.80	1.59*

*: Cu/Se ratio after subtracting $CuInSe_2$ composition.

It is also observed that for samples W369 and W367, the estimated Cu to Se ratio in the island areas was 1.6 ~ 1.7 assuming that any $CuInSe_2$ in the region has a 1:1:2 stoichiometry. This analysis implies that a Cu-Se secondary phase exists in both the island and matrix regions, but mostly segregated to the island area. To further probe the existence of a Cu-Se secondary phase, SEM and EPMA analyses were again performed, but after treating the CIS films with a 10% KCN solution to selectively etch any Cu-Se secondary phases. The micrographs shown in Figures 2-4 to 2-6 are again low (3000X) and high (30,000X) magnification SEM images of the same samples shown in Figures 2-1 to 2-3. It is seen that there is no significant morphological change in the films before and after etching, except for an increase of the gap between grains in the island regions. These observations suggest that a Cu-Se secondary phase mainly exists at the grain boundaries in the island regions or to a lesser extent on the surface of the matrix region.

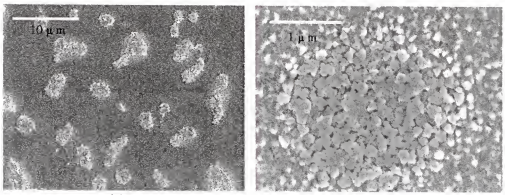

(a) (b)

Figure 2-4 SEM images of the surface of the Cu-rich sample Cu/In = 0.98 (W366) after etching in 10 % KCN. (a) 3,000X, (b) island region at 30,000X

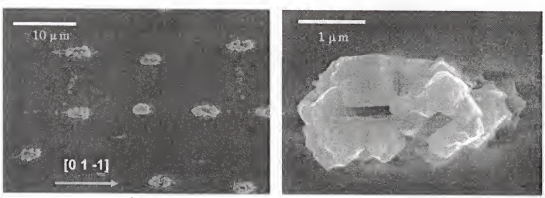

(a) (b)

Figure 2-5 SEM images of the surface of the Cu-rich sample Cu/In = 1.02 (W369) after etching in 10 % KCN: (a) 3,000X, (b) island region at 30,000X

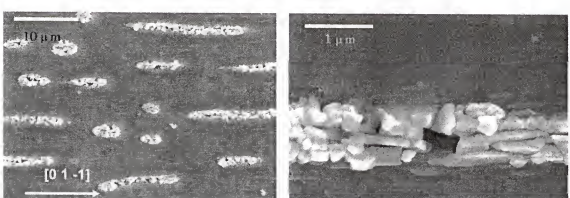

(a) (b)

Figure 2-6. SEM image of the surface of the Cu-rich sample Cu/In = 1.09 (CIS3) after etching in 10 % KCN: (a) 3,000X, (b) island region at 30,000X

Table 2-3. EPMA analysis for the matrix and island region of each CIS film grown on (100) GaAs after etching in 10% KCN.

Sample	Matrix Region				Island Region			
	Cu (at.%)	In (at. %)	Se (at. %)	Cu/In	Cu (at. %)	In (at. %)	Se (at. %)	Cu/In
W366	25.40	24.71	49.89	1.03	25.16	24.91	49.93	1.01
W369	25.79	24.75	49.46	1.04	26.08	24.09	49.83	1.08
W367	25.86	24.69	49.45	1.05	25.35	25.12	49.53	1.01

The compositions summarized in Table 2-3 reveal that the matrix region changed only slightly after etching and always by less than 1 at. %. The island regions of the In-rich sample (W366) also showed only a slight change in composition. This is in contrast to the island regions for the two Cu-rich samples (W369 and W367), in which the Cu and In, and to a lesser extent the Se, composition changed significantly and consistent with removal of a Cu-Se phase. The change in composition after etching was in a direction to produce an almost stoichiometric but slightly Cu-rich composition, as reported in Table 2-3. These results reinforce the hypothesis that a Cu-Se secondary phase exists at the grain boundaries in the island region.

To establish the relative locations of the island region and possibly identify the growth mode for the Cu-rich CIS films, cross-sections of both the matrix and island regions of each sample were analyzed (Figures 2-7 through 2-9). From Figure 2-7, it is clear that sample W366 (In-rich) was not grown epitaxially and its growth mode was 3-D or Völmer-Weber type. Thus epitaxial growth did not occur for the In-rich composition at this low growth temperature. For both Cu-rich films, the micrographs of the matrix region reveal the thickness of the film is very uniform (0.4 μm). In contrast, the micrographs of the island region show a thicker matrix layer of 0.6 μm and a multi-grain

structure above the matrix, which suggest that Cu-rich CIS films were grown in Stranski-Krastanov (S-K) growth mode.

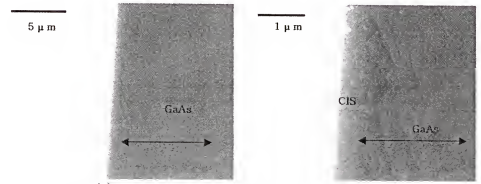

Figure 2-7 SEM images for the cross-section of the Cu-rich sample with Cu/In = 0.98 (W366):(a) 5,000X, (b) island region at 20,000X

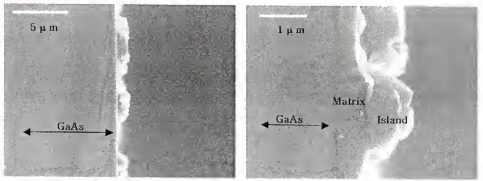

Figure 2-8 SEM images of the cross-section of the Cu-rich sample with Cu/In = 1.02 (W369):(a) 5,000X, (b) island region at 20,000X

To assess the film orientation relative to the GaAs substrate, high resolution XRD ω–2θ scans were taken for each sample after etching to produce the spectra displayed in Figures 2-10 to 2-12. The spectrum for the In-rich sample shown in Figure 2-10 confirms that epitaxial growth did not occur, but that the film was single phase chalcopyrite CIS

(denoted in the figure by Ch-CIS) with a preferential orientation given by the polar (112) plane parallel to the substrate plane.

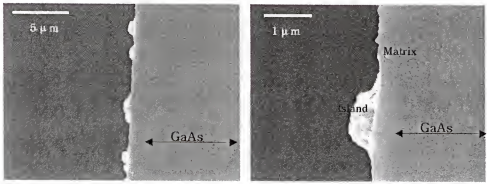

Figure 2-9 SEM images of the cross-section of the Cu-rich sample with Cu/In = 1.09 (W367):(a) 5,000X, (b) island region at 20,000X

When the Cu-to-In ratio was slightly larger than 1, as for sample W369 (nominally Cu/In=1.02), the XRD spectrum was consistent with Ch-CIS grown epitaxially on GaAs (Figure 2-11).

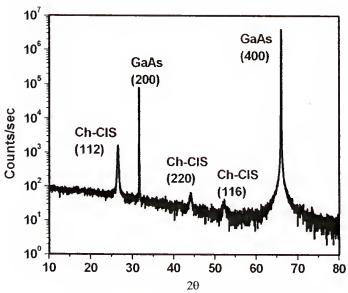

Figure 2-10. XRD ω–2θ scan of In-rich sample with Cu/In=0.98 (W366) after etching with 10% KCN.

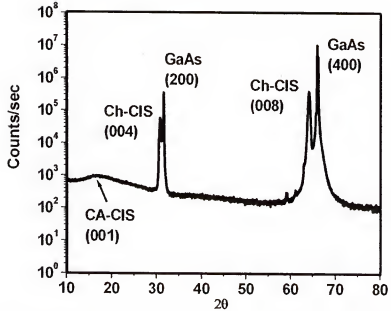

Figure 2-11. XRD ω–2θ scan of Cu-rich sample with Cu/In=1.02 (W369) after etching with 10% KCN.

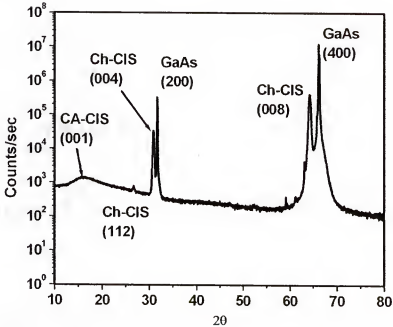

Figure 2-12. XRD ω–2θ scan of Cu-rich sample with Cu/In=1.09 (W367) after etching with 10% KCN.

In addition, a broad peak attributed to Cu-Au-like CIS (CA-CIS) was observed in the spectrum for this sample. This structure differs from the chalcopyrite one by ordering

existing in two cation planes in the (001) direction and requires translation of the cation plane in the [110] direction.

The most Cu-rich film, (W367, nominally Cu/In=1.09), also grew epitaxially as evidenced by the spectrum shown in Figure 2-12. Further increase of the Cu-to-In ratio, as in sample W367, however, did not improve the crystalline quality of the film, given that the ratio of the Ch-CIS (008) peak to the GaAs (400) peak is almost the same (0.038 for W369 and 0.033 for W367) in Figures 2-11 and 2-12, respectively, and the values of the FWHM for ω-rocking curves were nearly identical (0.3 degree) (Figure 2-13).

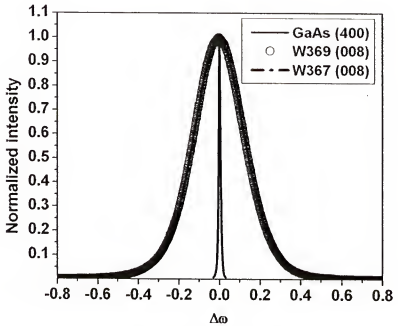

Figure 2-13 XRD ω–rocking curve for (008) plane of Cu-rich samples, W369 and W367 after etching with 10% KCN

It is concluded from the set of XRD scans and SEM micrographs that the textured structure of the matrix region for the two Cu-rich CIS films has a CH-CIS structure with epitaxial orientation. The XRD spectra were also taken for the CIS films with a Cu-rich

composition before the KCN etching (e.g., Figure 2-14), but no peak attributable to a Cu-Se phase was detected, suggesting that there was either a very small amount of this binary phase or it was amorphous.

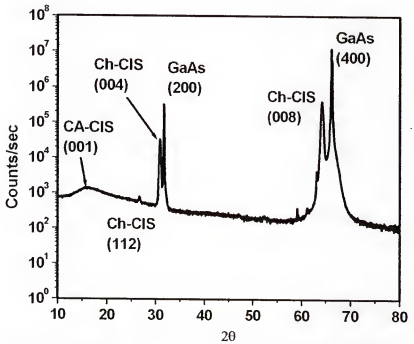

Figure 2-14. XRD ω–2θ scan of Cu-rich sample with Cu/In=1.09 (W367) before KCN etching.

The amount and composition of the Cu-Se phase was estimated using the composition data in Tables 2-1. From the ICP analysis, the amount of each element is Cu = 3.474×10^{-6} mole, In = 3.227×10^{-6} mole and Se = 6.462×10^{-6} mole. So, if it is assumed all In resides in the $CuInSe_2$ phase, the excess Cu and Se, after accounting for the Cu and Se in the $CuInSe_2$ phase is Cu = 2.470×10^{-7} mole, Se = 8.000×10^{-9} mole. Therefore, the amount of the Cu-Se secondary phase, which is determined from the Se is ~ 3.24% of $CuInSe_2$ phase concentration. This is a maximum estimate and it is thus possible that it can not be detected by XRD or was overwhelmed by the background signal. Figures 2-11,

2-12 and 2-14 (Cu-rich films) show a broad peak near the position of $2\theta=15°$ and it was assigned to the (001) reflection of CA-CIS. Grazing-angle incidence XRD analysis of the etched sample W367 was carried out to investigate the location of CA-CIS phase in the film. As can be seen in Figure 2-15, peaks attributed to CA-CIS were observed along with peaks for Ch-CIS ((112), (211), (202), and (116)). From this result, it is suggested that the CA-CIS phase exists predominantly within the depth of 20 nm from the surface of the film, and that the grains in the island region are a mixture of polycrystalline Ch-CIS and CA-CIS.

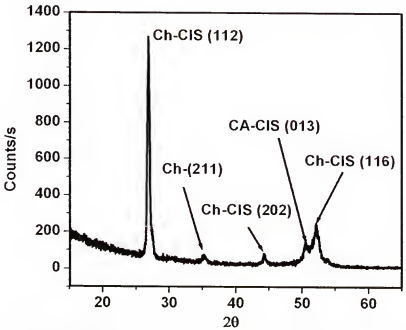

Figure 2-15. Grazing incidence XRD 2θ scan of Cu-rich sample W367 after etching with 10% KCN, $\omega = 0.4°$

A pole figure analysis was also performed on sample W367 to determine the relative orientation of the matrix region of the Cu-rich CIS films with respect to the GaAs substrate. From the results shown in Figure 2-16, it is concluded that the matrix region of

the Cu-rich CIS film has the same orientation as the GaAs substrate with the same plane and crystal directions, which can be represented as $(001)_{GaAs}//(001)_{CIS}$ and $[100]_{GaAs}//[100]_{CIS}$. Therefore, a two-dimensional layer for the matrix region grew heteroepitaxially. No peaks attributable to the CA-CIS phase were found in the pole figure analysis, suggesting that CA-CIS exists in only a very limited amount or as a polycrystalline material.

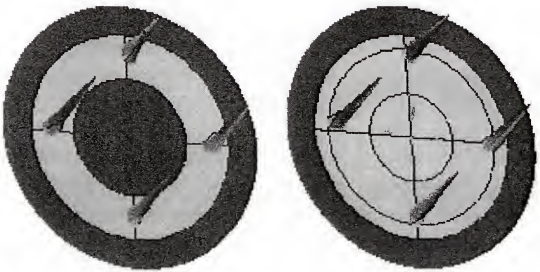

(a) GaAs (111) (b) Ch-CIS (112)

Figure 2-16. Pole figure of Cu-rich sample with Cu/In=1.09 (W367) after etching with 10% KCN

2.4 TEM Analysis of as-grown Epitaxial Films

To further understand the growth habit of CIS on GaAs, cross-sectional TEM was used to view the morphology and the crystal structure of sample W367 after coating with Pt. TEM-Energy dispersive X-ray spectroscopy (EDX) was also used to determine the location of Cu-Se secondary phase. Dark field images of the island and matrix regions are shown in Figure 2-17.

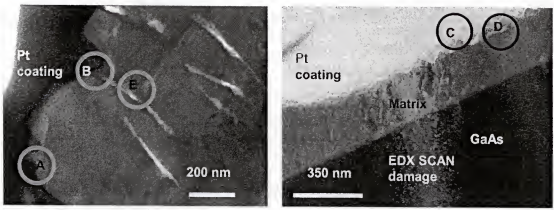

Figure 2-17. TEM cross-sectional images of the Cu-rich sample with Cu/In=1.09 (W367):(a) Dark field image of island region, (b) Dark field image of matrix region

An island region consists of several large grains separated by gaps covered with a Cu-Se compound. To identify the location of Cu-Se secondary phase, TEM-EDX line-scans were taken for areas "A", "B" and "E" in an island region (designated in Figure 2-17a) and areas "C" and "D" in a matrix region (designated in Figure 2-17b). The signal for each element was calibrated by using the standard supplied from NREL. The equation for the quantitative X-ray analysis was proposed by Castaining [Cas51]. He suggested that, for element i, there is a relation between the intensity from the sample, I_i, and that from the standard, $I_{(i)}$ such as $C_i / C_{(i)} = [K] I_i / I_{(i)}$, where C_i is the concentration of each element, I_i is the intensity for each element and [K] is the sensitivity factor that takes into account the difference between the generated and measured X-ray intensities for both for the standard and the unknown specimen. The contributions to K come from three factors: the atomic number (Z), absorption of X-rays within the specimen (A), and fluorescence of X-rays within the specimen (F). This correction is called ZAF correction. If the

specimen is sufficiently thin or electron-transparent, however, the correction procedure can be greatly simplified as the A and F terms can be ignored. For this case, Cliff *et al.* [Cli75] proposed the so-called Cliff-Lorimer equation:

$$\frac{C_A}{C_B} = k_{AB}\frac{I_A}{I_B} \tag{2-1}$$

where C_i is the concentration of element I, I_i is the intensity of the X-ray for element i and k_{AB} is the Cliff-Lorimer factor. Actually, k_{AB} is related to the atomic number correction in the original Castaining's equation. Since there is also mass conservation, e.g., for a binary system, $C_A+C_B = 100\%$, absolute values for C_A and C_B can be calculated. This equation can easily be extended to the ternary system as in our case.

$$\frac{C_{Cu}}{C_{Se}} = \frac{I_{Cu}}{I_{Se}} \times k_{Cu,Se} \quad \frac{C_{In}}{C_{Se}} = \frac{I_{In}}{I_{Se}} \times k_{In,Se} \quad C_{Cu} + C_{In} + C_{Se} = 1 \tag{2-2}$$

For the standard CIS sample, the intensities for Cu $K\alpha_1$, In $L\alpha_1$ and Se $K\alpha_1$ were 1245, 453 and 705 counts. Therefore, from the known composition ratio of 1:1:2 for Cu, In and Se in the standard, $k_{Cu,Se} = 0.283$ and $k_{In,Se} = 0.778$ were calculated by using equation 2-1.

The TEM-EDX depth profile of region A in the island as in Figure 2-18, is shown in Figure 2-19. The elemental profile shows that the Cu concentration is very high near the surface of the island region, and the In and Se concentrations are correspondingly low near the surface. The Cu concentration decreases and then remains constant deeper into the film. This "Cu-rich phase" extends only about 10 nm from the surface. Also, from the observation of In concentration near the surface region, it is suggested that the region near the surface could be a mixture of the CIS phase and the Cu-Se nano-phase.

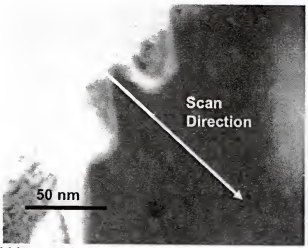

Figure 2-18. Dark field image of region A

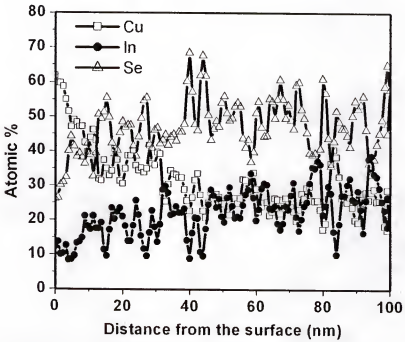

Figure 2-19 TEM-EDX line scan of region A

Figures 2-20 and 2-21 show the dark field image and TEX-EDX depth profile of matrix region. The surface of the matrix region is not flat but has valleys with a period of ~ 150 nm with sides oriented in the {112} direction. The line scan shown in Figure 2-21 indicates that matrix region is also covered with a Cu-rich phase, which extends about 60 nm into the film. TEM-EDX depth profile analyses were also done for region "B", "D"

and "E". They are shown from Figures 2-20 through 2-27 and they showed the same high Cu concentration near the surface.

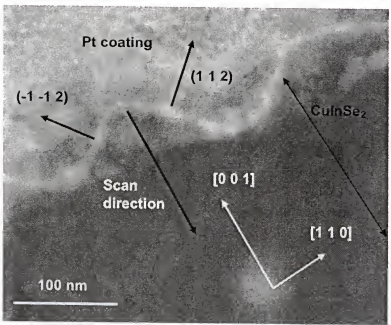

Figure 2-20. Dark field image of region C

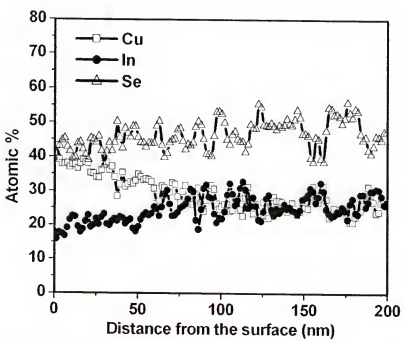

Figure 2-21 TEM-EDX line scan of region C

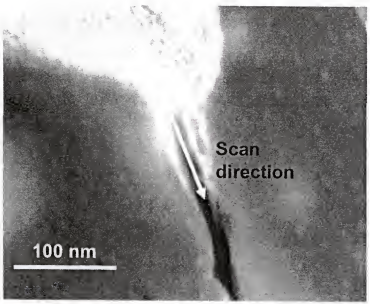

Figure 2-22. Dark field image of region B

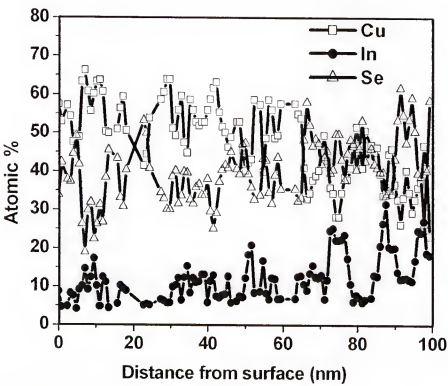

Figure 2-23 TEM-EDX line scan of region B

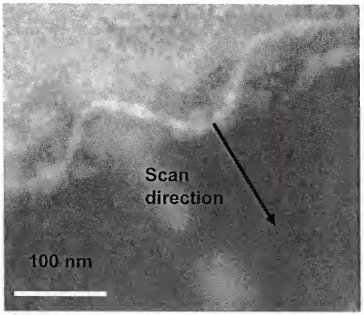

Figure 2-24 Dark field image of region D

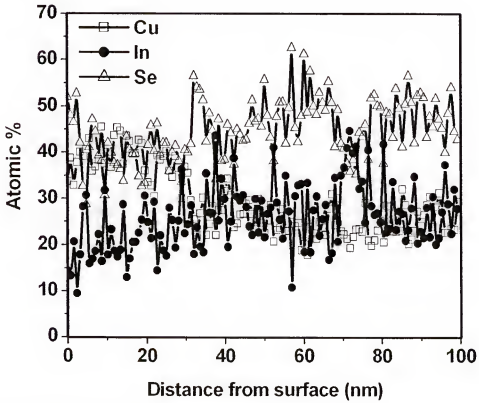

Figure 2-25. TEM-EDX line scan of region D

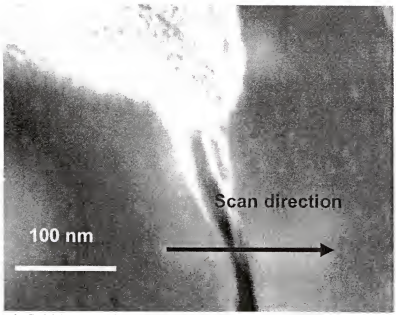

Figure 2-26 Dark field image of region

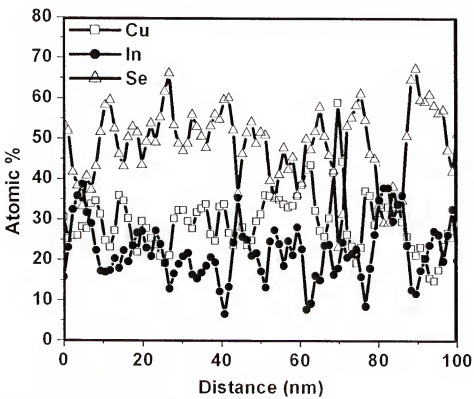

Figure 2-27 TEM-EDX line scan of region E

The composition profile across the island gap (Figure 2-27) shows no remarkable Cu concentration variation and there is only a slight increase of Cu concentration near the gap, which suggests there is no Cu-rich phase at the gap between grains or only a very thin layer of Cu-rich phase resides on the surface of the grains in the gap. From these EDX results, it is concluded that Cu-Se secondary phase mainly exists on the surface of island region and the matrix region or on surface of the grains.

It is also observed from the orientation of the matrix region in Figure 2-20 that the orientation of the matrix surface undulation is close to (112) crystal plane of $CuInSe_2$ as reported by D. Liao *et al.*[Lia02]. It was also reported that the (112) plane of $CuInSe_2$ is stable and the first principles calculations indicate spontaneous decomposition occurs from (220)/(204) surfaces to (112) facets with lowest energy [Zha02].

Selected area diffraction patterns (SADP) of the matrix and island regions were taken at zone axis [-1 -1 0] to check the orientations of these regions as shown in Figure 2-28.

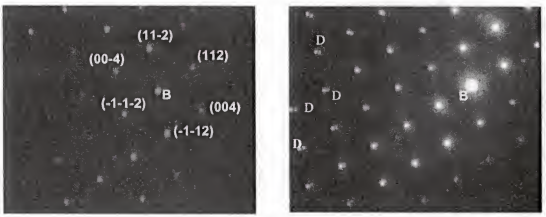

(a) (b)

Figure 2-28. Selected area diffraction pattern for the (a) matrix and (b) island regions: (a) Matrix region:B = [-1-10], (b) island region: B = [-1-10]

Both regions are of the same orientation. There are, however, double spots in the SADP for the island region (denoted as D in Figure 2-28b), and it indicates that the grains in island region are slightly mis-oriented or rotated relative to the orientation of the matrix region. Each grain, however, is a single crystal.

2.5 Strain Analysis of Epitaxial CIS Film Grown at Low Temperature

When there is a lattice mismatch between the substrate and the film, the film can be unstrained if a sufficient number of misfit dislocations form at the interface between the substrate and the film to reduce the strain. Alternatively, the film lattice can deform to account for the mismatch and match the same lattice constant as the substrate (pseudomorphic film). Or films can grow pseudomorphically initially and then after a critical thickness, the strain can be reduced with the formation of misfit dislocations. Given the lattice parameters a = 5.784 Å, and c = 11.616 Å for CIS [Cha03], the lattice mismatch between a CIS film and GaAs substrate is 2.26% at room temperature, which is relatively large. Therefore, epitaxial CIS films with Cu-rich composition should contain residual strain. The strain or the change of lattice parameters can be obtained by XRD space map. The method of calculating the in-plane and the perpendicular lattice parameters was proposed for a fully strained or fully relaxed layer, which do not use the differentiated form of Bragg's law [Slu93].

For a cubic crystal with (001) plane parallel to the surface with an epitaxial layer on top, the following expression can be defined as the in-plane and the perpendicular lattice mismatch relative to the substrate,

$$(\frac{\Delta a}{a})_{\perp} = \frac{c_n - a_s}{a_s},\ (\frac{\Delta a}{a})_h = \frac{a_h - a_s}{a_s} \qquad (2\text{-}3)$$

where a_s, a_h and c_n are the lattice constant of the substrate, the lattice constant of the film parallel to the surface and lattice parameter of the film perpendicular to the surface, respectively. In this case, a_h and c_n can be evaluated from a series of $2\theta-\omega$ scans or a space map in reciprocal space.

Figure 2-29 shows [001]/[110] section in real and reciprocal space of a fully relaxed epitaxial layer on a substrate. In Figure 2-29, k_{in} is the incoming X-ray vector and k_{out} is outgoing X-ray vector. Also, $K_{//}$ is the reciprocal lattice vector in [110] direction,

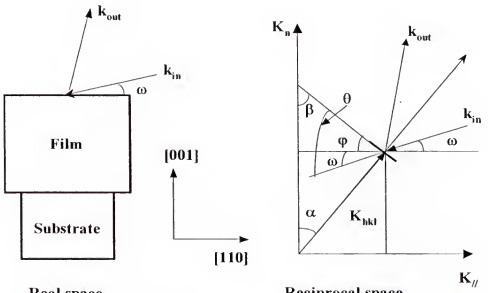

Figure 2-29. Relation between X-ray and film in real space and the reciprocal space

K_n is that in [001] direction and K_{hkl} is the reciprocal lattice vector of the tilted crystal plane of the film. For the angles in the Figure 2-29, ω is the angle between (001) plane of the film and the incoming X-ray, φ is the angle between (001) plane and the (hkl) plane of the film with following relations between these angles,

$$\alpha+\beta=\frac{\pi}{2},\quad \beta=\frac{\pi}{2}-\varphi,\quad \alpha=\frac{\pi}{2}-(\frac{\pi}{2}-\varphi)=\varphi \tag{2-4}$$

There are also relations among the reciprocal vectors K_n, $K_{//}$ and K_{hkl} :

$$K_n = K_{hkl} \bullet \cos(\varphi), \quad K_{//} = K_{hkl} \bullet \sin(\varphi), \quad as \quad \alpha = \varphi \tag{2-5}$$

Next, the equation for the lattice parameters must be determined from the relation between the reciprocal vectors and angles, which can be obtained from space map. As K_{hkl} is a reciprocal lattice vector, $K_{hkl} = \frac{2\pi}{d_{hkl}}$ holds between the reciprocal lattice vector and the lattice parameter of the corresponding crystal plane. Equation (2-5) can be written as the relations between lattice parameters,

$$\frac{2\pi}{d_n} = \frac{2\pi}{d_{hkl}} \bullet \cos(\varphi), \quad \frac{2\pi}{d_{//}} = \frac{2\pi}{d_{hkl}} \bullet \sin(\varphi) \tag{2-6}$$

As K_{hkl} is the sum of K_n and $K_{//}$, $K_n = K_{00l}$ and $K_{//} = K_{hk0}$. Defining $k_{hkl} = K_{hkl}/2\pi$, $d_{hkl} = 1/k_{hkl}$ and from the Bragg reflection condition, $d_{hkl} = \frac{\lambda}{2\sin(\theta_{hkl})}$, and Equation (2-5), k_{00l} and k_{hk0} are defined as :

$$\begin{aligned} k_{00l} &= k_{hkl} \bullet \cos(\varphi) = k_{hkl} \bullet \cos(\theta - \omega) = \frac{2\sin(\theta_{hkl})}{\lambda} \bullet \cos(\theta - \omega) \\ k_{hk0} &= k_{hkl} \bullet \sin(\varphi) = k_{hkl} \bullet \sin(\theta - \omega) = \frac{2\sin(\theta_{hkl})}{\lambda} \bullet \sin(\theta - \omega) \end{aligned} \tag{2-7}$$

Finally, the in-plane lattice constants, d_{100}, and the lattice constant perpendicular to the surface, d_{001} are written as,

$$d_{00l} = \frac{1}{k_{00l}}, \quad d_{hk0} = \frac{1}{k_{hk0}}, \quad d_{001} = \frac{l}{k_{00l}}, \quad d_{100} = \frac{\sqrt{h^2 + k^2}}{k_{hk0}} \tag{2-8}$$

To analyze the strain in the epitaxial film, the Cu-rich sample (W367) was selected and a space map was done for the (2 2 4) plane of GaAs and (2 2 8) plane of CIS. The X-ray was a mixture of Cu $K\alpha_1$ and Cu $K\alpha_2$ with the intensity ratio of $K\alpha_1$ to $K\alpha_2 = 2$. A

1/2 inch slit and 4-bounce hybrid monochromater with four Ge (220) single crystals were located immediately after the X-ray tube and an open detector was used. Figure 2-30 is the result of the space map, from which 2θ and ω positions for each plane were obtained as (2θ, ω) = (83.129°, 6.005°) for the GaAs (-2 -2 4) crystal plane and (2θ, ω) = (81.839°, 5.855°) for CIS (-2 -2 8) crystal plane.

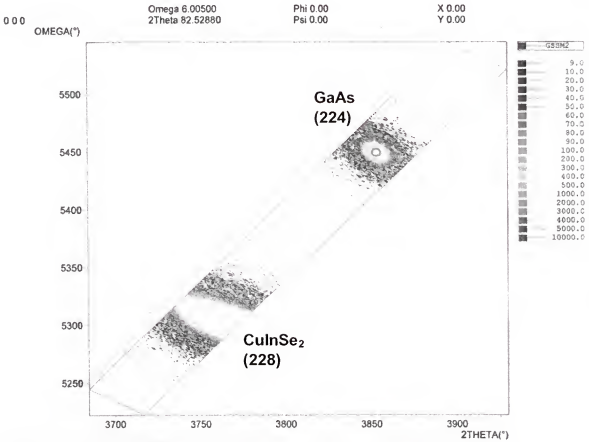

Figure 2-30. Space map for (2 2 4) plane of GaAs and (2 2 8) plane of CIS for Cu-rich CIS (sample W367)

To calculate the exact lattice parameter for CIS, the offset between the theoretical lattice parameters of GaAs and those from the measurement should be considered. The theoretical peak positions for GaAs were generated by using Tkatom [Rav01], which is one of the modules of IFEFFIT software for the analysis of the extended absorption fine

structure spectrum and summarized in Table 2-4. From this Table, the 2θ position for (2 2 4) plane is 83.736° and the experimental values of the offset for 2θ is calculated ($\Delta\theta = \theta_{theo} - \theta_{exp} = 0.6072°$). Also, as $\theta = \omega + \varphi$ and $\varphi = 35.264°$, the theoretical value for $\Delta\omega = 6.604° - 6.005° = 0.599°$. From these offset values, the experimental values of 2θ and ω for CIS (-2 –2 8) plane are calculated as 82.446° and 6.454°, respectively.

Table 2-4. Theoretical peak positions for GaAs: Space group (Fm-3m), λ = 1.54056Å

2θ	Crystal plane (h k l)	Calculated intensity
27.297	(1 1 1)	100.00
31.623	(2 0 0)	0.122
45.329	(2 2 0)	73.012
53.724	(3 1 1)	43.254
56.320	(2 2 2)	0.038
66.042	(4 0 0)	11.356
72.860	(3 3 1)	16.938
75.073	(4 2 0)	0.077
83.736	(4 2 2)	22.765
90.129	(5 1 1)	9.747
100.828	(4 4 0)	8.112
107.411	(5 3 1)	15.474
109.654	(6 0 0)	0.018
119.011	(6 2 0)	15.834
126.597	(5 3 3)	8.607
129.295	(6 2 2)	0.096
141.425	(4 4 4)	7.323
153.272	(7 1 1)	15.420
158.477	(6 4 0)	0.231

From equations (2-6) and (2-7) and the 2θ and ω values, $k_{00l} = 0.70278$ Å^{-1} and $k_{hk0} = 0.48788$ Å^{-1}, which result in the lattice constants $c = 8/k_{008} = 11.383$ Å, and $a = (8)^{1/2}/k_{220} = 5.797$ Å. Therefore, this CIS film grown on GaAs substrate is fully relaxed.

To check if there is any residual strain, a 2θ–ω rocking curve was measured at one ϕ position and at ϕ + 180° position. If there is any strain in the film, the distance between the peak for film and that for substrate should change. As shown in Figure 2-31, the distance between two peaks did not change, which substantiates there is no residual strain in the film.

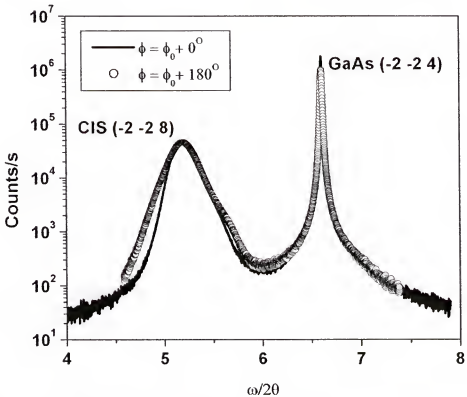

Figure 2-31. ω/2θ rocking curves for (2 2 8) plane of Cu-rich sample W367 and (2 2 4) plane of GaAs at $\phi = \phi_0 + 0°$ and $\phi = \phi_0 + 180°$

2.6 Summary and Conclusions

The evidence presented here suggests that the Cu-Se secondary phase in the Cu-rich CIS films plays an important role in producing epitaxial growth of CIS on a GaAs substrate. A growth sequence for Cu-rich CIS films consistent with the results of this study is next described and is schematically displayed in Figure 2-32. The substrates used in this study were intentionally miscut by 2 ° towards the nearest [011] direction to give an average terrace width of 80 nm.

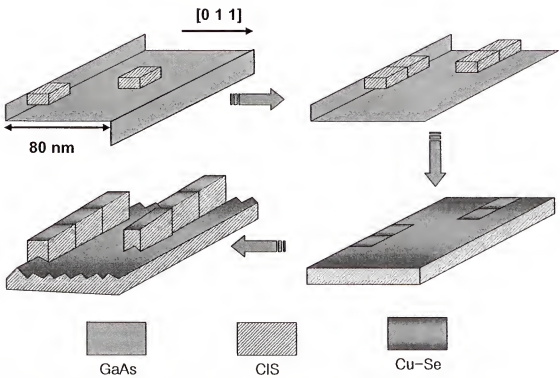

Figure 2-32 Suggested growth mechanism of Cu-rich CIS films (W367, W369)

As seen in Figures 2-2a and 2-3a or 2-5a and 2-6a, the island density for both Cu-rich films are almost identical (Cu/In ratios of 1.02 and 1.09). Furthermore, the island

feature size in sample W369 is nearly the same, while the islands in sample W367 are elongated to different lengths but show nearly the same width. These observations suggest that they nucleated at the same time, and most likely during the initial stages of growth. Given the low-high-low temperature sequence used to initiate growth, it seems reasonable that the islands nucleated during the initial low temperature stage.

Further examination of these SEM photos shows that the islands are textured along the [01-1] direction (i.e., parallel to the terrace steps). The terrace width is considerably smaller than the average spacing between islands (80 vs. ~5000 nm). The elongation along the terrace ledge direction is more pronounced in the sample with the higher Cu/In ratio, and thus presumably the one with the greater adatom surface mobility. It is hypothesized that excess Cu-Se resides on the growing surface to enhance the mobility of adatoms during the growth by acting as a surfactant, and allows the CIS film to grow epitaxially. The elongation could be produced by the enhanced surface mobility allowing nearby ledge sites to compete with the island nuclei to produce a bias for growth along the terrace direction. Another possibility is that nucleation may have been preferred at step or kink sites and more rapidly extended along a terrace edge. In both cases the higher adatom mobility with higher Cu/In ratio gave more elongated growth. It is also noted that the quoted GaAs dislocation density is $<5x10^3/cm^2$, which is much less than the observed island density ($\sim10^6/cm^2$). This fact and their alignment with the terrace edges suggest that nucleation occurred predominantly along the terrace edges.

It is further postulated that the dislocations exist within the nuclei since these nuclei were formed at low temperature. It is noted that the Cu-rich CIS films adopt a two-dimensional layer-by-layer structure for the first ~300 nm (matrix material) and then the

growth changes to a faceted three-dimensional mode at the island locations (Stranski-Krastanov growth mode). The higher local growth of the matrix observed below the island structure could have been produced by the presence of a higher dislocation density in this area. By this high dislocation density, the nucleation sites have lower strain energy and hence lower chemical potential to increase the flux of adatoms to this region.

After a critical film thickness (~ 9 nm) is reached, the excess Cu-Se segregates and precipitates as a solid phase at the initial nucleation sites as well as on the surface. It is noted that the growth temperature (360 °C) is lower than the β-$Cu_{2-x}Se/L_2/L_3$ monotectic temperature but higher than the β-$Cu_{2-x}Se/\gamma$-$CuSe/L_3$ pertitectic temperature, where L_3 is a Se-rich liquid and L_2 is an equimolar Cu-Se liquid. The distance between the island regions appears to be related to the mobility of the adatoms enhanced by Cu-Se secondary phase.

As the island region of Cu-rich CIS films is thought to be the area where dislocations are concentrated, it is also suggested that the translation of chalcopyrite (001) cation planes is more probable in this area and that a small amount of CA-like CIS may coexist with CH-CIS in the island region [Wei92, Sta02]. From the observation of the surface of the matrix region as in Figure 2-20, it is suggested that the strain energy of the matrix region was relieved by the formation of the surface undulation with {112} orientation with the Cu-Se secondary phase on it. Therefore, at the end of the growth, the film becomes a structure with an undulated, layered matrix region on which thick island structures reside with a segregation of Cu-Se secondary phase.

The growth habit for the In-rich CIS film (sample W366) is apparently different at this relatively low growth temperature. In this sample, the bulk Cu-to-In ratio was 0.98.

It is possible there was insufficient Cu to form the Cu-Se surfactant layer or the increase in the surface mobility introduced by the small amount of Cu-Se phase did not induce two-dimensional layer growth. Thus only the domains with larger grain size were observed. Hence, the In-rich CIS film grew as a three-dimensional layer, following a Völmer-Weber (V-W) mode. It is noted that growth of In-rich CIS films of a similar composition at a higher temperature (450 ºC) produced epitaxial films as in Chapter 3, presumably because of the higher surface mobility at the higher temperature. From the strain analysis by XRD space map and a rocking curve measurement, the Cu-rich films are found to be grown epitaxially with no residual strain.

CHAPTER 3
EPITAXIAL GROWTH OF $CuInSe_2$ AT HIGH TEMPERATURE

3.1 Introduction

As described in Chapter 2, it was possible to grow $CuInSe_2$ (CIS) epitaxially at a relatively low temperature (360 °C) for Cu-rich compositions. The explanation is that the excess Cu-Se phase acts as a surfactant to increase the mobility of surface adatoms and thus allow the adatoms to approach the nucleation sites and to grow epitaxially. It has also been suggested that a Cu-Se liquid phase exists and enhances the epitaxial growth of CIS, although no direct evidence has been reported. For the In-rich composition, the CIS film was not grown epitaxially and it showed only the domains with larger grain size. As discussed in Chapter 2, the polycrystalline growth was attributed to insufficient Cu to form the Cu-Se secondary phase, which increases the surface mobility and thus enhances two-dimensional-layer growth. Therefore, it was postulated that at higher growth temperature, the surface mobility, which increases exponentially with temperature, will be sufficient for epitaxial growth of In-rich films without the help of the Cu-Se phase. For these reasons, the growth of CIS films with both Cu-rich and In-rich compositions was performed at a higher growth temperature (464 vs. 360 °C).

Furthermore, the role of Na on the growth of CIS films is not well understood. From the literature review given in Chapter 1, it has been suggested that Na affects the growth process to increase the grain size by acting as a surfactant. Therefore, it is hypothesized that Na will also enhance epitaxial growth of CIS film, even without the help of the Cu-Se secondary phase. Four CIS films were grown on (100) GaAs, Cu-rich

and In-rich, each with and without Na dosing. The growth mode of the films was studied by several techniques including ICP-OES, SEM, XRD, and TEM.

3.2 Experimental Approach

The three-temperature sequence used for the epitaxial growth of CIS at low growth temperature in Chapter 2 was tried using higher initial and final temperatures, and resulted in polycrystalline CIS or poor crystalline quality. This is attributed to a lower density of nucleation sites with higher initial temperature to give a longer migration length of adatoms to reach the nucleation site and achieve epitaxial growth.

The experimental system previously described in Chapter 2 was used to grow four CIS films at the conditions summarized below. A constant growth temperature of 464 °C was used for the growth of CIS films. Because of a limitation in the system design and an increase in the background pressure of the reactor during the growth, this temperature was the maximum achievable one in the system. The background pressure during the deposition process was in the range of 2×10^{-7} to 6×10^{-7} Torr. The direction of the rotation (counter-clockwise) and the rotating speed (12 rpm) were the same as in low temperature growth experiments (Chapter 2). Again, semi-insulating (100) GaAs wafers were used as substrates. The bulk composition of each CIS film was measured by ICP-OES for companion films grown on molybdenum-coated glass substrate by dissolving the film in 15% HNO_3 solution. Two CIS films, one with Cu-rich composition (W558) and the other with In-rich composition (W560) were grown. NaF was used as the Na precursor and delivered to the film from a Knudsen cell. Both Cu-rich (W584) and In-rich (W590) CIS films were dosed with Na with a Na flux impinging on the surface continuously and initiated at the same time as film growth.

3.3 Composition, Phase and Surface Morphology of CIS Films

Table 3-1 summarizes the bulk composition of CIS films. Sample W558 is Cu-rich (Cu/In = 1.10), while sample W560 is slightly In-rich (Cu/In = 0.99).

Table 3-1. Bulk composition of CIS films on Mo-coated glass determined by ICP.

Sample	Cu (at. %)	In (at. %)	Se (at.%) (Δs)	Na (at. %)	Cu/In (Δm)	Growth rate (Å/s)
W558	26.76	24.38	48.87 (-0.022)	-	1.10 (0.098)	0.59
W560	25.30	25.58	49.12 (-0.037)	-	0.99 (-0.011)	0.48
W584	27.06	24.75	47.69 (-0.059)	0.50	1.09 (0.093)	0.52
W590	23.60	26.17	49.24 (-0.036)	0.99	0.90 (-0.098)	0.54

The level of Na dosing lies between 0.5 and 1 %, as stated in Table 3-1. CIGS absorber layers for high efficiency cells typically show 0.1 at.% of Na inclusion [Nil97]. As such a small amount of Na in the films is difficult to detect, secondary ion mass spectroscopy (SIMS) was used to verify the Na level in the film. Depth profiling was also performed to investigate the composition of each element along the depth of CIS film. SIMS analysis was performed using a Perkin-Elmer PHI 6600 SIMS system operating with a 5 keV Cs primary ion beam. The depth profile of the composition of each element is shown in Figure 3-1. In this figure, the depth was calculated from the value of the crater depth after SIMS analysis (1396 nm). The vertical dotted line represents the CIS film/GaAs wafer interface and was estimated by the film thickness of 550 nm as observed in Figure 3-11b by SEM. The element profiles shown in Figure 3-1 indicate considerable diffusion of Cu, In, and Se into the GaAs and the diffusion of Ga from the GaAs into the CIS film. This is, however, believed to be an artifact from uneven sputtering of the rough film surface (AFM image shown in Figure 3-5 with estimated RMS roughness of 3.25

nm). In addition, the raster size was large (400×400 μm). This conclusion is supported from TEM-EDX scan shown in Figure 5-12, which shows that In and Se were not detected in the GaAs substrate (detection limit ~ 0.5%) and Ga is not detected in CIS film though it was not plotted. However, Na was observed to diffuse into the GaAs substrate by TEM-EDX scan. The diffusion of Cu is also supported from the observation of PL peak related to the Cu_{Ga} - Na_i defect states in GaAs as shown in Figure 5-8.

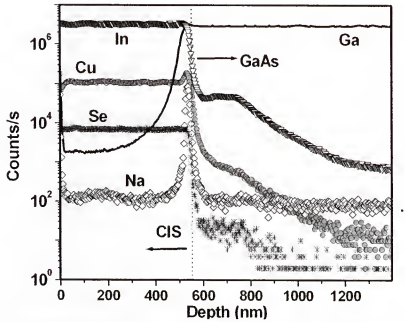

Figure 3-1 Element depth profiles of the In-rich, Na-dosed CIS sample (W590)

To investigate the effect of the Cu/In ratio and inclusion of Na dosing on the crystal quality and growth mode of CIS films at this higher growth temperature, the surface morphologies of the films were investigated by SEM as shown in Figures 3-2 through 3-4. Figure 3-5 is an AFM image as W590 has a very smooth surface that does not show the contrast in a SEM image. The Cu-rich CIS films without (W558, Figure 3-2) and with Na dosing (W584, Figure 3-4) show the island structures embedded in the matrix region

similar to the Cu-rich CIS films grown at low temperature described in Chapter 2. These island structures in Cu-rich CIS films show elongated and faceted structures oriented in [0 1 -1] direction. The density of islands in these two Cu-rich samples is ~ 5×10^5 cm^{-2} for both samples (W558 and W584) and lower than the density of islands in Cu-rich CIS sample (1.1×10^6 cm^{-2}) with Cu/In ratio of 1.09 as in Chapter 2.

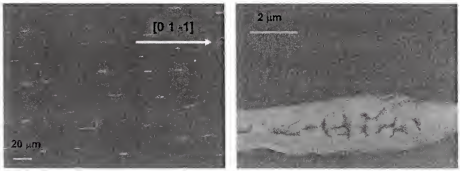

(a) (b)

Figure 3-2 SEM image of the surface of the Cu-rich CIS film (W558, Cu/In = 1.10): (a) 500X, (b) island region at 10,000X

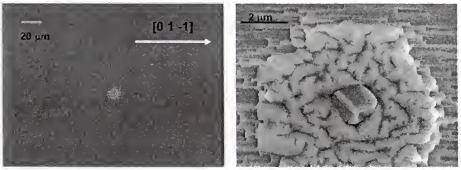

(a) (b)

Figure 3-3 SEM image of the surface of the In-rich CIS film (W560, Cu/In = 0.99): (a) 500X, (b) island region at 10,000X

There are a few grains boundaries observed in the island regions of the Cu-rich CIS film without Na dosing (W558) while the island regions in the Cu-rich CIS film dosed with Na (W584) do not show faceted grain boundaries.

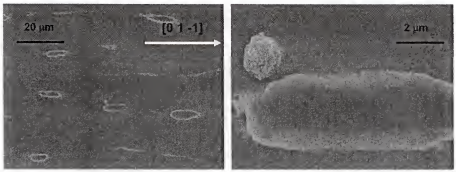

(a) (b)

Figure 3-4 SEM image of the surface of the Cu-rich, Na dosed CIS film (W584, Cu/In = 1.10): (a) 1,000X, (b) island region at 10,000X

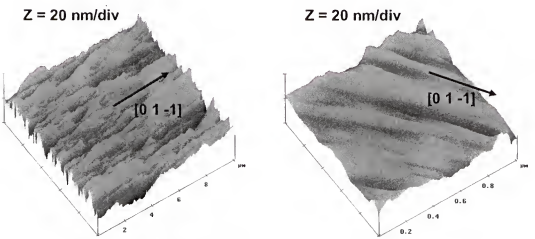

(a) (b)

Figure 3-5. AFM image of the surface of the In-rich CIS film with Na dosing (W590, Cu/In = 0.9): (a) 10 μmx10 μm, (b) 1 μmx1 μm

The matrix regions of both Cu-rich CIS films are textured with the long axis in [0 1 –1] direction of the substrate as was the morphology for the Cu-rich CIS films grown at low temperature (Figure 2-2). The island dimensions, however, are on the order of 3 μmx20 μm and the distance between islands is on the order of 20 to 30 μm. In contrast, typical

dimensions of the island structure for the Cu-rich, epitaxial CIS films grown at lower temperature (see Figures 2-2 and 2-3) was 2x8 μm and the interspacing between island structures was on the order of 10 μm. Therefore, it is obvious that higher growth temperature increased the mobility of adatoms, which resulted in a lower density of nucleated islands to produce more elongated island structures. Also, from the similar island density and the dimensions of the island structure for the Cu-rich CIS samples with and without Na (W558 and W584), it appears that the inclusion of Na did not increase the mobility of adatoms in the growth process.

The increased growth temperature also made it possible to grow nearly island-free epitaxial CIS films with an In-rich composition as shown in Figures 3-3 and 3-5 (W560 without Na-dosing and W590 with Na-dosing). From these images and SAD patterns presented in sections 3.5.2 and 3.5.4, it is concluded that the In-rich CIS films (W560 and W590) grew epitaxially. The epitaxial growth of CIS film with an In-rich composition was not observed at lower growth temperature of 360 °C as reported in Chapter 2. These In-rich CIS films showed an almost island-free matrix structure. The island structure shown in Figure 3-3 was observed with a density of less than 100 cm^{-2} and almost no island structure was observed in the In-rich CIS film with Na-dosing (W590). Therefore, it is suggested that at high growth temperature, the mobility of adatoms is sufficient to allow layer-by-layer growth without the assistance of a Cu-Se secondary phase. It is noted that the density of islands at a given growth temperature increases as the Cu/In ratio increases. This suggests that the excess Cu-Se is important to the island nucleation and growth process.

The faceted island structure of the Cu-rich CIS films (W558, W584) and the island shown in the slightly In-rich CIS film without Na dosing (W560) are likely a mixture of a Cu-Se secondary phase and CIS as was shown for the Cu-rich CIS films grown at low temperature (see sections 2.3 and 2.5). Na dosing appears to increase the extent of the segregation of Cu-Se secondary phase in the island region, which will be confirmed by TEM analysis in section 3.5.3.

The matrix regions of both In-rich CIS films (W560, W590) are also textured in [0 1 -1] direction of the substrate. The roughness of this textured structure in In-rich CIS films at high growth temperature, however, is smaller (less than 5 nm) than that (80 nm) in Cu-rich CIS films grown at lower temperature. In the case of Cu-rich CIS films at lower growth temperature, the formation of an undulated textured surface in the matrix region was attributed to the stress relieving process by forming the (1 1 2) CIS planes with the lowest surface energy. For In-rich CIS films (W560, W590) grown at high temperature, however, formation of a very thin buffer layer at the interface between the film and GaAs is suggested. The existence of this buffer layer was proposed from the observation of a small feature in the XRD spectra shown in Figure 3-12 and the TEM-EDX line scan that shows considerable diffusion of Cu atoms into the GaAs substrate (Figure 3-24). The heteroepitaxial stress in the In-rich CIS films (W560, W590) grown at high temperature is apparently relieved by this compliant thin buffer layer, which results in the shallower undulations on the matrix surface.

3.3.1 EPMA Analysis

The compositions of the matrix and the island regions of each film was probed by EPMA to determine if there is a difference between the two regions, as observed in lower temperature growth. The results of the analysis are summarized in Table 3-2.

Table 3-2 EPMA analysis for the matrix and island regions of CIS film

Sample	Matrix Region				Island Region			
	Cu (at.%)	In (at. %)	Se (at. %)	Cu/In	Cu (at. %)	In (at. %)	Se (at. %)	Cu/Se
W558	26.41	23.67	49.92	1.12	58.31	0.33	41.36	1.41*
W560	25.96	23.78	50.26	1.09	59.25	0.68	40.08	1.48*
W584	26.09	24.11	49.81	1.08	60.60	0.61	38.79	1.56*
W590	26.34	23.48	50.18	1.12	59.25	0.68	40.07	1.48*

*: Cu/Se ratio after subtracting $CuInSe_2$ composition.

In this analysis, the same accelerating voltage (6 keV) was used as for the samples discussed in Chapter 2. Similar to the lower temperature samples, the segregation of Cu-Se into the island region was observed for all CIS films, regardless of their bulk Cu to In metal ratio and Na dosing. It also appears that there was Cu-Se phase segregation near the surface region of the matrix region. EPMA is more surface sensitive (penetration depth of 200 nm at this accelerating voltage), and the Cu to In and Se to In ratios were higher than the bulk average determined by ICP.

To determine whether excess Cu-Se exists as a secondary phase or a solid solution and whether it resides in the matrix or island regions of the CIS films, SEM micrographs were taken after treating each CIS film with a 10% KCN solution to etch any Cu segregates and Cu-Se secondary phases exposed on the film surface. The SEM and AFM micrographs shown in Figures 3-6 to 3-9 are images of the same samples shown in Figures 3-2 to 3-5, but after etching. Note that the images are taken at different magnifications. It is observed that the surface morphology of the matrix region of each sample does not change with etching. The grains in the island regions of the Cu-rich CIS film without Na dosing (W558), however, appear to be covered with a thin layer of a Cu-

Se secondary phase. Comparing Figure 3-6b to 3-2b, it is evident that etching resulted in the exposure of grains in the island region.

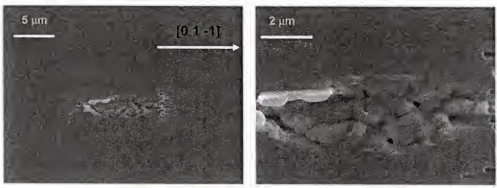

(a) (b)

Figure 3-6. SEM image of the surface of the Cu-rich CIS film (W558, Cu/In = 1.10) after etching: (a) 3,000×, (b) island region at 10,000×

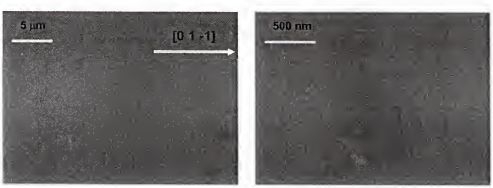

(a) (b)

Figure 3-7. SEM image of the surface of the In-rich CIS film (W560, Cu/In = 0.99) after etching: (a) 3,000X, (b) island region at 30,000X

Interestingly, it is observed that the faceted single grain displayed in Figure 3-4b for the Cu-rich, Na-dosed CIS film (W584), was completely removed by etching (Figure 3-8b). Thus a Cu-Se phase formed a separate grain as the top part of the island structure of the Cu-rich, Na-dosed CIS film (W584).

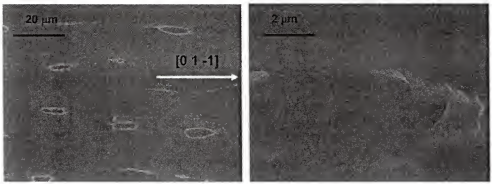

(a) (b)

Figure 3-8. SEM image of the surface of the Cu-rich CIS film with Na dosing (W584, Cu/In = 1.10) after etching: (a) 1,000X, (b) island region at 10,000X

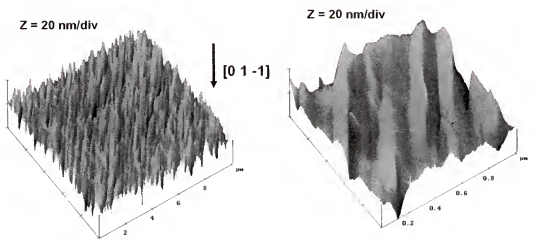

(a) (b)

Figure 3-9. AFM images of the surface of the In-rich CIS film with Na dosing (W590, Cu/In = 0.9) after KCN etching: (a) 10 μmX10 μm, (b) 1 μmX1 μm

For the In-rich CIS film without Na dosing (W560), a large crater was exposed after etching at the location of the island structure. Thus the entire island region consists of a Cu-Se secondary phase in this case. The EPMA analysis for the island region of Cu-rich, Na-dosed CIS film (W584) listed in Table 3-2 suggests that the Cu-Se secondary phase is $Cu_{2-x}Se$ with $x \sim 0.5$, which will be confirmed by TEM analysis (Figure 3-29 in

section 3.5.3). The crystal structure, as determined by TEM analysis, of the Cu-Se secondary phase in the island region will also be reported in section 3.5.3.

From the AFM images of In-rich, Na-dosed sample (W590) after etching, it was observed that the RMS surface roughness was increased to 5.83 nm from the RMS value of 3.25 nm before etching. This result indicates that the surface of the In-rich, Na-dosed sample (W590) was covered with a thin layer of the Cu-Se phase.

3.3.2 Cross-sectional SEM Images

To identify the location of the island and the matrix regions and the possible growth mode for each CIS film, cross-sectional SEM micrographs were taken on samples prepared by cleaving the film/GaAs wafers in the [0 1 -1] direction.

The SEM cross sectional images in Figures 3-10 and 3-11 clearly indicate that CIS films grew uniformly regardless of their Cu/In ratio and the addition of Na at this high growth temperature.

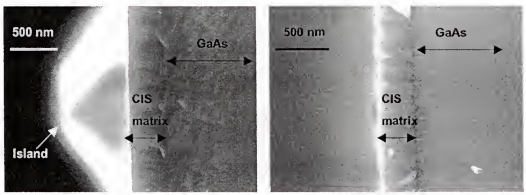

Figure 3-10. SEM cross-sectional images of CIS films without Na-dosing: (a) Cu-rich CIS film (W558, Cu/In = 1.10), (b) In-rich CIS film (W560, Cu/In = 0.99)

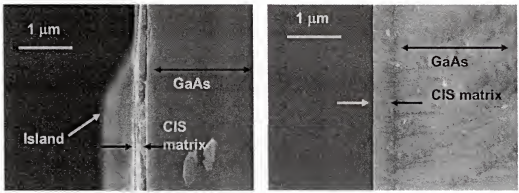

(a) (b)

Figure 3-11. SEM cross-sectional images of CIS films with Na-dosing: (a) Cu-rich CIS film (W584, Cu/In = 1.09), (b) In-rich CIS film (W590, Cu/In = 0.90)

CIS films, however, showed different growth modes depending on the Cu/In ratio. Cu-rich CIS films (W558 and W584) were grown epitaxially by the S-K growth mode, while the nearly stoichiometric or In-rich CIS films (W560 and W590) showed layer-by-layer growth mode. From the fact that the layer-by-layer growth mode was observed for both In-rich samples (W560 and W590), the mobility of adatoms was apparently sufficient for layer-by-layer growth at this growth temperature, and did not require the assistance of the excess Cu-Se or Na-dosing.

3.4 XRD Analysis of CIS Films Grown at High Temperature

3.4.1. XRD θ–2θ Scan and ω-rocking Curve Analysis of CIS Films Grown at High Temperature

To determine the film orientation and phase, high resolution XRD θ–2θ scans were taken for each film with the results summarized in Figure 3-12. The XRD spectra for all CIS films showed XRD peaks for only CIS (00n) planes, which is consistent with the epitaxial growth. There was also a small feature at 2θ values slightly greater than that for the GaAs (400) reflection. To estimate the strain in all CIS films, and to help identify the

origin of this feature, a XRD space map, which is a series of ω–2θ scans with varying ω values, was performed using the X'Pert system. Unfortunately, it was not possible to separate the feature from the intense (400) reflection. The ratio of the intensity of this feature to that of GaAs was very small (~ 8×10^{-4}) and the signal from the unknown peak can be overwhelmed by the background intensity. More importantly, for the crystal plane with higher index usually used in XRD space map, the intensity from the feature is very small when there is a strain distribution which is observed from the broad shape of the peak as in this case. It is due to the less coherence of the crystal planes with high index than (00n) planes when there is a strain in the film.

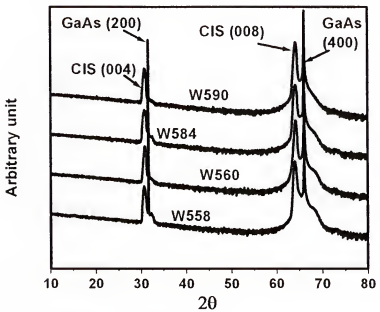

Figure 3-12. XRD θ–2θ scan of each CIS film.

The XRD θ–2θ scan of In-rich CIS film (W560) after etching by KCN solution shows the same feature in the spectrum, which indicates the reflection is not from the Cu-Se secondary phase.

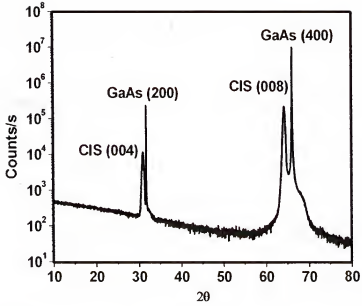

Figure 3-13. XRD 0–2θ scan of the In-rich CIS film without Na-dosing (W560) after KCN etching.

As the bump is located at a higher 2θ value in the [001] direction of the reciprocal space, the phase or region of the film that is responsible for reflection has a smaller c constant than CIS or larger in-plane lattice constant than that of GaAs. Therefore, a possible hypothesis is that a very thin GaAs region is near the interface between the film and the substrate is strained relative to the film. It is also possible that the broad peak is derived from an $In_XGa_{1-X}As$ layer or $CuIn_{1-x}Ga_xSe_2$ layer formed by the inter-diffusion of In or Ga atoms between the film and the substrate. The inter-diffusion of In or Ga will be discussed in section 3.3

To compare the crystal quality of epitaxial CIS films with different Cu/In ratios and Na dosing, ω-rocking curve scans for the (008) plane were recorded for each CIS film. As shown in Figure 3-14, the FWHM values of the rocking curves for the Cu-rich CIS film (W558 or W584) is slightly larger than those for the In-rich CIS films (W560 or

W590). This difference in FWHM values is likely attributed to the defects at the boundaries between the matrix and the island regions in Cu-rich CIS films since these samples have a higher density of islands than the In-rich CIS films (W560 and W590), which are nearly island-free. The FWHM value of the substrate (35 arcsec) is considerably smaller than any of the CIS films (in range of 648 to 923 arcsec). Thus the structural quality of the CIS films is considerably less than the GaAs substrate, regardless of the presence of Na or Cu/In ratio. It is concluded that the mobility of the adatoms is sufficient at this high temperature and the Cu-Se secondary phase is not needed for the epitaxial growth. Similarly, the higher FWHM values for CIS films with Na-dosing (W584, W590) than the CIS films without Na-dosing (W558, W560) also indicate that the inclusion of Na did not improve the crystal quality and the surface mobility. The relatively large difference in lattice constants between GaAs and CIS is likely responsible for the presence of a larger defect density and residual strain that dictate the overall structural quality.

3.4.2 Strain Analysis of CIS Films Grown at High Temperature

An analysis to estimate the change of lattice parameters or the strain of each CIS film was performed in the same manners as described in section 2.6. A space map analysis was performed on the (228) crystal plane of CIS film and the (224) crystal plane of GaAs for each film. The same X'pert system and procedures described in chapter 2 were was used for the space map analysis. A hybrid 4-bounce monochromator with four Ge (220) single crystals and 1/2 inch slit were used to produce the incident beam, and a triple axis, including two of the Ge (220) single crystals, was used to collect the diffracted beam. The combined resolution for this ω–2θ scan is 0.0001°. The values of

the (ω, 2θ) coordinates, were obtained by manually maximizing the intensity of the (228) peak of CIS film and that of the (224) peak of GaAs, respectively.

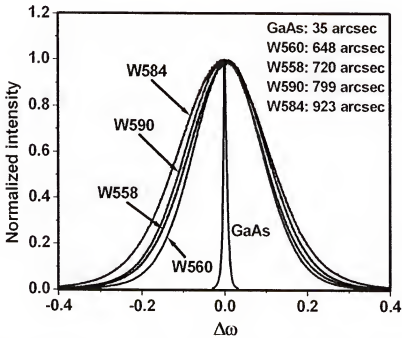

Figure 3-14. ω-rocking curve of the CIS (008) plane for each film and the GaAs (400) plane

In the XRD space map measurement, only the Cu $K\alpha_1$ emission line with a wavelength of 1.54089 Å was used. From this wavelength and the lattice parameter of GaAs (5.654 Å from JCPDS32-0389), the theoretical value for the (ω, 2θ) coordinate set of the GaAs (224) plane is calculated as $\omega = 6.6146°$ and $2\theta = 83.758°$. After considering the offset between the theoretical (6.6146, 83.758) and the measured (6.6466, 83.822) values for the GaAs (224) plane, the values for the CIS (228) crystal plane were calculated as summarized in Table 3-3 by the same method described section 2.6. Also, from the estimated values presented in Table 3-3, the lattice constants of each film were calculated and listed in Table3.4. These values were compared to the unstrained lattice parameters

of CIS film (a = 5.782 Å, c= 11.619 Å from JCPDS40-1487) to give the lattice constants of each film relative to the GaAs substrate using equations 2-7 and 2-8.

Table 3-3 Estimated values of ω, 2θ,φ, and psi for the GaAs (224) and CIS (228) planes

ID	GaAs				CIS			
	2θ	ω	φ	psi	2θ	ω	φ	psi
W558	83.7580	6.6146	-0.18	0.79	81.1875	5.2932	-0.52	0.78
W560	83.7580	6.6146	-0.22	0.96	81.1947	5.3075	-0.48	0.45
W584	83.7580	6.6146	0.81	0.22	81.1977	5.2990	0.81	0.61
W590	83.7580	6.6146	-0.45	0.27	81.2017	5.2475	-0.45	0.56

Table 3-4 Lattice constants and lattice mismatch relative to GaAs for each CIS film

ID	k_{008} ($Å^{-1}$)	k_{720} ($Å^{-1}$)	c(Å)	a(Å)	mismatch
W558	0.6893	0.4880	11.606	5.796	2.51%
W560	0.6894	0.4880	11.604	5.796	2.51%
W584	0.6894	0.4881	11.604	5.791	2.42%
W590	0.6889	0.4888	11.613	5.786	2.33%

A plot of the lattice constants of each CIS film in reciprocal space clearly shows that each CIS film grown at this high temperature was nearly fully relaxed (Figure 3-15). In this case, the lattice mismatch between each CIS film and the GaAs substrate might have been accommodated by misfit dislocations in these films, especially near the boundaries of the island structures embedded in the matrix region for the Cu-rich CIS films (W558, W584) and near the interface between the CIS film and GaAs substrate for the In-rich CIS films (W560, W590). As suggested previously in this section, the XRD spectra shown in Figures 3-12 and 3-13 show a small and broad peak positioned at a slightly greater 2θ value than the reference (400) GaAs reflection. It is proposed that a thin buffer layer was formed in the GaAs near the interface between GaAs and CIS film. This buffer layer is thought to be made from the diffusion of Cu, In or Ga atoms to form a graded

buffer layer near the interface. This buffer layer is assumed to present an in-plane lattice constant close to that of CIS to permit epitaxial growth of a nearly relaxed film.

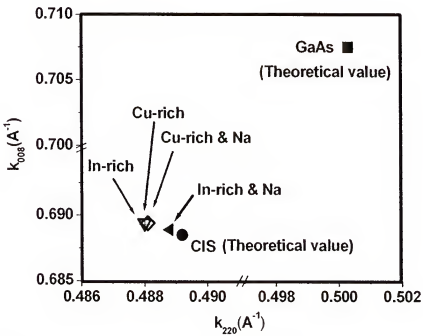

Figure 3-15. Lattice constants of each CIS film in the reciprocal space:

3.5 TEM Analysis of CIS Films Grown at High Temperature

As observed in the SEM micrographs in section 3.3, Cu-rich CIS films (W558, W584) showed the island structures embedded in the smooth matrix region. Also, the top part of the island structure in Cu-rich CIS film with Na-dosing (W584) was suggested as $Cu_{1.5}Se$ from the result by EPMA analysis in section 3.3.1. Therefore, it is necessary to investigate the crystal structure of each CIS film more extensively at high spatial resolution.

For this purpose, TEM analysis was performed in selected areas on each CIS film. Selected area diffraction (SAD) is used to measure the local lattice spacing. For the assignment of each diffraction spot observed using SAD patterns, the distance between

the transmitted beam and each diffraction spot is first measured. Then, the inter-planar spacing for each diffraction spot is calculated by the following equation;

$$Rd_{hkl} = \lambda L, \tag{3-1}$$

,where R, d_{hkl}, λ, and L are the measured distance between the diffraction spot and the transmitted beam, the inter-planar spacing of the corresponding diffraction spot, wavelength of the electron beam, and the camera length of the microscope (82 cm) used to obtain the diffraction pattern, respectively. The wavelength of the electron beam at the accelerating voltage of 200 kV used in this study is 0.0252 Å. The values of d_{hkl}, is then calculated from Equation 3-1 and the corresponding crystal plane (h k l) is determined by comparing the inter-planar spacing value, d_{hkl} with the theoretical or experimental values.

In TEM analysis, dark field images are often taken to yield an image with better contrast and to better demark the dislocations in the film. Practically, a dark field image is obtained by locating the diffracted beam at the optic axis using a two-beam condition, where diffraction is obscured from only two crystal planes. Therefore, the dark field image under this condition shows the feature in the film that has orientation parallel to the diffracted beam, and those features that have an orientation (h k l) normal to the diffracted beam are not shown in the dark field image. This approach can be used to determine the orientation of a dislocation in the material or to identify an area with a different orientation or crystal structure from other areas.

3.5.1 TEM Analysis of the Cu-rich, Na-free CIS Film (W558)

Though the epitaxial growth of all CIS films were confirmed by XRD analysis as in section 3.4, it is necessary to identify the orientation of the CIS film relative to that of GaAs. SAD patterns of film and substrate for the Cu-rich film without Na addition were

taken using selected area aperture with a diameter of 500 nm at [1 -1 0] zone axis as in Figure 3-16.

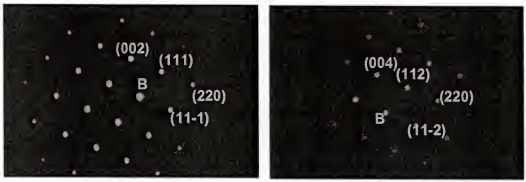

(a) (b)

Figure 3-16. SAD pattern of GaAs substrate and CIS region of Cu-rich CIS film without Na (W558) at zone axis [1 -1 0]: (a) GaAs, (b) CIS

The lattice constants of CIS film were calculated from the pattern shown in Figure 3-16b and a value of 82 cm for the camera length. The value of λL is calculated from the product of the values of the separation distance and the electron beam energy. This is only possible, however, when the sample is positioned exactly at the eucentric position. As in the strain analysis using XRD data, to estimate the offset in the λL value, it is assumed that the in-plane lattice constant of GaAs is the fully relaxed value since it is considerably thick (~ 400 μm) than the overgrown CIS film (~ 0.5 μm). The distance between the transmitted beam (indexed with B in Figure 3-16) and the spot for the (220) plane in the SAD pattern for GaAs area (Figure 3-16a) is 10.7 mm. Therefore, to produce the in-plane lattice constant of GaAs (a = 5.654 Å), the required value of λL is 21.39 mm·Å. For the CIS area, the distance of the (220) spot from the transmitted beam is 10.45 mm, and results in the value of $d_{(220)} = 2.047$ Å (21.39 mm·Å/10.45 mm) and the in-plane

lattice constant, $a = (8)^{1/2} d_{(220)} = 5.790$ Å. The values for the inter-planar spacing, d_{hkl}, and their crystal plane assignments are summarized in Table 3-5.

Table 3-5. Lattice parameters of GaAs and CIS calculated from SAD pattern at [1 -1 0] zone axis for Cu-rich CIS film without Na (W558)

	Distance to the spot (mm)		Inter-planar spacing, d (Å)		Lattice parameter (Å)	
	(220)	(111) or (112)	$d_{(220)}$	$d_{(111)}$ or $d_{(112)}$	a	c
GaAs	10.70	6.56	1.999	3.261	5.654	5.637
CIS	10.45	6.35	2.047	3.369	5.790	11.86

* Estimated 0.1 mm uncertainty.

The assignments to specific crystal planes are labeled in Figure 3-16. From the lattice constants presented in Table 3-5, this CIS film was grown in a nearly relaxed state.

A SAD pattern was also taken at the region near the interface region between CIS and GaAs to check if the Cu-rich CIS film (W558) shows pseudomorphic growth. A selected area (SA) aperture with a diameter of ~ 250 nm was used, where half of the SAD aperture was filled with CIS material and the other half was filled with GaAs material. As the pattern in Figure 3-17 shows, double spots are apparent for each crystal plane, and then the CIS film did not grow pseudomorphically near the interface region.

These results are consistent with the result of the XRD strain analysis presented in the previous section. However, from the observation of the diffused spots in Figure 3-17, it is assumed that the SAD spots in Figure 3-17 might be a mixture of the spots from the bulk region of CIS and GaAs materials and the spots from the buffer layer region since the size of the SAD aperture is too big for a thin buffer layer. Therefore, the growth model is postulated as follows. At the initial stage of the growth, a thin buffer layer with an in-plane lattice close to that of CIS film is formed in the GaAs region near the interface. With the help of this buffer layer and resulting decrease of the heteroepitaxial strain, the CIS film grows epitaxially by 2-D layer growth mode. However, there is also

the segregation of Cu-Se phase from the Cu-rich composition at some of the nucleation sites, which results in the faster growth and thicker island region.

Figure 3-17. SAD pattern at the interface of the Cu-rich CIS film without Na addition (W558) and the GaAs substrate at zone axis [-1 1 0]

The spots labeled as 1 & 1` in Figure 3-17, correspond to the family of (2 2 0) crystal planes, {2 2 0}, and those labeled as 2 & 2`are for the {1 1 1} family.

Dark field image were taken by using (0 0 -4) diffraction vector and the images of the island and matrix regions are presented in Figure 3-18. The images in Figure 3-18 show that the island region consists of an underlying matrix layer and a multiple grain upper region. The image shows the underlying matrix region contains several dislocations originating at the CIS/GaAs interface. The image in Figure 3-18b similarly shows the matrix region contains dislocations. The dislocations extend from the substrate to both in the island and matrix regions. Therefore, it is proposed that the heteroepitaxial strain due to the lattice mismatch between the CIS film and GaAs was largely relieved by the formation of the misfit dislocations during the initial stage of the growth.

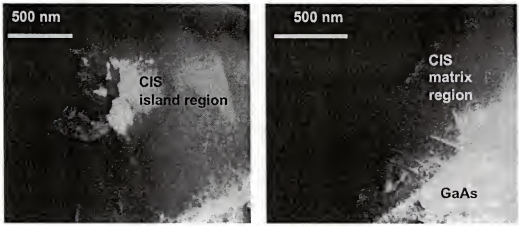

(a) (b)

Figure 3-18 Dark field images of the Cu-rich, no Na sample (W558) using g = (0 0 -4) diffraction vector at 50,000X magnification: (a) island region, (b) matrix region

SAD patterns from a single grain and from multiple grains in the island region were taken (Figure 3-19). These patterns suggest that, as in the case of Cu-rich CIS film grown at lower temperature (See section 2.5 for sample W367), twins are formed, where each grain was grown as a single crystal with a small rotation or mis-orientation relative to each other. The reduction of the heteroepitaxial strain is also attributed to the existence of this twin structure.

(a) (b)

Figure 3-19. SAD pattern for a single grain and multiple grains in the island region at zone axis [1 -1 0]: (a) Single grain, (b) Multiple grains

3.5.2 TEM Analysis of In-rich, Na-free CIS Film (W560)

The same TEM analysis was performed on the In-rich, Na-free CIS film (W560), to determine the values of lattice constants and the relative orientation of CIS region with respect to the substrate. Figure 3-20 shows SAD patterns of CIS and GaAs regions of the sample at zone axis [-1 1 0]. As shown in this figure, the SAD patterns for both GaAs and CIS film show the same symmetry and orientation at the zone axis [-1 1 0] but different distances between corresponding different spots.

The same calibration procedure in section 3.3.1 was performed that requires a (GaAs) = 5.654 Å for the 82 cm camera length. It was calibrated for the (2 2 0) spot and the λL value was determined as 20.65 mm·Å. By using this value, the lattice constants of CIS region and GaAs substrate were again calculated and the values are summarized in Table 3-6. In addition, each diffraction spot was assigned to the specific crystal plane as labeled in Figure 3-20.

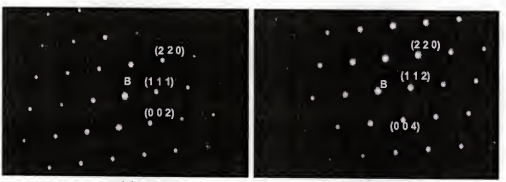

(a) (b)

Figure 3-20. SAD patterns of the GaAs substrate and CIS region for In-rich, Na-free CIS film (W560) at zone axis [-1 1 0]: (a) GaAs, (b) CIS

Table 3-6. Lattice parameters of GaAs and CIS region for In-rich CIS film (W560) calculated from SADP at [-1 1 0] zone axis

	Distance to the spot (mm)		Inter-planar spacing, d (Å)		Lattice parameter (Å)	
	(220)	(002) or (004)	$d_{(220)}$	$d_{(002)}$ or $d_{(004)}$	a	c
GaAs	10.330	7.300	1.999	2.829	5.654	5.658
CIS	10.167	7.250	2.031	2.848	5.745	11.39

* Estimated 0.1 mm uncertainty.

The results shown in Table 3-6 indicate that the in-plane lattice parameter "a" of the In-rich CIS film (W560) is only slightly less than the unstrained material (lattice mismatch = 1.61%). The island-free, In-rich, Na-free CIS film grew heteroepitaxially in a nearly unstrained state with good crystal quality. SAD pattern of the interface region between GaAs and CIS at zone axis [-1 1 0] is shown in Figure 3-21.

Figure 3-21. SADP near the interface between CIS film and GaAs substrate, W560

The diffraction spots were indexed by comparing with the theoretical values and are labeled in Figure 3-21. The diffraction spots labeled 1, 2 and 3 in the figure are produced from the CIS region and 1`, 2` and 3` are from the GaAs region. Their assignments are summarized in Table 3-7.

Table 3-7. Assignment of diffraction spots for the GaAs and CIS regions near the interface.

	1	2	3
GaAs	{1 1 1} family	{0 0 2} family	{2 2 0} family
CIS	{1 1 2} family	{0 0 4} family	{2 2 0} family

* Estimated 0.1 mm uncertainty.

Values of the lattice parameters were calculated from the measured distance between each spot and the transmitted beam (camera length = 137 cm, $\lambda L = 52.77$ mm·Å The lattice constants are summarized in Table 3-8. The in-plane lattice constant, "a", of the CIS near the interface is almost the same as unstrained CIS, which indicates that the film grew in the nearly relaxed state from the interface.

Table 3-8 Lattice parameters of GaAs and CIS near the interface calculated from SAD patterns at [-1 1 0] zone axis

	Distance to the spot(mm)		Inter-planar spacing, d (Å)		Lattice parameter (Å)	
	(220)	(002) or (004)	$d_{(220)}$	$d_{(002)}$ or $d_{(004)}$	a	c
GaAs	26.4	18.70	1.999	2.822	5.654	5.644
CIS	26.0	18.2	2.030	2.899	5.742	11.60

* Estimated 0.1 mm uncertainty.

Figure 3-22 shows a bright field and a dark field image of W560 using (0 0 -4) diffracted beam. Dislocations are observed in the dark field image of the CIS region, some of which extend to the interface between CIS and GaAs, and release the strain energy that would be produced from the lattice mismatch between CIS and GaAs.

The possible inter-diffusion of Cu, In or Ga was proposed in section 3.4 from the observation of the low intensity, broad peak at slightly higher value of 2θ than the GaAs (400) peak (Figure 3-12). To probe this possibility, TEM-EDX scan was performed across the interface. A bright field image of the scan region and TEM-EDX scan are shown as in Figures 3-23 and 3-24, respectively.

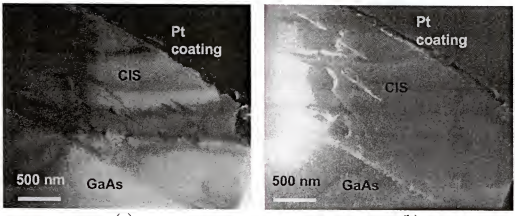

Figure 3–22. Bright field and dark field images of the In-rich, Na-free sample (W560) using g = (0 0 -4): (a) bright field image, (b) dark field image

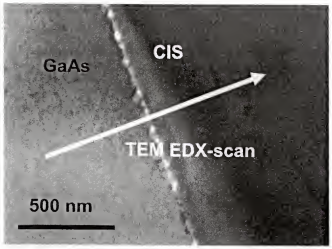

Figure 3-23. Bright field image of the TEM-EDX scan region near the GaAs/CIS interface of In-rich, Na-free sample (W560)

From the EDX scan shown in Figure 3-24, a considerable amount of Cu diffusion from the CIS film into the GaAs was observed. In Figure 3-24, the position of the interface was determined where Se signal sharply decreases to zero. It is known that Cu atom diffuses rapidly in GaAs even at low temperature by an interstitial diffusion process [Fra56]. The diffusion coefficient of Cu in GaAs was reported to be as $D = 3\times10^{-2}\ cm^2s^{-1}\times \exp(-$

0.53/kT) and 7.641×10^{-6} cm^2/s at 464 °C [Hal64]. The solubility was found also to be high ($5.66x10^{14}cm^{-3}$ at 464 °C) [Hal64]. Therefore, it is proposed that the bump on the right side of GaAs (400) peak in the XRD spectra is due to Cu diffusion from CIS film to the GaAs during the growth, and the increase of the in-plane lattice constant is attributed to the formation of Cu_i defects in the GaAs substrate. Additionally, the broad feature was not observed in the XRD spectra of CIS films grown at low temperature (Figure 2-12). However, there was no diffusion of other elements such as Ga or In atoms observed.

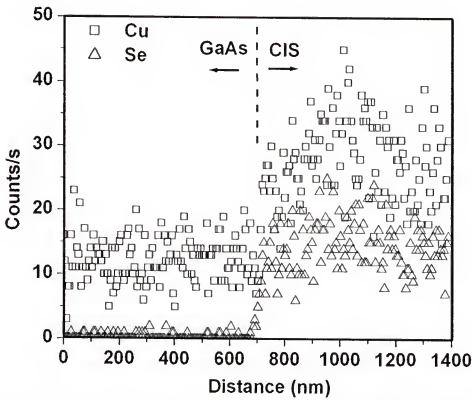

Figure 3-24. TEM-EDX scan of In-rich, Na-free CIS film (W560) near the interface

3.5.3 TEM analysis of the Cu-rich, Na-dosed CIS film (W584)

It is recalled from the results shown in section 3.2 that the top part of the faceted island structure in the Cu-rich, Na-dosed CIS film (W584) was completely removed after KCN etching (Figure 3-8). The conclusion that the upper layer in the island facets are

primarily a Cu-Se secondary phase was further supported by the EPMA results (Table 3-2). The island region of the sample was probed using TEM to independently investigate the upper and lower parts of the island region.

Figure 3-25 shows the bright field images of the island and matrix regions of this CIS film (W584).

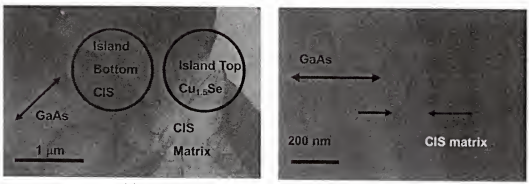

(a) (b)

Figure 3-25. Bright field images of the Cu-rich, Na-dosed CIS film (W584): (a) island structure, (b) matrix region

The EPMA analysis (Table 3-2) suggested that the top part of the island region has composition close to $Cu_{1.5}Se$. Figure 3-26 shows the SAD patterns for both GaAs (a) and the island bottom area (b) that is CIS in the Cu-rich CIS film with Na-dosing (W584).

(a) (b)

Figure 3-26. SAD pattern of GaAs and matrix regions of the In-rich, Na-dosed sample (W584) at [-1 0 3]: (a) GaAs, (b) matrix region

As observed in Figure 3-26, the CIS film was again grown epitaxially with the same orientation as the underlying GaAs substrate. The lattice constants of the CIS film were calculated and summarized in Table 3-9. The results indicate that Cu-rich CIS, Na-dosed CIS film (W584) was again grown nearly relaxed epitaxial, regardless of Na-dosing.

Table 3-9. Lattice parameters of GaAs and CIS calculated from SADP at [-1 0 3] zone axis

	Distance to the spot(mm)		Inter-planar spacing, d (Å)		Lattice parameter (Å)	
	(020)	(311) or (312)	$d_{(020)}$	$d_{(311)}$ or $d_{(312)}$	a	c
GaAs	7.375	12.25	2.827	1.702	5.654	5.556
CIS	7.240	18.20	2.880	1.733	5.760	11.26

* Estimated 0.1 mm uncertainty.

The double spots in the SAD pattern of the interface region are displayed in Figure 3-27., the CIS film appears to have grown in a nearly relaxed state in Figure 3-27. This is the same finding for the film grown without Na-dosing (W558 and W560).

Figure 3-27 .SAD pattern of the interface between GaAs and CIS film at [-1 0 3].

The double spots denoted as D correspond to the spots from both GaAs and CIS film. Figure 3-28 shows the SAD patterns taken for the upper and lower areas in the island

region. The lattice constants of each phase, presumably $Cu_{1.5}Se$ for the upper layer and CIS for the lower layer, were calculated from the spot distances measured on patterns shown in Figure 3-28. From the results shown in Table 3-10, the in-plane lattice constant of the $Cu_{1.5}Se$ phase was strained relative to the CIS phase below it.

(a) (b)

Figure 3-28. SAD pattern of island region of the Cu-rich, Na-dosed sample (W584) at [-1 1 2] zone axis: (a) upper layer of island region ($Cu_{1.5}Se$), (b) lower area of the island region (CIS)

Table 3-10. Lattice parameters of GaAs and CIS calculated from SADP at [-1 0 3] zone axis rL = 20.65

	Distance to the spot (mm)		Inter-planar spacing, d (Å)		Lattice parameter (Å)	
	(220)	(311) or (312)	$d_{(220)}$	$d_{(311)}$ or $d_{(312)}$	a	c
Upper layer ($Cu_{1.5}Se$)	10.10	6.150	2.045	3.358	5.784	5.882
Island bottom (CIS)	10.10	6.225	2.045	3.317	5.784	11.34

* Estimated 0.1 mm uncertainty.

To verify whether the Cu-Se phase in the top part of the island structure is a $Cu_{1.5}Se$ phase, TEM-EDX line scan was performed along the depth direction of the island structure as in Figure 3-29. As shown in Figure 3-29, it is observed that the Cu/Se ratio of the Cu-Se region in the top part of the island structure where there is no In, is close to 1.5.

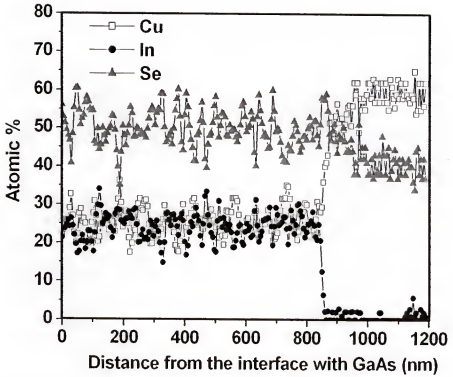

Figure 3-29. TEM-EDX line scans of W584 along the depth of the island structure

The coexistence of $Cu_{1.5}Se$ phase with CIS in the epitaxial growth of Cu-rich CIS (Cu/In = 1.4 ~ 2.6) was reported before by Fons *et al.* [Fon98]. In their work, they reported the existence of the wedge-shaped epitaxial $Cu_{1.5}Se$ phase on the surface of the epitaxial CIS grown on (001) GaAs. They calculated the lattice constant of the $Cu_{1.5}Se$ phase using XRD space map and obtained an in-plane lattice constant of 5.770 Å and an out-of plane lattice constant of 5.722 Å. They also grew epitaxial $Cu_{1.5}Se$ on (001) GaAs substrate without CIS phase and reported the in-plane lattice constant of 5.764 Å as a nearly completely relaxed lattice constant. The in-plane lattice constant calculated here for the $Cu_{1.5}Se$ phase found in the Cu-rich CIS film with Na-dosing (W584) is, therefore, close to the value reported in their study. Also, as in their study, the in-plane lattice constant of $Cu_{1.5}Se$ was strained to that of CIS.

From the fact that the segregation of the epitaxial $Cu_{1.5}Se$ was not observed in the Cu-rich CIS film without Na-dosing (W558) with the same Cu/In ratio in section 3.5.1, it is proposed that Na dosing resulted in the segregation and the epitaxial growth of the $Cu_{1.5}Se$ phase on top of the epitaxial CIS phase in the island structure by acting as a surfactant during the growth. Also, as in the literature review in section 1.1.5.4, Na-dosing was known to improve the crystal quality by suppressing the formation of the defect pairs in the film. Therefore, it is postulated that this suppression of defects in CIS film by Na might suppress the existence of Cu-Se nano-crystalline phase in the CIS region and results in the segregation of the Cu-Se phase in the form of $Cu_{1.5}Se$.

3.5.4 TEM Analysis of In-rich, Na-dosed CIS film (W590)

The final sample examined by TEM in the set was grown at the high temperature of 464 °C with In-rich composition and Na-addition. The SEM images and XRD analysis showed this sample grew island-free and nearly relaxed.

The dark field images shown in Figure 3-30 were taken using the g = (0 2 2) diffracted beam.

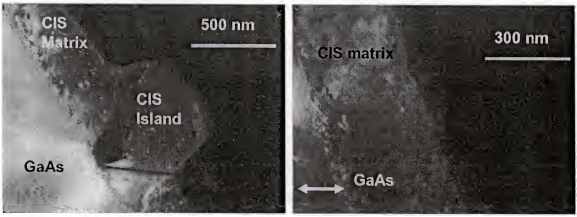

(a) (b)

Figure 3-30. Dark field images of In-rich, Na-dosed CIS film (W590): g = (0 2 2): (a) Dark field image: Island (50,000X), (b) Dark field image: Matrix (100,000X)

There are a few grain boundaries observed in the island region, which may be the result of the formation of twins. Also, the voids and dislocations are observed at the distinctive interface between the matrix region and the GaAs substrate. The dislocations or grain boundaries from the possible twin structures in the island region are believed to release the heteroepitaxial strain in this film. The SAD patterns (Figure 3-31) were taken for the matrix and substrate region and the spots were assigned to crystal planes as in Figure 3-31.

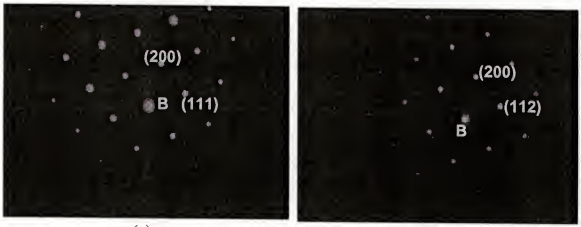

(a) (b)

Figure 3-31 SAD pattern of GaAs and matrix regions of In-rich, Na-dosed CIS film (W590) at [0 1 -1] zone axis: (a) GaAs, (b) matrix region (CIS)

Again, the matrix region of the CIS film showed the same orientation as that of GaAs and the epitaxial growth. The lattice parameters of GaAs and the CIS region were also calculated as in Table 3-11.

Table 3-11. Lattice constants of GaAs and CIS calculated from SADP at [0 1 -1] zone

	Distance to the spot(mm)		Inter-planar spacing, d (Å)		Lattice parameter (Å)	
	(200)	(111) or (112)	$d_{(200)}$	$d_{(111)}$ or $d_{(112)}$	a	c
GaAs	7.48	6.48	2.828	3.264	5.656	5.648
CIS matrix	7.30	6.33	2.897	3.341	5.794	11.54

* Estimated 0.1 mm uncertainty.

The lattice parameter values of the CIS film listed in Table 3-11 show that In-rich, Na-dosed CIS film also grew epitaxially and almost completely relaxed similar to the other CIS films grown at high growth temperature. The double spots in Figure 3-32 indicate that In-rich, Na-dosed CIS film grew epitaxially and with almost no strain.

Figure 3-32. SAD pattern of In-rich, Na-dosed CIS film (W590) at the interface between GaAs and CIS film.

Diffraction spots for twins were observed in the SAD pattern of the island structure (Figure 3-33), and it is suggested that the formation of these twins is induced by the heteroepitaxial stress (lattice mismatch = 2.26%). The formation of twins in the island region leads to the epitaxial growth in this film by relieving the heteroepitaxial stress.

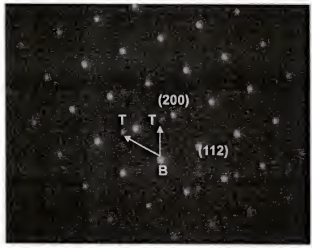

Figure 3-33 SAD pattern of island region above the matrix region of In-rich, Na-dosed CIS film (W590): 'T' means diffraction patterns from twins.

3.6 Summary and Conclusions

The Cu-rich CIS films (W558 and W584) showed morphology similar to those of Cu-rich CIS films grown at the low temperature (Chapter 2). This morphology consists of a 2-D matrix layer with the nucleation of isolated island regions. The thickness of the matrix under the island region is greater than the island-free area. In contrast, a two-dimensional growth mode resulting a very smooth surface was observed for In-rich CIS films (W560 and W590), regardless of Na dosing. This is also in contrast to the polycrystalline structure observed for the In-rich CIS film grown at low temperature. It is suggested that the surface mobility of adatoms was increased for 2-D epitaxial growth at a high growth temperature. The assistance of Cu-Se secondary phase appears not necessary for the epitaxial growth at this high growth temperature.

The In-rich CIS films (W560, W590) showed very few island structure (100 cm^{-2}), while Cu-rich CIS films (W558, W584) showed highly faceted island structures, which increased their size slightly with Na dosing (from 10 ~ 15 μm to 15 ~ 20 μm). However, the spacing between island structures was nearly the same for Cu-rich CIS films regardless of Na-dosing. XRD θ–2θ scans indicated that all CIS films were grown

heteroepitaxially. XRD space maps also indicate that all CIS films grew in a nearly fully relaxed state, which also occurred at the lower growth temperature (Chapter 2).

From the TEM-EDX line scan for the cross-section of In-rich CIS film without Na-dosing (W560), it is observed that there is a considerable Cu-diffusion from the film to the substrate, which is possibly due to the higher growth temperature and possibly attributed to the sequential deposition process of the PMEE reactor allowing longer migration step for the adatoms. It is proposed that this Cu diffusion formed a thin buffer layer with a larger in-plane lattice parameter in the GaAs substrate near the interface region. It is also suggested that the feature of slightly higher value of 2θ than the GaAs (400) peak in the XRD spectra is due to the decrease of c-axis lattice constant (higher 2θ value or lower d_{004}) as well as the increase of in-plane lattice constant in that layer. It is postulated that this buffer layer with increased in-plane lattice constant partly relieved the heteroepitaxial stress between CIS film and the GaAs substrate and enabled CIS films to grow epitaxially without strain along with the strain relieving process by dislocations.

The difference of the growth process between Cu-rich and In-rich CIS films is postulated as follows. As the liquidus of $Cu_{2-x}Se$ was suggested as 525 °C in Fon's *et al.*'s work [Fon98], it is possible that the Cu-Se secondary phase in the Cu-rich CIS films at the higher growth temperature of 464 °C exist as a liquid-like state during the growth. As the surface mobility is enough at this temperature without the assistance of the Cu-Se secondary phase, the adatoms form a 2-D layer from the initial stage of the growth with a buffer layer and resulting smaller lattice mismatch at the interface. For In-rich CIS films, part of the heteroepitaxial strain that is not relieved by the formation of the buffer layer is suggested to be relieved by the formation of dislocations at the interface as the film

continues to grow with the same growth rate for the entire 2-D layer region. However, for Cu-rich CIS films, the Cu-Se phase is segregated at some of sites where the dislocation is concentrated, and then results in the faster growth rate by even lowering the surface energy with a surfactant effect at the sites, and the formation of the thicker island regions over the sites.

The formation of the epitaxial $Cu_{1.5}Se$ phase at the top part of island structure was observed for the Cu-rich CIS film with Na dosing (W584). It is postulated that the Na results in the segregation of the epitaxial $Cu_{1.5}Se$ phase in the top part of the island region by suppressing the formation of the defects, and the existence of the Cu-Se phase as a nano-crystalline phase in the CIS film. This segregation was not observed for the Cu-rich CIS film without Na-dosing (W558) with the same Cu/In ratio.

The SAD patterns taken at the interface of CIS film and GaAs substrate showed double spots for all CIS films. It confirms that all CIS films grew with relaxed state with in-plane lattice constant close to the original value. Twins were also observed in the island region of the Cu-rich CIS film without Na-dosing (W558) and the island region of the In-rich CIS film with Na-dosing (W590) by TEM-SADP. It is proposed that the heteroepitaxial stress due to the lattice mismatch leads to the formation of those twins in the island region. The composition of the Cu-Se phase observed in the island region of Cu-rich CIS film with Na-dosing (W584) was confirmed as $Cu_{1.5}Se$ by TEM-EDX line scan of the island structure. It is also identified as epitaxial to the CIS film in the island structure. The in-plane lattice constant of this $Cu_{1.5}Se$ phase was calculated from the TEM-SADP analysis and its value, 5.784 Å was close to that of CIS (5.784 Å).

CHAPTER 4
EPITAXIAL GROWTH OF CUGASE2 AT HIGH TEMPERATURE

4.1 Introduction

As described in Chapter 2, it was possible to grow Cu-rich CIS films epitaxially at a relatively low growth temperature (360 °C), although In-rich films were polycrystalline. Attempts to grow epitaxial $CuGaSe_2$ (CGS) on GaAs at this low temperature, however, were not successful regardless of the Cu/Ga ratio. All CGS films grown at this low temperature were polycrystalline as evidenced by XRD patterns. The lack of epitaxial growth is attributed to insufficient surface mobility of adatoms on the surface of CGS even under Cu-rich growth conditions. In Chapter 3, it was shown that In-rich CIS films could be grown epitaxially at high growth temperature (464 °C), even without a Cu-Se secondary phase to the increased surface mobility. From the observations for CIS growth, it is postulated that a higher growth temperature will required as well as Cu-rich growth conditions to realize epitaxial growth of CGS films. To test this hypothesis, CGS films were grown under both Cu-rich and Ga-rich compositions at a higher growth temperature (438 °C). It was not possible to increase the growth temperature as high as that used for the growth of CIS films (464 °C) because the background pressure increased inside the reactor during the growth.

Another observation reported in Chapter 3 is that the inclusion of Na during the growth of CIS films resulted in segregation of an epitaxial $Cu_{1.5}Se$ phase as an upper layer on nucleated islands for a Cu-rich CIS film (W584). Therefore, it is further postulated that Na will influence the segregation of a Cu-Se phase in Cu-rich CGS films.

As in the CIS growth study, four CGS films were grown on (100) GaAs, Cu-rich and Ga-rich, each Na-free and with Na dosing. The film composition, morphology, and structural quality were studied by ICP-OES, SEM, XRD, and TEM. These results were used to suggest film growth modes.

4.2 Experimental Approach

Two Na-free CGS films, one Cu-rich (W552) and the other Ga-rich (W567) were grown, along with two Na-dosed CGS films with the similar Cu/Ga ratio as the Na-free samples (W583, Cu-rich and W599, Ga-rich). The direction of the platen rotation (counter-clockwise) and the rotation speed (12 rpm) were the same as in the previous growth experiments (Chapters 2 and 3). The background pressure of the reactor during the deposition process was maintained in the range of 5×10^{-7} to 9×10^{-7} Torr. The same semi-insulating (100) GaAs wafers and surface preparation was used. NaF was again used as the Na precursor and delivered to the surface from a Knudsen cell. Both of the Na-dosed samples (Cu-rich, W583 and Ga-rich, W599) CGS films were dosed with the Na flux impinging on the surface continuously and initiated at the same time as that for the film growth.

The lattice mismatch between CGS and GaAs (-0.71%) is smaller than the case of CIS, and is tensile with a lattice constant "a"of 5.614 Å for CGS compared to 5.654 Å for GaAs.

The bulk composition of each CGS film was measured by ICP-OES on companion films grown on molybdenum-coated glass substrate by dissolving the film in 15% HNO_3 solution. The other characterization tools and their use were the same as previously described in section 2.3.

4.3 Composition, Phase, and Surface Morphology of CGS Films

The bulk compositions of as-grown CGS films as determined by ICP are summarized in Table 4-1. It is noted that the samples are relatively more Cu or Ga rich than the sample set described in the previous chapte rs. The Na levels in the two dosed samples are 0.9 and 2.65%, which also is higher than that measured in the CIS films (Table 3-1 in Chapter 3). It is noted that the growth rate for CGS (~0.3 to 0.4 Å/s) is somewhat lower than used in the growth of CIS (~0.48 to 0.59 Å/s). Although the NaF flux was similar for both sets of film growth, it is reasonable to expect more Na incorporation at the lower growth rate. The difference in Na uptake between the Cu-rich and III-rich samples, however, is contrary to this explanation. Both the CIS and CGS Cu-rich samples showed considerably lower Na uptake than the group III metal-rich samples. As suggested in the literature review in Chapter 1, the most probable site for Na inclusion in the bulk of the CIGS film is VCu. Thus, there should be fewer Cu vacancies available in the films grown under Cu-rich conditions, consistent with the results. Furthermore, as shown in Table 4-1, the Cu/Ga ratio (0.81) of the Ga-rich CGS film with Na-dosing (W599) is smaller than the Cu/In ratio (0.90) of the corresponding In-rich CIS film with Na-dosing. The lower value of the Cu/Ga ratio compared to the Cu/In ratio in the CIS film may also contribute to an increase in the V_{Cu} density.

Secondary ion mass spectroscopy (SIMS) was again employed to estimate the Na level in the film using the same system described in section 3.3. Depth profiling of each element along the depth of CGS film was also performed and the results are shown in Figure 4-1. The depth scale shown in Figure 4-1was calculated from the value of the crater depth after SIMS analysis (1215 nm). The interface between the film and GaAs is estimated to lie approximately at 130 nm from the surface. The thickness of the film,

however, is not uniform as viewed in the cross-sectional SEM image (Figure 4-11b), and the average thickness may be somewhat greater. The profile of each element shown in Figure 4-1 shows a considerable diffusion of Cu, Na, and Se into the GaAs. The diffusion of Se is believed to be an artifact from uneven sputtering of the rough film surface (see SEM image shown Figure 4-5). This conclusion is again partly supported from TEM-EDX scan shown in Figure 5-12 for CIS films grown at a similar temperature, which shows that Se is not detected in the GaAs substrate (detection limit ~ 0.5%). The diffusion of the Cu and Na, however, is supported from the observation of the PL peak related to the Cu_{Ga} - Na_i defect complex in GaAs as shown in Figure 5-8. Since a standard was not available, a quantitative estimate of the levels in GaAs was not possible.

Table 4-1. Bulk composition of CGS films grown on Mo-coated glass determined by ICP

Sample	Cu (at. %)	Ga (at. %)	Se (at. %) (Δs)	Na (at. %)	Cu/Ga(Δm)	Growth rate (Å/s)
W552	27.69	23.33	48.98 (0.003)	-	1.19 (0.187)	0.33
W567	24.65	25.80	49.55 (-0.029)	-	0.96 (-0.045)	0.32
W583	28.03	23.03	48.03 (-0.011)	0.9	1.22 (0.217)	0.33
W599	21.83	26.81	48.71 (-0.047)	2.65	0.81 (-0.186)	0.42

To investigate the effects of the Cu/Ga ratio and Na dosing on the film surface morphology, SEM images were taken as collected in Figures 4-2 through 4-5. The Cu-rich, Na-free CGS film (W552) shows island structures embedded on a smooth matrix bed. The island collection is a mixture of faceted islands (2 ×5 μm) and spherical islands with a typical diameter ~700 nm. The spacing between the islands is in the range 5 to 7

μm. The dimensions and spacing of the faceted island structures, however, are much smaller than those for Cu-rich CIS film described in Chapter 3 (sample W558 dimensions of 3×20 μm and spacing of ~ 20 to 30 μm). Therefore, it appears that the mobility of adatoms on the Cu-rich CGS film is less than that on the Cu-rich CIS film (see Figure 3-2 for comparison), in part due to the slightly lower growth temperature (438 vs. 464 °C).

The Cu-rich CGS film with Na addition (W583) showed morphology similar to that of the Cu-rich, Na-free CGS film (W552). The island structures are more elongated (length ~ 20 μm) in the Cu-rich CGS film with Na-dosing than without, however, the spacing between the islands, and hence nucleation density, is approximately the same (~ 20 μm).

In contrast, the Ga-rich CGS films (W567 and W599) showed spherical island structures of ~1 μm diameter embedded in the smooth matrix region, regardless of Na-dosing. In contrast the In-rich CIS films (W560, Figure 3-3) showed a nearly island-free morphology. This is surprising since the CGS films have a smaller lattice mismatch, grew at a slower rate, and are thinner than their CIS counterparts by at least a factor of 2, all of which should reduce the tendency to nucleate islands. A much reduced surface mobility then seems likely to be responsible for the growth mechanism for the island structure in CGS samples.

The textured structure with the long axis in the [0 1 –1] direction of the substrate was observed in the matrix region for both the Cu-rich and Ga-rich CGS films as was the case for the CIS films. Thus it appears that there was sufficient atom mobility to nucleate and grow at the step edges. These SEM micrographs also hint that the CGS films grew

epitaxially, at least the matrix region, regardless of their Cu/Ga ratio at this growth temperature (438 °C).

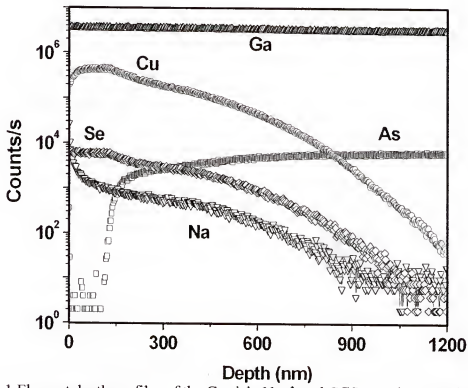

Figure 4-1 Element depth profiles of the Ga-rich, Na-dosed CGS sample (W599)

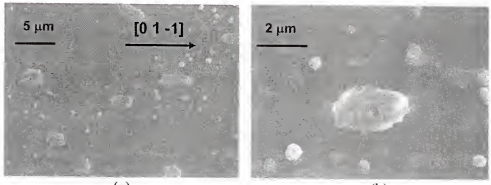

Figure 4-2 SEM images of the surface of the Cu-rich, Na-free CGS film (W552, Cu/Ga = 1.19): (a) 3,000X, (b) island region at 10,000X

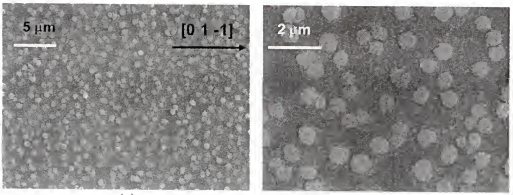

(a) (b)

Figure 4-3 SEM images of the surface of the Ga-rich, Na-free CGS film (W567, Cu/Ga = 0.96): (a) 3,000X, (b) island region at 10,000X

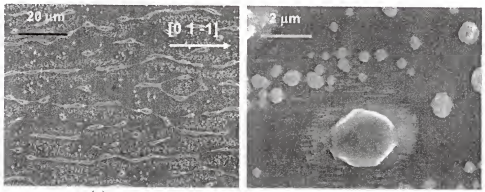

(a) (b)

Figure 4-4 SEM images of the surface of the Cu-rich CGS film with Na-dosing (W583, CuGa=1.22): (a) 1,000X, (b) island region at 10,000X

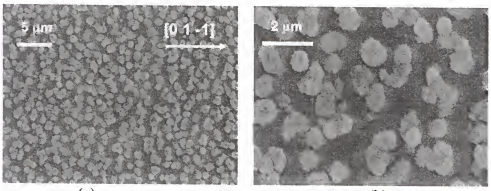

(a) (b)

Figure 4-5 SEM images of the surface of the Ga-rich CGS film with Na-dosing (W599, Cu/Ga = 0.81): (a) 3,000X, (b) island region at 10,000X

4.3.1 EPMA Analysis

The composition of both the matrix and island regions of each CGS film was probed by EPMA and the results are summarized in Table 4-2. Segregation of a Cu-Se secondary phase at the islands was observed for both Cu-rich CGS films (W552 and W583), regardless of Na dosing. The stoichiometry of the Cu-Se secondary phase in the CGS samples is close to $Cu_{1.5}Se$ phase, which was measured in the Cu-rich, Na-dosed CIS film (Table 3-2 in section 3.2.1).

It is interesting to compare the results of the ICP analysis, which summarizes the overall film composition, with those of the EPMA analysis, which represent local area results near the surface (~ 1 μm probe diameter, and ~ 200 nm probe depth). As observed in Tables 4-1 and 4-2, the Cu/Ga ratio of the matrix region determined by EPMA is smaller than that of bulk region by ICP analysis. It indicates that most Cu-Se secondary phase was segregated in the island region for the case of CGS films.

Table 4-2. EPMA analysis of the matrix and the island regions of the CGS films

Sample	Matrix Region				Island Region			
	Cu (at.%)	Ga (at. %)	Se (at. %)	Cu/Ga	Cu (at. %)	Ga (at. %)	Se (at. %)	Cu/Ga
W552: Na-free	25.88	26.20	47.92	0.99	59.75	0.79	39.46	1.56*
W567: Na-free	25.18	24.82	50.00	1.01	25.58	23.05	51.38	1.11
W583: w/ Na	26.45	22.79	50.76	1.16	61.98	0.06	37.96	1.64*
W599: w/ Na	22.88	29.23	47.89	0.78	23.96	26.31	49.73	0.91

*: Cu/Se ratio after subtracting $CuGaSe_2$ composition.

To determine the location of the Cu-Se phase, SEM micrographs were taken after treating each CGS film with a 10% KCN solution to selectively etch possible Cu or Cu-Se secondary phases. The micrographs shown in Figures 4-6 to 4-9 are SEM images of

the same CGS films shown in Figures 4-2 to 4-5 after etching (note that the magnification is different between samples for some images).

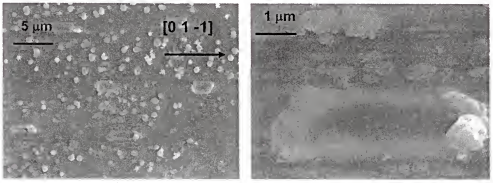

(a) (b)

Figure 4-6 SEM images of the surface of the Cu-rich, Na-free CGS film (W552, Cu/Ga=1.19) after etching: (a) 3,000X, (b) island region at 20,000X

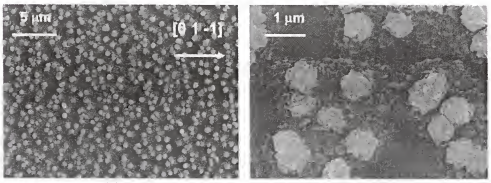

(a) (b)

Figure 4-7 SEM images of the surface of the Ga-rich, Na-free CGS film (W567, Cu/Ga=0.96) after etching: (a) 3,000X, (b) island region at 20,000X

The matrix regions of each sample, regardless of Cu/Ga ratio and the presence of Na during growth, did not significantly change its surface morphology. Also, the appearance of the island regions in the Ga-rich CGS films (W567 and W599) did not show any significant change in surface morphology after etching. The only noticeable change was in the island structures in both Cu-rich CGS films (W552 and W583). The

top layer appears to be etched, which results in a flat surface (W552) or indentation (W583) in the larger islands. This is consistent with a Cu-Se secondary phase present on the upper part of the islands in the Cu-rich samples.

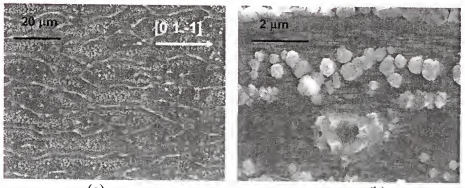

(a) (b)

Figure 4-8 SEM images of the surface of the Cu-rich CGS film with Na-dosing (W583, Cu/Ga=1.22) after etching: (a) 1,000X, (b) island region at 10,000X

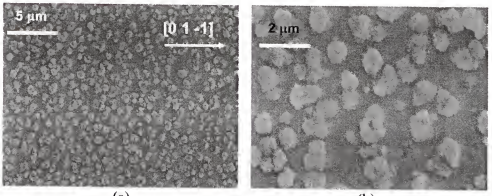

(a) (b)

Figure 4-9 SEM images of the surface of the Ga-rich CGS film with Na-dosing (W599, Cu/Ga = 0.81) after etching: (a) 3,000X, (b) 10,000X

4.3.2 Cross-sectional SEM Images

To locate the island and the matrix regions and to learn more about the possible growth mode for each CGS film, cross-sectional SEM micrographs were taken on samples prepared by the same method described in section 3.3.2. SEM pictures of cross

sections suggest that all CGS films grew with island structures on uniform 2-D layer structure, regardless of their Cu/Ga ratio and Na dosing at this high growth temperature. Also, the epitaxial growth of all CGS films was verified by SAD patterns on TEM samples discussed in section 4.5. The thickness of the matrix region, however, is greater in the Cu-rich CGS films (~ 500 nm) than in the Ga-rich ones (~ 150 nm).

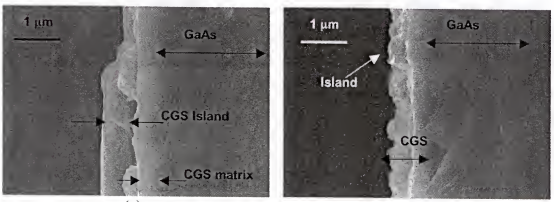

Figure 4-10 Cross-sectional SEM images of Na-free CGS films: (a) Cu-rich CGS film (W552, Cu/Ga = 1.19), (b) Ga-rich CGS film (W567, Cu/Ga = 0.96)

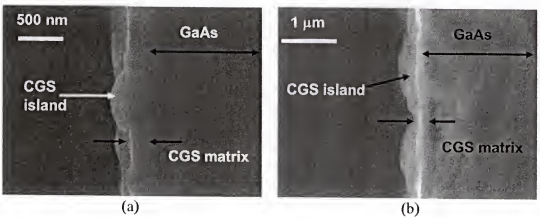

Figure 4-11 Cross-sectional SEM images of CGS films with Na-dosing: (a) Cu-rich CGS film (W583, Cu/Ga = 1.22), (b) Ga-rich CGS film (W599, Cu/Ga = 0.81)

4.4 XRD Analysis of CGS Films

4.4.1 XRD θ–2θ Scan and ω-rocking Curve Analysis

To evaluate the degree of the orientation of the CGS films, XRD θ–2θ scans were performed for each sample to produce the XRD spectra displayed in Figure 4-12. All CGS films showed strong (00n) peaks. Additional peaks from reflections of other CGS crystal planes ((112), (220) and (116)) were observed in the XRD spectra of Ga-rich CGS films (W567 and W599) as seen in Figure 4-12. This result indicates that the Ga-rich CGS films have some polycrystalline regions.

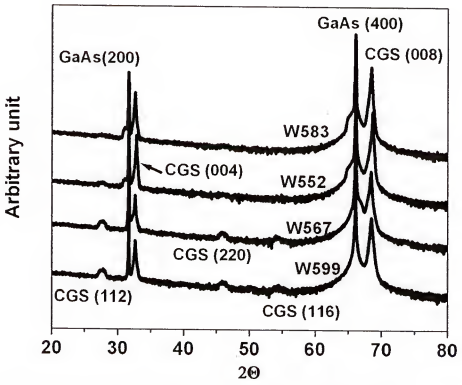

4-12. XRD θ–2θ scans of CGS films (W552, W567, W583 and W599)

A small feature is evident at slightly lower 2θ values than the GaAs (400) peak, which is similar to that seen for the CIS films (Figure 3-12). It is again proposed that this feature originates from the formation of a thin buffer layer in the GaAs substrate as in the case of CIS films (in section 3.4.1). The lower 2θ value for the feature corresponds to a larger c constant or smaller in-plane lattice constant for the buffer layer than that for GaAs, which results in the decrease of lattice mismatch with that of CGS film. The formation of this feature is attributed to Cu diffusion from the CGS film into the GaAs substrate since the feature is not observed in the Ga-rich CGS films (W567, and W599), i.e. the activity of Cu in the excess phase is higher than that in the a-CGS phase and thus more driving force exists. The diffusion of Cu atoms, however, was observed by photoluminescence in all CGS film as discussed in Chapter 5. The diffusion of each element will be further investigated in section 4.5 by TEM-EDX to resolve this issue.

To compare the crystal quality of the four CGS films, ω-rocking curve scans were taken on each CGS film as is summarized in Figure 4-13. The first observation on the values of the measured FWHM values is that they are much closer to the value for the substrate then the values for the CIS samples. The larger lattice mismatch between CIS and GaAs than between CGS and GaAs is likely responsible for the decreased broadening.

The rocking curve scans of the CGS films indicate that the Cu-rich films (W552, W583) grew with better crystal quality (smaller FWHM values) than the Ga-rich CGS films (W567 and W599). This result supports the suggestion that the Cu-Se secondary phase increases the mobility of the adatoms. Also, from the fact that Cu-rich CGS film with Na-dosing (W583) showed the smallest FWHM value (80 arc sec), it is proposed

that Na serves as a surfactant during the growth by further increasing the adatom mobility in the Cu-rich CGS film (W583). Judging surface mobility only by nucleation density, this result is not consistent with the SEM observation in section 4.3 (Figures 4.2 and 4.4), which shows a higher density of island in the Na-dosed sample. The Cu/In ratio for the Na-free sample according to the EMPA results in the matrix region is actually slightly Ga-rich, while Na-dosed sample (W583) is highly Cu-rich. It is also noted in Figure 4.4 that the island areas are of variable size, suggesting that they nuclueated throughout the growth process, perhaps caused by the progressive build-up of excess Cu-Se. The FWHM value is generally considered a better measure of the crystal quality, and thus it is still concluded that Na-dosing gave additional surface mobility to the Cu-rich CGS film (W583).

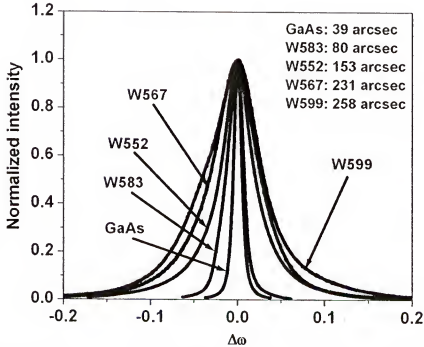

Figure 4-13. ω-rocking curves of the (008) plane of CGS films and (004) plane of GaAs

The Ga-rich CGS film with Na dosing (W599) showed a larger FWHM value than that from Ga-rich, Na-free CGS film (W567). It was observed that the In-rich CIS film showed no epitaxial growth at low growth temperature with insufficient adatom mobility. As it appears that the surface mobility is not sufficient for Ga-rich CGS films from the observation of the SEM micrographs of CGS films, this increase of FWHM for Ga-rich, Na-dosed CGS film is attributed to the smaller Cu/Ga ratio in W599 than that of Ga-rich, Na-free CGS film (W567) as in Table 4-1 (0.96 vs., 0.81) even with Na-dosing.

4.4.2 Strain Analysis of CGS Films

In a manner similar to that described in Chapters 2 and 3, a space map was generated on the (228) crystal plane of each CGS film and the (224) crystal plane of GaAs to quantify the change of lattice parameter or strain in each film. The procedure outlined in section 3.4.2 was used in the analysis. The (ω, 2θ) coordinates of each CGS film and GaAs were obtained manually by maximizing the peak intensity. The same fixture used to record the space map of the CIS films reported Chapter 3 was used to achieve a resolution of 0.0001°. After considering the offset between the theoretical and the measured (ω, 2θ) values of the GaAs (224) plane, the (ω, 2θ) coordinates of the CGS (228) crystal plane for each CGS film were calculated as listed in Table 4-3.

Table 4-3. (ω, 2θ,φ, psi) values for the GaAs (224) and CGS (228) planes

Sample	GaAs				CGS			
	2θ	ω	φ	psi	2θ	ω	φ	psi
W552	83.758	6.6146	0.12	0.03	86.0292	8.5667	-0.23	-0.03
W567	83.758	6.6146	0.23	1.8	86.0448	8.5266	0.15	1.97
W583	83.758	6.6146	0.36	-1.50	85.9602	8.6052	0.24	0.94
W599	83.758	6.6146	0.36	-2.12	86.0764	8.6167	-1.91	0.36

From the values given in Table 4-3, Equations 2-7 and 2-8, along with the lattice parameters of CGS film (a = 5.614 Å, c= 11.022 Å), the lattice constants and the lattice mismatch of each CGS film with respect to GaAs were calculated as summarized in Table 4-4. As the lattice constant "a" of CGS film is smaller than that of GaAs, the mismatch is negative (tensile) while CIS has a positive (compressive) lattice mismatch.

Table 4-4. Lattice constants and lattice mismatch with GaAs for each CGS film

Sample	k_{008} ($Å^{-1}$)	k_{220} ($Å^{-1}$)	c(Å)	a(Å)	mismatch
W552	0.7302	0.5009	10.956	5.647	0.71%-> -0.12%
W567	0.7299	0.5015	10.960	5.640	0.71%-> -0.25%
W583	0.7303	0.4996	10.954	5.661	0.71%-> 0.12%
W599	0.7307	0.5007	10.948	5.649	0.71%-> -0.09%

To compare the results, the lattice constant of each CGS film is plotted in k-space in Figure 4-14. As clearly seen in Figure 4-14, all CGS films were grown almost pseudomorphically with the in-plane lattice constants close to that of GaAs. In other words, the space map result indicates that all CGS films were strained to match the lattice constant of GaAs. Also, it is observed that the in-plane lattice constant of the CGS films approaches the in-plane lattice constant of GaAs with Cu-rich composition or Na dosing, which might be attributed to the increased mobility of adatoms during the growth process along with the creation of the buffer layer with smaller lattice mismatch to the GaAs, resulting improvement in the crystal quality. The decrease in the lattice mismatch between each CGS film with GaAs is in contrast to the mismatch measured between CIS films that were observed to be nearly completely relaxed state as reported in Chapter 2.

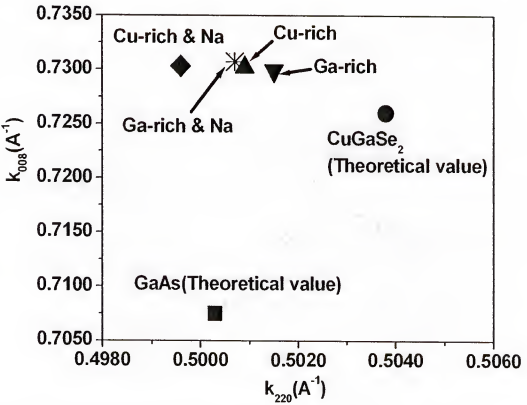

Figure 4-14. Comparison of measured lattice constants of CGS films in k-space to relaxed GaAs and CGS.

4.5 TEM Analysis of CGS Films

The SEM and EPMA results previously described support the conclusion that a Cu-Se secondary phase segregates at the islands. Also, the observation of XRD peaks other than those attributed to (00n) reflections in the Ga-rich CGS films (W567, W599) shown in Figure 4-12 motivates investigation of the local crystal structure and orientation of these films. TEM analysis was performed in the vicinity of both the island and the matrix regions of each CGS film. The same accelerating voltage was used as with the characterization of the CIS films reported in Chapter 3.

4.5.1 TEM Analysis of Cu-rich CGS Film (W552)

Figure 4-15 shows z-contrast dark field images of the island structure and the matrix region of the Cu-rich, Na-free CGS film (W552).

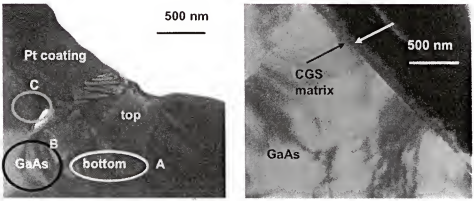

(a) (b)

Figure 4-15. Z-contrast dark field images of the island and matrix regions of Cu-rich, Na-free sample W552: (a) island region, (b) matrix region

(a) (b)

Figure 4-16. SAD patterns of GaAs and the lower part of the island structure for Cu-rich, Na-free CGS film (W552) along the [-1 -1 2] zone axis: (a) GaAs (B), (b) lower island region A (CGS)

Selected area diffraction patterns were taken for GaAs and the bottom part of the island structure shown in Figure 4-15a, respectively to identify the crystal structure and the relative orientation of the CGS film with respect to the GaAs substrate. The patterns

shown in Figure 4-16 show that the lower part of the island structure in CGS film was grown epitaxially with the same orientation as that of GaAs. The lattice constants of GaAs and CGS in this region were also calculated and are given in Table 4-5.

Table 4-5. Lattice parameters of Cu-rich, Na-free CGS film (W552) calculated from SADP along the [-1 -1 2] zone axis

	Distance to the spot(mm)		Inter-planar spacing, d (Å)		Lattice parameter (Å)	
	(220)	(111) or (112)	$d_{(220)}$	$d_{(111)}$ or $d_{(112)}$	a	c
GaAs	10.45	6.40	1.999	3.264	5.654	5.652
CGS	10.50	6.40	1.990	3.264	5.627	11.41

From the lattice constants calculated by SAD patterns, the CGS film in the lower region of the island structure is partially strained to better match the in-plane lattice constant of the underlying GaAs substrate, which leads to a decrease in the lattice mismatch. This is consistent with the XRD space map analysis described in section 4.4.2, although there is a difference in the absolute values. The SAD values are believed to have poor certainty.

It was previously concluded that the upper layer of the faceted island structure observed in Cu-rich CGS films (W552 and W583) was a Cu-Se secondary phase since the material was completely removed after etching with KCN solution (Figures 4-2, 4-4, 4-6, and 4-8). Also, the EMPA measured composition of this top part was consistent with a $CuSe_{1.5}$ phase composition being present. To verify the crystal structure of this upper layer part and determine its relation to the bottom part CGS region, TEM SAD patterns were again taken in this region and at the interface between island upper and lower regions.

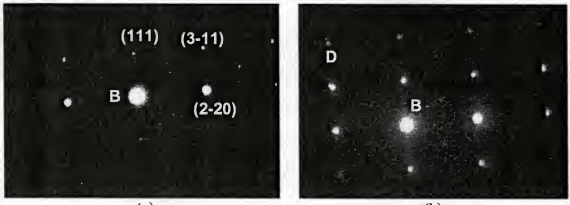

(a) (b)

Figure 4-17. SAD patterns of the island upper region and of the interface between island upper and lower regions along the [-1 -1 2] zone axis for Cu-rich, Na-free CGS film (W552): (a) island upper region: Cu-Se phase, (b) interface between island upper and lower regions

The patterns from these two regions are given Figure 4-17. From the observation of the double spots in SAD patterns taken at the interface between island upper and lower regions (labeled D in this figure), it is concluded that the Cu-Se phase grew unstrained and epitaxially. The lattice constants of the island top region were calculated and are listed in Table 4-6. The results indicate that the lattice constant of the Cu-Se phase are greater from those of the CGS film and the GaAs substrate in Table 4-5.

Table 4-6. Lattice parameters of island top region calculated from SADP at [-1 -1 2] zone axis

	Distance to the spot(mm)		Inter-planar spacing, d (Å)		Lattice parameter (Å)	
	(220)	(111)	$d_{(220)}$	$d_{(111)}$	a	c
GaAs	10.45	6.40	1.999	3.264	5.654	5.652
$Cu_{1.5}Se$	10.25	6.3	2.038	3.316	5.764	5.703

The in-plane lattice constant of the $Cu_{1.5}Se$ phase in Table 4-6 is close to the value measured for the $Cu_{1.5}Se$ phase found in the Cu-rich CIS film with Na-dosing (W584)

given in Table 3-10 (a = 5.784 Å). In both the CIS and CGS films, the $Cu_{1.5}Se$ is strained relative to the chalcopyrite film below it.

To investigate if there is any change in the in-plane lattice parameter of CGS film near the interface between the lower region of the island structure and the GaAs substrate, SAD patterns were taken at these interfaces and the results are shown in Figure 4-18. This figure shows that the CGS grown adjacent to the GaAs substrate both below the matrix only area and the island region were grown with the same orientation as that of GaAs, and their in-plane lattice constants were very close in value. This result is not consistent with the results given in Table 4-5 that show there is a small difference between the in-plane lattice constants of GaAs and CGS. This inconsistency is possibly attributed to the existence of a thin compliant buffer layer formed at the interface.

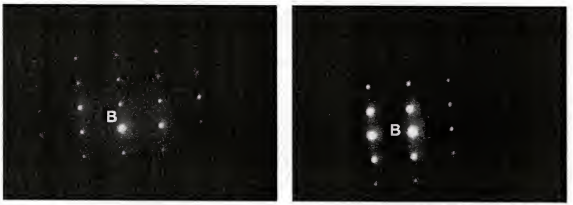

(a) (b)

Figure 4-18. SAD patterns at two interfaces regions of Cu-rich, Na-free CGS film (W552) along the [-1 -1 2] zone axis: (a) SADP at the interface of island bottom and GaAs, (b) SADP at the interface of matrix and GaAs

To explore the composition of the $Cu_{1.5}Se$ phase that resides on the top of the islands, a TEM-EDX scan was taken along the line shown in Figure 4-19. As the Z-

contrast, or equivalently the composition, dark field image shows, the top part of the island region appears to have a different composition from that of lower part of the island. From the TEM-EDX-line scan in Figure 4-20, it is confirmed that the composition of the bottom region of the island structure is close to CuGaSe2 and that of the top part of the island structure is close to $Cu_{1.5}Se$.

In section 4-4 as well as in section 3.4 for CIS films, the existence of a buffer layer at the interface was proposed from the observation of the feature in XRD θ–2θ scans. Also, the formation of this buffer layer was suggested to be related to Cu diffusion into the GaAs substrate. To verify this hypothesis, the diffusion of each element of CGS film and GaAs (Cu, Ga, As, and Se) was studied by taking a TEM-EDX line scan near the interface region between the matrix region and the GaAs substrate of Cu-rich, Na-free CGS film (W552) as shown in Figures 4-21 and 4-22.

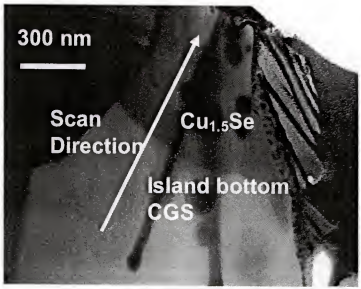

Figure 4-19. Z-contrast dark field image of Cu-rich, Na-free CGS film (W552)

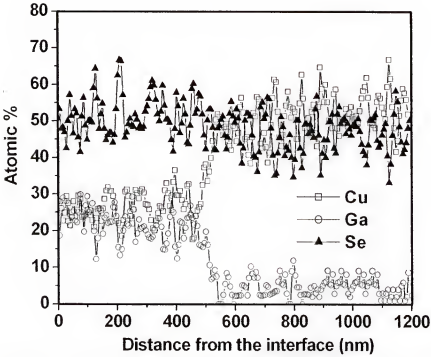

Figure 4-20. TEM-EDX line scan of the island structure of Cu-rich, Na-free CGS film (W552)

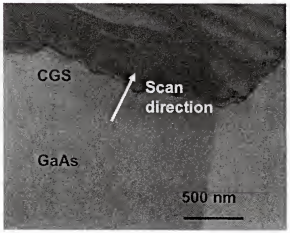

Figure 4-21. TEM-EDX line scan near the interface region of Cu-rich, Na-free CGS film (W552)

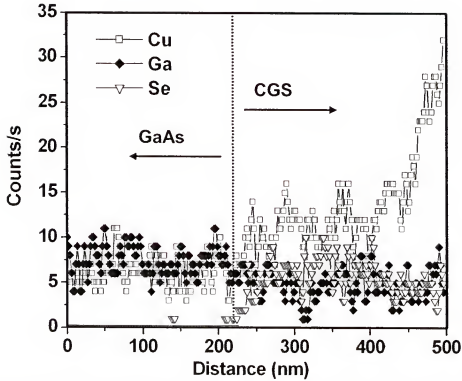

Figure 4-22. TEM-EDX line scan at the interface between CGS film and GaAs for Cu-rich, Na-free CGS film (W552)

From Figure 4-22, it is observed that there is a considerable Cu diffusion from the CGS film into the GaAs substrate. Therefore, it is possible that a graded buffer layer formed in the GaAs region near the interface from this Cu-diffusion. Also, the segregation of the Cu-Se phase on the surface of the matrix region is suggested from the high Cu signal near the surface region. Arsenic was not displayed since no signal was observed in the CGS, and thus it was concluded no diffusion for As occurred.

4.5.2 TEM Analysis of Ga-rich, Na-free CGS Film (W567)

The XRD pattern for the Ga-rich, Na-free CGS film (W567) given in Figure 4-12 show a few peaks in addition to the (0 n) peaks, which indicates that there is a region that is not epitaxial in the film. To investigate the local crystal structure and to locate where the origin of the additional peaks TEM SAD patterns were taken at the island, interface,

and matrix regions as indicated in the dark field image in Figure 4-23obtained from the g = (200) diffracted beam. From the dark field image, the island region is shown to be darker than the matrix region. This indicates that the island region has either a different crystal structure or orientation is different relative to that of the matrix region. Figure 4-24 shows the SAD patterns of GaAs and the matrix region of the Ga-rich, Na-free CGS film (W567) along the [-1 0 3] zone axis. Both SAD patterns verify that the matrix region of W567 was grown epitaxially and has the same orientation as that of GaAs.

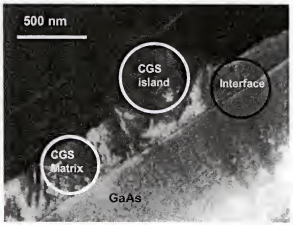

Figure 4-23. Dark field image of the Ga-rich, Na-free CGS film (W567) with g = (200)

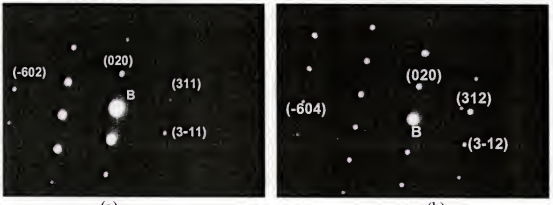

(a) (b)

Figure 4–24. SADP of GaAs and matrix region at zone axis [-1 0 3] for Ga-rich, Na-free CGS film (W567): (a) GaAs, (b) CGS region

Figure 4-25 shows SAD patterns collected for the same regions but along the [1 -1 0] t zone axis. From these SADP's the lattice constants of GaAs and CGS region were calculated as listed in Table 4-7.

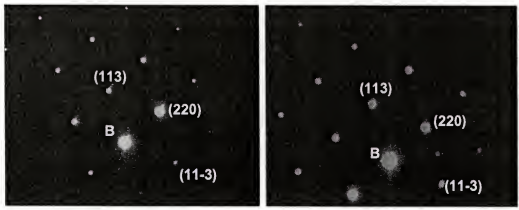

(a) (b)

Figure 4–25. SADP of GaAs and CGS region for Ga-rich, Na-free CGS film (W567) at zone axis [1 -1 0]: (a) GaAs, (b) CGS region

Table 4-7. Lattice parameters calculated from SADP at the [1 -1 0] zone axis shown in Figure 4-24

	Distance to the spot(mm)		Inter-planar spacing, d (Å)		Lattice parameter (Å)	
	(220)	(113) or (116)	$d_{(220)}$	$d_{(113)}$ or $d_{(116)}$	a	c
GaAs	10.60	12.45	1.999	1.702	5.654	5.643
CGS	10.62	12.7	1.995	1.669	5.644	11.02

The results in Table 4-7 indicate that the in-plane lattice constant of Ga-rich CGS film (W567) was strained or expanded to match the lattice constant of GaAs as is the case for the Cu-rich, Na-free CGS film (W552).,

It was previously postulated that the extra peaks in the XRD spectrum of the Ga-rich CGS film (W567) were derived from the spherical island structures. Figure 4-26 shows the SAD patterns of the spherical island structure along the [0 0 -1] and [1 -1 0]

zone axes.., There are two ring patterns shown in the SAD patterns at each zone axis in Figure 4-26. The ring patterns indicate that the grains in the spherical island structure are polycrystalline and verify the observation of the extra peaks by XRD reported in section 4.4. There are also spots in each SAD pattern attributable to twins. These observations indicate that the spherical islands are composed of many grains and each grain has an orientation which is rotated with respect to each other with the rotation plane of {1 1 0}.

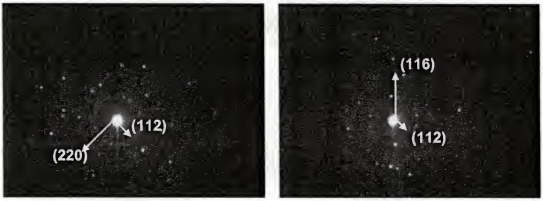

(a) (b)

Figure 4-26. SADP of spherical island structure in Ga-rich, Na-free CGS film (W567): (a) SADP at [0 0 -1], (b) SADP at [1 -1 0]

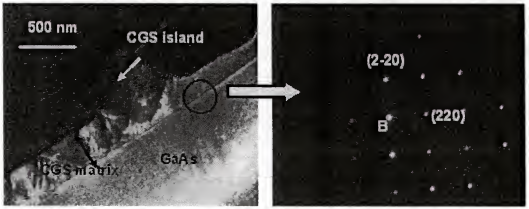

(a) (b)

Figure 4-27 Dark field image and SADP of interface region in Ga-rich, Na-free CGS film (W567): (a) Dark field image by g = (2 0 0), (b) SADP at interface at zone axis [0 0 -1]

From the SADP near the interface region as in Figure 4-27, it is concluded that the CGS film grew nearly pseudomorphically as no double diffraction spots were observed in the SADP. Therefore, it is concluded that the Ga-rich, Na-free CGS film (W567) also grew nearly pseudomorphically.

4.5.3 TEM Analysis of Cu-rich, Na-dosed CGS Film (W583)

The SEM micrographs shown in Figure ? for the,Cu-rich CGS film with Na-dosing (W583) also showed faceted island structures embedded in the matrix region and the upper layer of the island structure was completely removed by KCN etching. From these observation and the EPMA results listed in Table 4-2, the upper layer of the island structure is labeled $Cu_{1.5}Se$ in the dark field image shown in Figure 4-28. Again, the $Cu_{1.5}Se$ region is shown dark in the dark field image as was the case for Cu-rich, Na-free CGS film (W552), which indicates a different orientation or crystal structure from that of matrix region.

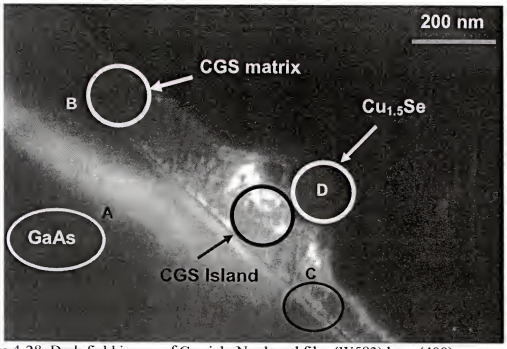

Figure 4-28. Dark field image of Cu-rich, Na-doped film (W583) by g (400)

The chalcopyrite CGS matrix region was grown epitaxially and has the same orientation as GaAs again as revealed by SADP's presented in Figure 4-29. The lattice constants of CGS matrix region were calculated from the diffraction spots in Figure 4-29 and are summarized in Table 4-8.

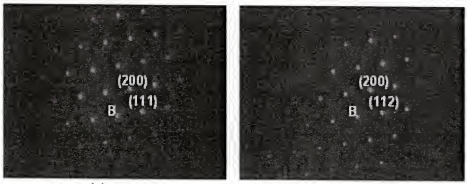

(a) (b)

Figure 4-29. SADP of Cu-rich CGS film with Na-dosing (W583) at [0 1 -1]: (a) GaAs region (A), (b) matrix region (B)

The values indicate that the in-plane lattice constant of the Cu-rich, Na-doped CGS film was also strained to match that of GaAs, and the film is nearly pseudomorphic growth as was the growth of other CGS films.

Table 4-8 Lattice parameters calculated from SADP at [0 1 -1] zone axis

	Distance to the spot(mm)		Inter-planar spacing, d (Å)		Lattice parameter (Å)	
	(200)	(111)	$d_{(200)}$	$d_{(111)}$	a	c
GaAs	7.32	6.3	2.827	3.284	5.654	5.758
CGS	7.33	6.3	2.823	3.284	5.646	11.55

Figure 4-30 shows the SADP at the interface region between matrix region and GaAs, and at the top part of the island structure.

(a) (b)

Figure 4-30 SADP of Cu-rich CGS film with Na-dosing (W583) at [0 1 -1]: (a) at interface between matrix and GaAs (C), (b) at island top region (D, $Cu_{1.5}Se$)

From Figure 4-30a, it is observed that the lattice constants near the interface region between CGS film and the GaAs substrate are close to each other as is the case of all CGS films grown at high temperature. Therefore, it is postulated that a buffer layer might have formed near the interface region leading to the pseudomorphic growth of all CGS films on GaAs. Also, the $Cu_{1.5}Se$ shows the same orientation as that of GaAs as was the case for the Cu-rich CGS, Na-free film (W552).

The lattice constants of $Cu_{1.5}Se$ were also calculated from the diffraction spots in Figure 4-30b and are listed in Table 4-9. The in-plane lattice constant (a = 5.753 Å) is also close to the value (a = 5.764 Å) observed in the Cu-rich CGS film without Na-dosing (W552) and similar to the value (a = 5.784 Å) observed in Cu-rich CIS film with Na-dosing (W584), which is consistent with the formation of the same $Cu_{1.5}Se$ in all three films. It is also noted that the in-plane lattice constant of $Cu_{1.5}Se$ phase is strained to the phase below it.

Table 4-9 Lattice parameters calculated from SAD pattern along the [0 1 -1] zone axis

	Distance to the spot(mm)		Inter-planar spacing, d (Å)		Lattice parameter (Å)	
	(200)	(111)	$d_{(200)}$	$d_{(111)}$	a	c
GaAs	7.32	6.3	2.827	3.284	5.654	5.758
$Cu_{1.5}Se$	7.19	6.24	2.877	3.317	5.753	5.728

Figure 4-31(a) shows a dark field image of the island region on top of the GaAs substrate using the (400) diffracted beam, while Figure 4-31(b) is a SAD pattern taken in the $Cu_{1.5}Se$ island region along the [0 1 -1] zone axis. The interface between the CGS region and the $Cu_{1.5}Se$ region in the island structure is clearly seen in the dark field image, In addition twins are also observed in the $Cu_{1.5}Se$ region. It is possible that the strain from the lattice mismatch between the CGS and $Cu_{1.5}Se$ regions was released by the formation of twins in the $Cu_{1.5}Se$ as well as the misfit dislocations at the interface

As the morphology of the Ga-rich CGS film with Na-dosing (W599), was observed to be almost the same as that of Ga-rich CGS film without Na-dosing (W567) in the SEM micrographs, TEM analysis was not performed on Ga-rich CGS film with Na-dosing (W599).

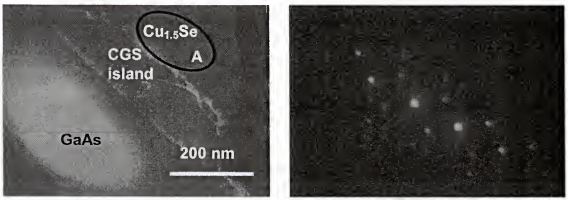

Figure 4-31. TEM image of island region for the Cu-rich CGS film with Na-dosing (W583): (a) Dark field image of the island region: g = (400) (b) SAD pattern of $Cu_{1.5}Se$ region

4.6 Summary and Conclusions

The morphology of the two Cu-rich CGS films (W552 and W583) showed islands with a density of 1.3×10^{6} cm^{-2} embedded in a matrix region similar to that observed in the Cu-rich CIS films (W558, W584) discussed in Chapter 3. The island structures in the Cu-rich CGS film with Na-dosing (W583) are more elongated in the [0 1 -1] direction than Cu-rich, Na-free CGS film (W567).

While the Cu-Se secondary phase formed from the excess Cu in the Cu-rich CIS films resided primarily on the film surface, and the segregation of this $Cu_{1.5}Se$ phase was only observed with Na addition (W584), segregation of epitaxial $Cu_{1.5}Se$ was observed on the top part of faceted island structure, regardless of Na dosing for the case of Cu-rich CGS films (W552 and W583). The Ga-rich CGS films, regardless of Na dosing, contained islands, but of hemispherical geometry with densities of 7×10^{7} cm^{-2} and 1.6×10^{8} cm^{-2} embedded in the epitaxial matrix region. Therefore, it is proposed that the secondary Cu-Se phase in the Cu-rich CGS films, again enhances the surface mobility of adatoms leading to the epitaxial growth with faceted island structures on the 2-D layer matrix region.

XRD θ–2θ scans revealed that all CGS films were grown as a single crystal in the matrix region, but they showed additional peaks for Ga-rich CGS films. From SAD patterns of these regions the hemispherical island structures were observed to consist of multiple grains and are responsible for the additional peaks in the XRD spectra. XRD space map showed that all CGS films grew nearly pseudomorphically and the lowest FWHM value (80 arcsec) for an XRD ω–rocking curve ever reported for CGS was obtained for Cu-rich CGS film with Na dosing (W583). This high quality material shows

that the surface mobility of adatoms was increased by the addition of Na and the presence of excess Cu and Se.

Nearly pseudomorphic growth of all CGS films was confirmed by analysis of TEM –SAD patterns that included the calculation of lattice constants. The Cu-Se secondary phase segregated on top of the island structure for the Cu-rich CGS films (W552 and W583) was identified as $Cu_{1.5}Se$ phase by a TEM-EDX line scan. The in-plane lattice constants of this $Cu_{1.5}Se$ phase in the Cu-rich CGS films were calculated as 5.764 Å (Cu-rich, Na-free CGS film) and 5.753 Å (Cu-rich CGS film with Na-dosing), respectively, by TEM-SADP analysis. This result indicates that the $Cu_{1.5}Se$ phase is strained to the CGS region below it. It is postulated that the segregation of the epitaxial $Cu_{1.5}Se$ phase on top of the island structure of the Cu-rich CGS films was originated from the large lattice mismatch between CGS (5.647 ~ 5.661 Å) and $Cu_{1.5}Se$ (5.764 Å) and resulting strain energy. In contrast, the $Cu_{1.5}Se$ phase in the Cu-rich CIS films has an in-plane lattice constant that is very close to that of CIS (5.784 Å). From the TEM-EDX analysis (Figure 2-19 in section 2.5), it was proposed that the Cu-Se phase in Cu-rich CIS film grown at low temperature might exists as a nano-crystalline phase from the observation of the In concentration near the surface where high Cu and Se concentrations were observed. The reason for the existence of this nano-crystalline Cu-Se phase was explained as the similar lattice constants of the two in section 3.6. A clear interface between the $Cu_{1.5}Se$ phase and the CGS region in the island structure of Cu-rich CGS films (W552 and W583) indicates the formation of misfit dislocations at the interface due to the large lattice mismatch. Twin structures were also observed in the $Cu_{1.5}Se$ phase of the island structure for the Cu-rich CGS films (W552, W583). It is proposed that the twins in the $Cu_{1.5}Se$

phase and the misfit dislocations at the interface relieve the stain between the CGS region and the $Cu_{1.5}Se$ region.

TEM analysis verified that the matrix region of the Ga-rich CGS films (W567 and W599) grew epitaxially and nearly pseudomorphically. The hemispherical island structures that nucleated on the matrix region is composed of multiple grains as well as twins, which are responsible for the additional peaks in XRD θ–2θ scans.

From the results of the SAD patterns at the interface between the CGS region and the GaAs substrate, it was suggested that a very thin buffer layer forms near the interface region to reduce the heteroepitaxial strain between the CGS film and the GaAs, which leads to the nearly pseudomorphic growth. This postulation is also supported by the observation of a small feature in the XRD spectra near the (004) reflection of GaAs. Cu diffusion into the GaAs by TEM-EDX analysis and photoluminescence in Chapter 5 clearly support the interdifusion.

A difference between growths of CGS on GaAs as compared to CIS is that In is present in CIS but not CGS. Thus a large In chemical potential difference exists in the CIS/GaAs couple while the Ga difference is much smaller in the CGS/GaAs couple, and the driving force for In diffusion is greater. It is also noted that the stoichiometry range of GaAs is very much less ($<10^{-5}$ Ga mole fraction) than in CGS or CIS ($\sim10^{-2}$ mole fraction). GaAs is usually grown at near Ga-rich conditions with a corresponding Ga activity close to unity. Thus only a small amount of Ga can diffuse into the CGS before a phase change occurs in the GaAs. The lattice constant of the CGS varies very little with composition and thus changes in the CGS side are not likely responsible for this feature. In contrast for the CIS/GaAs couple, the complete miscibility of Ga and In in the two

compound semiconductors allows for significant inter-diffusion of Ga into CIS and In into GaAs. Comparing the observations of the full set of existence and location of the XRD feature between the CIS and CGS sample, the PL data, and the TEM-EDX results, it is concluded there is a considerable diffusion of Cu into the GaAs in both CIS and CGS films at this high growth temperature. Though the In diffusion was not observed in the TEM-EDX analysis in CIS films, it is probable that there is still an In diffusion into the very thin layer of the GaAs compared to the resolution of the TEM-EDX analysis (5 ~ 10 nm). From the diffusion of these elements, it is postulated that a very thin buffer layer (possibly $In_xGa_{1-x}As$ with Cu atoms for CIS case, and GaAs with Cu_{Ga} for CGS case) is formed near the interface and produces the epitaxial growth by decreasing the heteroepitaxial strain between the film and the GaAs.

CHAPTER 5
STUDY OF DEFECT STRUCTURE OF CGS BY PHOTOLUMINESCENCE SPECTROSCOPY

5.1 Introduction

$CuGaSe_2$ has recently received attention as a material for the top cell in a tandem structure solar cell since it has high band gap (1.73 eV at 10 K). Therefore, its defect structure determines the material's electrical properties as was reviewed in section 1.1.5.2. From the previous studies, it is known that CGS films are always grown p-type since the compensating donor state, Ga_{Cu}, has a much deeper energy level (130 meV) than that of the corresponding donor in CIS (25 meV). The acceptor state, V_{Cu}, in CGS has a similar energy level (50 ~ 60 meV) as that of CIS (40 ~ 50 meV) as summarized in Tables 1-1 through 1-4 in section 1.1.5. Also, shifting to Ga-rich compositions increases the Cu-deficiency and the resulting increase in the V_{Cu}, which is an acceptor. Thus the CGS top cell does not possess a natural buried junction as is thought to exist in CIGS cells. Being able to type convert CGS would be a major contribution. Therefore, it is useful to study its defect structure with varying Cu/Ga ratio and without influence from grain boundaries.

In this study, the defect structure of CGS films was investigated using the same CGS films studied in the previous chapter (Cu-rich and Ga-rich composition). In addition the effect of Na of adding Na during growth was examined to determine its impact on the defect structure of CGS, particularly on the V_{Cu} or Cu_{Ga} defect states. Cu and Ga-rich CGS films with and without Na-dosing were also characterized by photoluminescence

(PL). Films were also analyzed by PL after annealing in Se to investigate the effect of Se concentration on the defect structure as well as the transition related to the V_{Se}.

5.2 Theoretical Background

Photoluminescence (PL) is a process of photon emission by the transition between two defect states in the forbidden gap or between one of the defect states and band edge (conduction band (CB) or valence band (VB)) after the photon energy is absorbed by the material. When light with photon energy higher than the band gap of the material is absorbed, electron-hole pairs are generated in the material. These electron-hole pairs are usually bound as pairs by electrostatic forces, and are called excitons. When these excitons move freely without being bound to a state in the band gap, they are called free excitons. An exciton does not contribute to the current and it can have a different energy level as it is excited and finally breaks into free electron and free hole. The peaks corresponding to these excitonic transitions are usually observed near the band edge in a PL spectrum, the exact position depending on their excitation states. The binding energy of the exciton can be calculated using the following expression for each excitation energy level n [Pan71]

$$E_{ex} = \frac{m_r^* q^4}{2h^2 \varepsilon^2 n^2} \quad , (n=1, 2, 3\ldots), \tag{5-1}$$

where m_r^* is the reduced mass defined as $m_r^* = m_e^* m_h^* / (m_e^* + m_h^*)$ with m_e^* and m_h^* being the electron and hole effective masses, respectively. ε is the dielectric constant, h is Planck's constant, and n is an integer and equal to 1 for the exciton ground state. The binding energy of the exciton can be calculated from literature data for m_e^* and m_h^* or alternatively, it can be calculated by using the following equation if the peak energies for the ground state (E_{FX1}) and the first excited state (E_{FX2}) of the free exciton were known.

$$E_{FX} = \frac{4}{3}(E_{FX1} - E_{FX2}) \tag{5-2}$$

Sometimes, a shoulder is observed at the lower energy side of the excitonic emission peak. If the intensity of this shoulder becomes smaller, the shoulder is usually attributed to the bound exciton emission peak, and can be separated from the excitonic emission peak by measuring the PL emission with varying excitation power. In the excitation power dependent PL spectrum, both peaks show a super linear dependence of PL intensity on the excitation power, which is proof of excitonic recombination [Yam96]. The emission intensity from excitonic recombination is proportional to the product of the number of electrons in CB and holes in the VB. As the photons generate electron-hole pairs, the emission intensity shows a quadratic dependence on the excitation power in principle. The number of bound excitons in thermal equilibrium with the free ones is also proportional to the square of the number of incident photons, or excitation power. As the free excitons are in thermal equilibrium with bound excitons, the temperature dependence of the integrated excitonic emission intensity from both excitons can be represented as follows,

$$N_{FE} = C_1 e^{-E_{a1}/kT} N_{BE}, \; N_{FCP} = C_2' e^{-E_{a2}/kT} N_{FE} = C_2 e^{-(E_{a1}+E_{a2})/kT} N_{BE}, \tag{5-3}$$

where $N_{BE}(T)$, $N_{FE}(T)$, and $N_{FCP}(T)$ are the numbers of bound excitons, free-excitons and free carriers, respectively, k is Boltzman constant, E_{a1} is the localization energy of excitons to a bound center and E_{a2} is the dissociation energy of a free exciton to a free electron-hole pair. As the total number of particles is in equilibrium, the total number of bound and free excitons and carriers is proportional to the excitation power, P_{exc}

$$N_{BE} + N_{FE} + N_{FCP} = CP_{exc}, \tag{5-4}$$

where C is a constant. If the emissions from both bound and free excitons are observed, the integrated PL intensity, I(T), can be represented by the following equation:

$$\frac{I(T)}{CP_{exc}} = \frac{r_1 N_{BE} + r_2 N_{FE}}{N_{BE} + N_{FE} + N_{FCP}}, \tag{5-5}$$

where r_1 and r_2 are the ratios of the collected emission through the aperture to the total emission by bound excitons or free excitons, respectively. Finally, the integrated intensity can be represented as:

$$I(T) = C_0 \frac{1 + rC_1 e^{-E_{a1}/kT}}{1 + C_1 e^{-E_{a1}/kT} + C_2 e^{-(E_{a1}+E_{a2})/kT}} \tag{5-6}$$

with $C_0 = r_1 CP_{exc}$, $C_2 = C_1 \times C_2^{'}$, and $r = r_2/r_1$. Therefore, from parameter fitting of the experimental data, the dissociation energy of a free exciton can be obtained and compared to known values. The localization energy of the bound exciton can also be obtained, from which the activation energy of the bound center, E_{BC} can be calculated by using Hayne's rule [Hay60], $E_{a2} = CE_{BC}$ with $C \sim 0.1$.

There are usually other peaks present in a PL spectrum, which are often related to the donor-acceptor (D-A) pair transition. They usually exist within 200 meV from the band edge for CIS or CGS. The peak energy of this transition is given by the following expression [Beb72].

$$E = E_g - (E_a + E_d) + \frac{e^2}{4\pi\varepsilon_r \varepsilon_0 r} + f(r) \tag{5-7}$$

In this equation, E_g is a band gap, E_a is the acceptor state energy level, E_d is the donor state energy level, ε_r is the dielectric constant of the material, ε_0 is the dielectric constant of the vacuum, r is the separation of the donor-acceptor pair involved in the transition. The last term, f(r) is a quantum mechanical correction, which can be neglected if r is

large compared to the radii of the acceptor and donor states. If the radii of those states overlap, the position of the emission energy increases by quantum mechanical repulsion, which can be calculated from solution of the stationary Schrödinger equation for those states [Sav99]. The D-A related transition shows a peak shift to higher energy (blue shift) with increasing excitation power as the average distance between the D-A pair decreases with excitation power.

The ionization energies of the states involved in a D-A pair transition can be estimated by the temperature dependent PL measurement [Yam96, Yam97] as follows. First, the efficiency of the donor-acceptor recombination for the donor state is represented by

$$\eta_{DA}^{j} = \frac{P_{DA}^{j}}{P_{Dh}^{j} + P_{DA}^{j} + P_{DO}^{j} + P_{TD}^{j}}, \tag{5-8}$$

where each term represents recombination with valence band holes with probability of occurrence P^{j}_{Dh}, the recombination with holes at the acceptor states with probability P^{j}_{DA}, recombination by other processes with probability P^{j}_{DO}, and thermal ionization to the conduction band with probability P^{j}_{TD}, respectively. Also, the efficiency of donor-acceptor recombination for the acceptor state, is given by

$$\eta_{AD}^{j} = \frac{P_{AD}^{j}}{P_{eA}^{j} + P_{AD}^{j} + P_{AO}^{j} + P_{TA}^{j}}, \tag{5-9}$$

with P^{j}_{eA} representing the transition probability with electrons at the conduction band, P^{j}_{AD} the probability of donor-acceptor recombination with electrons at donor state, P^{j}_{AO} the probability of other processes and P^{j}_{TA} the probability of thermal ionization to the valence band edge. The overall efficiency of the donor-acceptor recombination is given by the product of equations (5-8) and (5-9),

$$\eta_{DA}^{j}\eta_{AD}^{j} = \frac{P_{DA}^{j}}{P_{Dh}^{j} + P_{DA}^{j} + P_{DO}^{j} + P_{TD}^{j}} \frac{P_{AD}^{j}}{P_{eA}^{j} + P_{AD}^{j} + P_{AO}^{j} + P_{TA}^{j}} \tag{5-10}$$

The integrated intensity of the emission related to the donor-acceptor recombination is given by,

$$I = \eta_{DA}^{j} A \,, \tag{5-11}$$

where A is a constant. As the thermal transition probabilities P^{j}_{TA} and P^{j}_{TD} are given by an exponential function of ionization energy, they can be represented as,

$$P_{TA}^{j} = B_A \exp(-E_A / kT)\,,\ P_{TD}^{j} = B_D \exp(-E_D / kT)\,, \tag{5-12}$$

where E_A and E_D are the ionization energies of the acceptor and donor states, respectively. As only P^{j}_{TA} and P^{j}_{TD} are functions of temperature and all recombination probabilities are independent of temperature, equation (5-11) can be written as follows:

$$I = \frac{C_3}{[1 + C_4 \exp(-E_D / kT)][1 + C_5 \exp(-E_A / kT)]}\,, \tag{5-13}$$

where all recombination probabilities are shown as constants. Therefore, the ionization energies of the donor and acceptor states can be estimated by parameter fitting of the measured integrated emission intensity of the related peak using equation (5-13).

5.3 Experimental Approach

Samples prepared in the MEE reactor described in section 1.2 were characterized by PL using the facilities at Yungnam University at Kyongsan, Korea. The system is a commercial unit (SPEX750M). The PL measurements were carried out using the 514 nm line of an Ar-ion laser with a beam diameter of ~100 μm and an excitation power of 2 mW. PL spectra were first obtained at 10 K to probe possible excitonic emissions near the band edge as well as any donor-acceptor transitions. The sample temperature was

varied from 10 to 300 K and the temperature-dependent PL intensities measured to allow calculation of the activation energies of defect states involved in a particular transition. In addition to characterizing the defect structure of films grown in the MEE reactor, the effect of subsequent annealing in a Se overpressure was performed to better understand the atomic origin of the defect. These PL measurements were performed on samples annealed by placing a solid Se source in the chamber with the as-grown films at 300 °C for 30 min. PL measurements were not performed for CIS films since a photomultiplier tube was the only available detector and thus suitable for the higher band gap energy films.

The CGS samples studied were grown by MEE. A summary of the growth conditions for each sample is given in Table 4.1. The samples were selected to study the effect of Na-dosing on the point defects in CGS. Two CGS films were grown with Cu-rich (Cu/Ga = 1.19, W552) and Ga-rich (Cu/Ga = 0.96, W567) compositions. For the study of the Na effect on the defect structure, Na was incorporated into each film during growth using a Knudsen cell delivering NaF.

5.4 PL Measurements of Epitaxial CGS Films

5.4.1 PL Spectra

PL measurements were performed on the as-grown CGS films and CGS films after Se annealing at 10 K and the resulting spectra are shown in Figures 5-1 through 5-8. All spectra show a distinctive peak near 1.5 eV (between 1.498 and 1.508 eV). This peak is assigned to the transition of excitons bound to copper centers with trigonal symmetry in Cu-doped GaAs by Wang *et al.* [Wan85] and they suggested that the $Cu_{Ga} - V_{As}$ defect pair is responsible for this center. Therefore, this observation confirms the diffusion of

Cu atoms into the GaAs substrate in all CGS films, and supports the hypothesis proposed in Chapter 4 that a diffusion layer forms within the GaAs substrate.

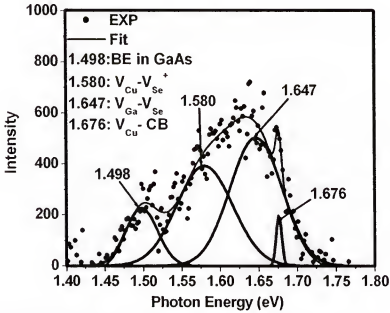

Figure 5-1. PL spectrum of Cu-rich, Na-free CGS film (W552) at 10 K.

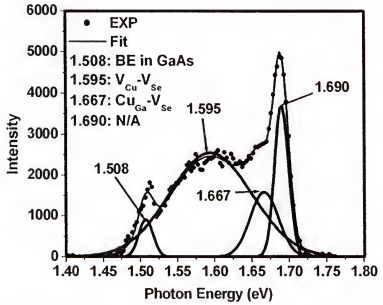

Figure 5-2. PL spectrum of Ga-rich, Na-free CGS film (W567) at 10 K

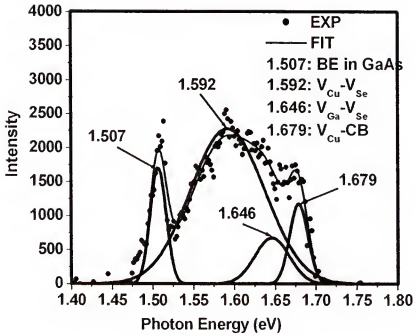

Figure 5-3. PL spectrum of Cu-rich, Na-doped CGS film (W583) at 10 K

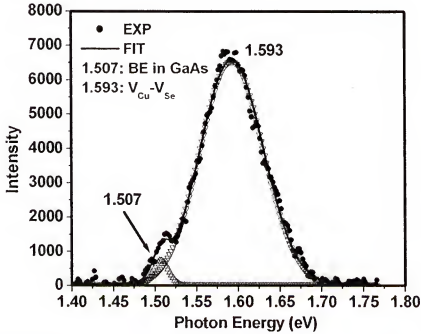

Figure 5-4. PL spectrum of Ga-rich, Na-doped CGS film (W599) at 10 K

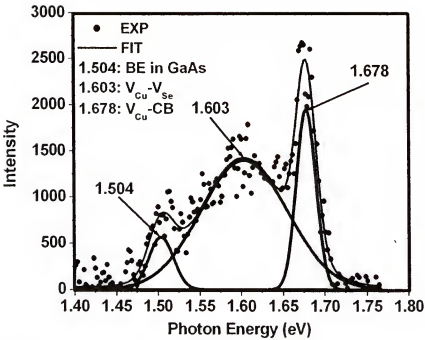

Figure 5-5. PL spectrum at 10 K of Cu-rich, Na-free CGS film (S552) after Se annealing

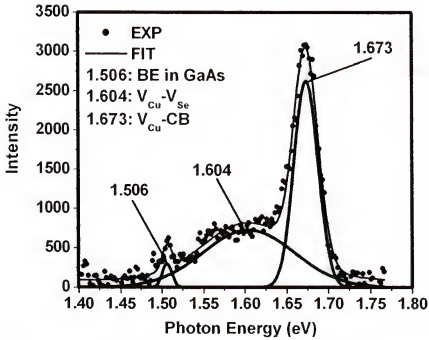

Figure 5-6. PL spectrum at 10 K of Ga-rich, Na-free CGS film (S567) after Se annealing

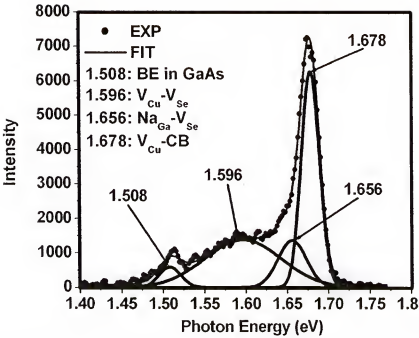

Figure 5-7. PL spectrum at 10 K of Cu-rich, Na-dosed CGS film (S583) after Se annealing

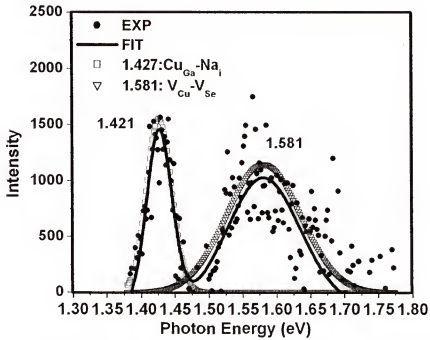

Figure 5-8. PL spectrum at 10 K of Ga-rich, Na-doped CGS (S599) after Se annealing

The peak position in the range 1.673 and 1.679 eV in each PL spectrum, except in the Ga-rich, Na-free CGS film (W567) spectrum, is assigned to the conduction band to acceptor state transition based on previous studies [Chi94, Sch96, Sch99]. From this previous work as well as the peak energy difference (51 ~ 57 meV) from the band edge (1.730 eV at 10 K), the acceptor state involved in this transition is assigned to V_{Cu} acceptor state. It is also observed that the peak at 1.646 or 1.647 eV in the PL spectra of the Cu-rich CGS films (both Na-dosed and Na-free) disappeared after Se annealing (compare Figures 5-1, 5-3, 5-5, and 5-7), which strongly suggests the assignment of this peak to a V_{Se}-related transition.

The peak located at 1.667 eV in the PL spectrum of Ga-rich, Na-free CGS film, W567 (Figure 5-2) also disappeared after Se-annealing. Therefore, it is also assigned to a V_{Se}-related transition. The peak positioned at 1.690 eV in the PL spectrum of the Ga-rich, Na-free CGS film (W567) appears to be related to an excitonic transition. It is not assigned to this specific transition since there is no transition with the corresponding energy difference. For the Ga-rich, Na-dosed CGS film (W599), the PL spectrum (Figure 5-4) included a peak at 1.593 eV, which is assigned to the V_{Cu}-V_{Se} D-A transition as previously suggested in the literature [Sch96, Yam97]. The fact that the ratio of this peak to the peak at 1.676 eV assigned to V_{Cu} – CB transition decreases after Se-annealing for all CGS films, is further evidence that this peak involves a V_{Se} – related transition.

The peak for the V_{Cu}-CB transition (at 1.676 eV) that was found in the Ga-rich Na-free CGS film (W567) and the peak at 1.690 eV were not observed in the Ga-rich, Na-dosed CGS film. The disappearances of the V_{Cu}-CB transition in the Ga-rich, Na-dosed CGS film (W599) is likely due to the decrease of V_{Cu} from the formation of Na_{Cu} with Na

addition. Also, the disappearance of the exciton related peak at 1.690 eV is likely due to the poorer crystalline quality of the Ga-rich, Na-dosed CGS film (sample W599 has the highest FWHM in the HRXRD patterns with the lowest Cu/Ga ratio of 0.81) than that of Ga-rich CGS film. Also, a new peak appears at energy of 1.421 eV in the PL spectrum when Na is added to the Ga-rich CGS film (Figure 5-8). Gislason *et al.* proposed that the PL peak at 1.41 eV observed in GaAs doped with Cu and Li atoms is related to the Cu_{Ga}-Li_i-related transition [Gis85].

Figure 5-10 is a TEM-EDX line scan of the Cu-rich, Na-dosed CGS film (W583) without Se-annealing for the region shown in the micrograph in Figure 5-9. Considerable diffusion of Na into the GaAs substrate is evident in the profile shown in Figure 5-10. These profiles are consistent with the assignment of observed peak intensities to Na and Cu related defect in GaAs. It is also noted that considerable diffusion of Na and Cu into the substrate occurs when CGS is replaced by CIS for an In-rich composition and of course Na-dosing (Figures 5-11 and 5-12).

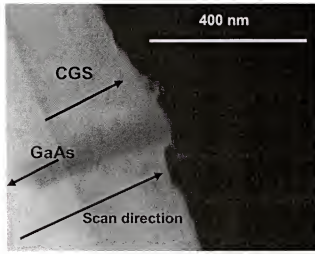

Figure 5-9. TEM-EDX line scan region of the Cu-rich, Na-dosed CGS film (W583)

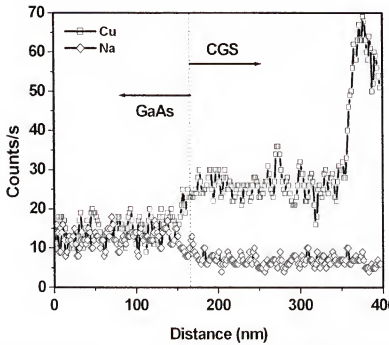

Figure 5-10. TEM-EDX line scan of Cu-rich, Na-doped CGS film (W583) before Se annealing

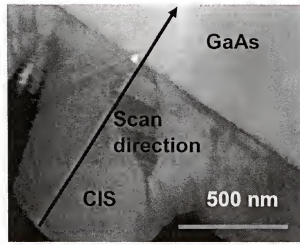

Figure 5-11. TEM-EDX line scan region of In-rich, Na-dosed CIS film (W590)

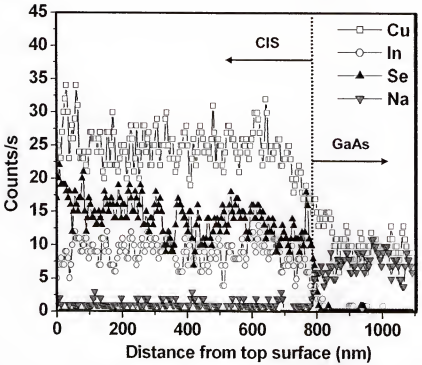

Figure 5-12. TEM-EDX line scan of In-rich, Na dosed CIS film (W590) before Se annealing

Therefore, it is suggested that this peak at 1.41 eV is related to a Cu_{Ga}-Na_i-related transition in GaAs, which forms upon both Cu and Na diffusion during growth into the GaAs substrate from the film.

There is a new peak observed at 1.656 eV in the PL spectrum of the Cu-rich, Na-dosed CGS film after Se-annealing (S583) as indicated in Figure 5-7. This peak is believed to be related to the transition involving a Na-related defect. Assuming that V_{cu} is present in the material, even for Cu-rich conditions, the search for a transition of a defect state pair with a relatively small formation energy and defect level would include V_{Ga}-V_{Se}: 1.646 eV, V_{Cu}-CB: 1.678 eV, V_{Cu}-V_{Se}: 1.6 eV, Cu(Ga)–V_{Se}: 1.667 eV. Since these defect pairs are accounted for, a Na-related defect is the likely possibility for this peak

5.4.2 Thermal Quenching of PL Peaks

To investigate the PL peaks involving only donor-acceptor transitions, a selected transition was thermally quenched to probe the activation energy of the defect state of the shallower energy level according to the following equation [Dea67, Yam99]:

$$I = \frac{C_1}{(1 + C_2 \exp(-E/k_B T))} \tag{5-15}$$

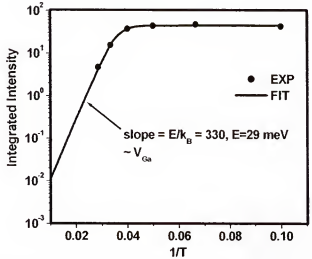

Figure 5-13. Thermal quenching of PL peak at 1.647 eV in the Cu-rich, Na-free CGS film (W552)

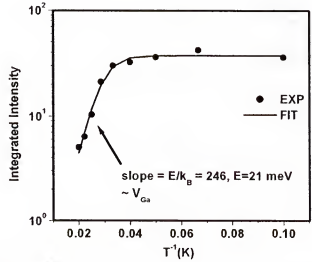

Figure 5-14. Thermal quenching of PL peak at 1.646 eV from Cu-rich, Na-dosed CGS film (W583)

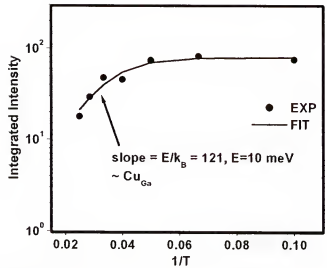

Figure 5-15. Thermal quenching of PL peak at 1.667 eV from Ga-rich, Na-free CGS film (W567)

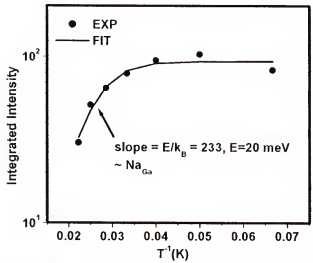

Figure 5-16. Thermal quenching of PL peak at 1.656 eV from Cu-rich, Na-dosed CGS film after Se annealing (S583)

In equation (5-15), I is the integrated intensity, C_1 and C_2 are constants, k_B is the Boltzman constant, and E is the activation energy of the shallower defect state of the two.

The results of the thermal quenching studies are graphically shown in Figures 5-13 to 5-16. Several conclusions can be drawn from these results. First, analysis of the thermal quenching data for the peak at 1.647 eV found in the Cu-rich, Na-free CGS films (W552, W583) shown in Figures 5-13 and 5-14 produces slopes of (29±2.1) and (21±1.4) meV, respectively. These energy levels are likely related to the V_{Ga} defect state, since they are close to the value (20 meV) reported in a previous study [Sch00b]. Therefore, the peak at 1.647 eV is assigned to the V_{Ga}-V_{Se} transition.

Activation energy of (10±0.34) meV was derived from the thermal quenching data of the PL peak at 1.667 eV (see Figure 5-15). From the fact that this peak disappeared after Se annealing and the value of the activation energy (10 meV) reported for the Cu_{Ga} defect by Bauknecht *et al.* [Bau00], this transition is assigned to the Cu_{Ga}-V_{Se} transition.

The spectrum shown in Figure 5-7 reveals a new peak at 1.656 eV for the Cu-rich, Na-dosed CGS film after Se-annealing (S583) The activation energy of this transition was calculated as (20±0.78) meV (Figure 5-14), and it was tentatively assigned to the Na_{Ga} acceptor state. It is also suggested that this peak is related to the Na_{Ga}–V_{Se} transition, and this conclusion is based on the following rationale. First, the activation energies estimated for the V_{Ga} defect from the data shown Figures 5-13 and 5-14, are 29 and 21 meV. In addition, the reported activation energy of the defect level of V_{Se} is 80 meV [Sch96]. From these energy levels, the Coulombic term in equation (1-7) for the peak at 1.647 eV is estimated as 18 and 26 meV, respectively. This value shows good agreement with Coulombic energy of 26 meV in the report of Bauknecht *et al.* [Bau00] with an estimated typical distance between the two charged defects of 4 nm. Using these values to approximate the Coulombic energy of the defect complex responsible for the peak at

1.656 eV, the donor state involved in this transition is suggested to be a V_{Se} since the activation energy for the donor state is calculated as 72 ~ 80 meV. The peak energies observed for each sample in this study and their assignments are summarized in Tables 5-1 and 5-2.

Table 5-1 Peak energies and their assignments observed in CGS films in this study.

Peak Energy (eV)	Cu-rich	Ga-rich	Cu-rich, Na-dosed	Ga-rich, Na-dosed
1.427				
1.500	$Cu_{Ga} - V_{As}$	$Cu_{Ga} - V_{As}$	$Cu_{Ga} - V_{As}$	$Cu_{Ga} - V_{As}$
1.580	$V_{Cu} - V_{Se}$			
1.600		$V_{Cu} - V_{Se}$	$V_{Cu} - V_{Se}$	$V_{Cu} - V_{Se}$
1.647	$V_{Ga} - V_{Se}$		$V_{Ga} - V_{Se}$	
1.656				
1.667		$Cu_{Ga} - V_{Se}$		
1.676	$V_{Cu} - CB$		$V_{Cu} - CB$	

Table 5-2 Peak energies and their assignments observed in CGS films after Se annealing in this study.

Peak Energy (eV)	Cu-rich	Ga-rich	Cu-rich, Na-dosed	Ga-rich, Na-dosed
1.427				$Cu_{Ga} - Na_i$
1.500	$Cu_{Ga} - V_{As}$	$Cu_{Ga} - V_{As}$	$Cu_{Ga} - V_{As}$	
1.580				$V_{Cu} - V_{Se}^{+}$
1.600	$V_{Cu} - V_{Se}$	$V_{Cu} - V_{Se}$	$V_{Cu} - V_{Se}$	
1.647				
1.656			$Na_{Ga} - V_{Se}$	
1.667				
1.676	$V_{Cu} - CB$	$V_{Cu} - CB$	$V_{Cu} - CB$	

5.5 Summary and Conclusions

The point defects of CGS films grown by MEE on GaAs were characterized by low temperature PL spectroscopy. In particular, the effects of the Cu/Ga ratio, Na dosing, and subsequent Se-annealing on the defect states were investigated. Peak assignments to specific defects were suggested by comparing the spectra to previously reported results, observing changes in the spectra as the film composition was changed, and estimating activation energies estimated from the results of thermal quenching experiments. This

work supports the findings of previous studies of the defects V_{Cu}, V_{Ga}, Cu_{Ga}, and V_{Se} with corresponding activation energies of 50 ~ 60, 20 ~ 30, 10, and 75 ~ 80 meV. In addition, a new defect state was observed at 20 meV above the valence band edge from the thermal quenching of the peak at 1.656 eV in the Cu-rich, Na-dosed CGS film after Se annealing. For the Ga-rich, Na-dosed CGS film, a new PL peak was observed at 1.427 eV in the PL spectrum after Se annealing and assigned to the transition from the exciton bound to the $Cu_{Ga} - Na_i$ defect pair.

Composition profiles across the CGS/GaAs interface (TEM_EDX) showed substantial diffusion of Cu into the GaAs as well as Na when added to the film. A peak near 1.5 eV was observed in all CGS films. Consistent with previous studies on GaAs, this peak was assigned to the transition from the excitons bound to the $Cu_{Ga} - V_{As}$ defect pair, consistent with diffusion of Cu into the GaAs substrate in all CGS films. The diffusion of Na and Cu into the GaAs substrate was observed by TEM-EDX line scan of In-rich, Na-dosed CIS film (W590). From this observation and the report of the Cu_{Ga}-Li_i-related transition peak in the GaAs doped with Na and Cu, it is proposed that the peak at 1.421 eV observed in the PL spectrum of Ga-rich, Na-dosed CGS film after Se annealing (S599) is related to the Cu_{Ga}-Na_i-related transition.

A peak at 1.67 eV was assigned to the V_{Cu}-CB transition by comparison of the energy difference from the band edge with the values reported in the previous studies. Activation energy in the range 21 to 29 meV was estimated for the peak at 1.647 eV from the thermal quenching experiments, and it was assigned to the activation energy of the V_{Ga} defect, again from comparison with the value in previous studies. From the

disappearance of the peak at 1.647 eV after Se-annealing, this peak was assigned to the V_{Ga}-V_{Se} transition.

An activation energy of 10 meV was calculated from the thermal quenching studies as the energy level for a defect state involved in the transition responsible for the 1.667 eV peak in the PL spectrum of Ga-rich, Na-free CGS film. This energy level was assigned to the Cu_{Ga} defect state from the comparison with the results of previous studies and the peak was assigned to the Cu_{Ga}-V_{Se} transition since it also disappeared after Se-annealing.

Another new defect state at 20 meV above the valence band was observed from the thermal quenching of the peak at 1.656 eV in the PL spectrum of the Cu-rich, Na-dosed CGS film after Se-annealing (S583). This energy level was tentatively assigned to the Na_{Ga} acceptor state, and this peak was assigned to the V_{Se}-Na_{Ga} transition from considerations of the activation energy and the energy difference from the band edge including estimation of Coulombic energy.

From the PL measurement results for the Cu-rich CGS films, it is concluded that the V_{Cu} is the dominant defect state, even in the Cu-rich CGS films since it has a low activation energy (50 ~ 60 meV, section 1.1.5.3) and the lowest formation energy (0.66 eV, first principles calculation in Table 1-3) of all defect states in CGS. It is also postulated that the disappearance of the peak from the $V_{Ga} - V_{Se}$ transition in the Cu-rich CGS films after Se annealing is a result of a decreased stability of V_{Ga} defect state due to the reduction of V_{Se} concentration for the formation of the stable defect pair.

The Ga_{Cu} defect state was not observed in all CGS films as a result of its deep energy level (130 meV, section 1.1.5.3) and high formation energy (3.22 eV, Table 1-4).

Therefore, it is expected that Na-dosing may not increase the hole concentration of the CGS films to the extent that it does in CIS films since the concentration of the compensating donor, Ga_{Cu} in CGS films is much lower than that of In_{Cu} in CIS films. This is a result of a large difference in their activation energies (25 meV for CIS and 130 meV for CGS, sections 1.1.5.2 and 1.1.5.3). Formation of a n-type buried junction near the surface region (section 1.1.5.3) might be achieved by the formation of a very thin layer of $Cu(In,Ga)Se_2$ with high In/Ga ratio, low Cu/(In+Ga) ratio, and with sufficient Se flux near the surface region should lead to the n-type layer from the formation of In_{Cu} shallow donor states in the layer with less V_{Ga} concentration. Of course, this will lower the band gap energy of this layer and modify the absorption process.

CHAPTER 6
STUDY OF GRAIN BOUNDARY EFFECTS IN CIS SOLAR CELLS

6.1 Theoretical Background

As in the review in chapter 1, CIGS absorber layers are polycrystalline with an average grain size on the order of a several μm. The relatively high density of grain boundaries and the associated trap states at the grain boundaries would be expected to influence device performance. It has been puzzling then that high efficiencies, as high as 19.2 % [Ram03], cells have been demonstrated using polycrystalline material, while high efficiencies can be achieved only by using single crystalline absorbers in the case of Si solar cells. In this chapter, the effects of grain boundaries in the CIS absorber layer on the device performance of /ZnO/CdS/CIS/Mo-glass solar cells were modeled using the software, MEDICI (Avant! Co.).

6.2 Electrostatics of p-n Junction Solar Cells

A solar cell is a minority carrier device. Since this study is limited to the absorber layer of CIS solar cells, only the electrostatics of p-type absorber layer will be reviewed. The transport of charged carriers in the absorber layer is described by Poisson's equation and the carrier continuity equations as follows:

$$\rho = \varepsilon \nabla E = \varepsilon \nabla \bullet (-\nabla V) = -\varepsilon \nabla^2 V = q(p - n + N_D - N_A) \tag{6-1}$$

$$\frac{\partial n}{\partial t} = \frac{1}{q} \nabla \bullet J_N - U_N + G_L, \quad where \quad J_N = q\mu_N nE + qD_N \nabla n \tag{6-2}$$

$$\frac{\partial p}{\partial t} = -\frac{1}{q} \nabla \bullet J_P - U_P + G_L, \quad where \quad J_P = q\mu_P pE - qD_P \nabla p \tag{6-3}$$

In Equations (6-1) to (6-3), ρ, ε, E and V are charge density, dielectric constant, electric field, and the electric potential, respectively. Also, p, n, N_D and N_a are the hole density, electron density, and doping density of donors and of acceptors. Equations 6-2 and 6-3 are the carrier continuity equations for holes and electrons, respectively, where q is the electronic charge, J_P and J_N are the hole and electron current density vectors that contain both drift and diffusion terms, U_i is the recombination rate for carrier i and G_L is the generation rate of an equal number of holes and electrons by light injection. In the carrier continuity equations, the recombination rate U can be represented as the sum of the band-to-band recombination, Auger recombination, and Shockley-Read-Hall (SRH) recombination [Sho52]. Band-to-band recombination is the recombination between the electrons at the conduction band and the holes in the valence band. In Auger recombination, electrons in the conduction band, first lose their energy by collision with the other electrons and then recombine with the holes in the valence band. SRH recombination is a recombination process where one or both carriers pass through states with energy levels in the band gap. Usually, band-to-band recombination as well as the Auger recombination terms are neglected as they are small compared to the SRH recombination term. The rate of SRH recombination through a single trap can be represented by the following equation:

$$U = U_{SRH} = \frac{pn - n_i^2}{\tau_p[n + n_i \exp(\frac{E_{trap}}{kT})] + \tau_n[p + n_i \exp(\frac{-E_{trap}}{kT})]}, \qquad (6\text{-}4)$$

$$where \quad E_{trap} = E_t - E_i$$

In Equation 6-4, n_i is the intrinsic carrier concentration and E_{trap} is the energy difference between the trap state level and the midgap level. τ_i is the lifetime of carrier type i and

they can be either constant or carrier concentration dependent. If the trap state in the gap acts as a trap for an electron or hole in addition to serving as a recombination center, Poisson's equation should be modified since such traps add to the net charge distribution. First, the probability of filling trap state i, f_i, for an electron or hole is as follows:

$$f_i^{electron} = \frac{\tau_{pi} n + \tau_{ni} p_{ti}}{\tau_{pi}(n + n_{ti}) + \tau_{ni}(p + p_{ti})} \tag{6-5}$$

$$f_i^{hole} = \frac{\tau_{pi} n_{ti} + \tau_{ni} p}{\tau_{pi}(n + n_{ti}) + \tau_{ni}(p + p_{ti})} \tag{6-6}$$

where τ_{pi} and τ_{ni} are the carrier life times at trap state i and p_{ti} and n_{ti} are the carrier concentrations at the trap states. For hole traps, Poisson's equation will be modified to

$$-\varepsilon \nabla^2 V = q(p - n + N_D - N_A + \sum_i N_{ti} f_i^{hole}) \tag{6-7}$$

If the trap state acts as donor state or acceptor state with a very shallow energy level, Equation 6-7 will be as follows:

$$-\varepsilon \nabla^2 V = q(p - n + N_D - N_A - \sum_i N_{ti}(f_i - 1)) \quad \text{for donor state} \tag{6-8}$$

$$-\varepsilon \nabla^2 V = q(p - n + N_D - N_A + \sum_i N_{ti}(f_i - 1)) \quad \text{for acceptor state} \tag{6-9}$$

In solar cells, the generation term, G_L in Equations 6-2 and 6-3, corresponds to the photogeneration by sun light. Photogeneration is the generation of the electron-hole pairs when the energy of the photons is larger than the bandgap of the absorber layer and it is defined by the following equation for the one dimensional case:

$$G(x) = \int_{\nu_1}^{\nu_2} G(x,\nu) d\nu = \int_{\nu_1}^{\nu_2} \beta(\nu)\alpha(\nu) S_0(\nu)(1 - R)\exp(-\alpha(\nu)x) d\nu \tag{6-10}$$

In Equation 6-10, R is the reflectivity and β is the quantum efficiency that takes into account that only a fraction of the absorbed photons generates electron-hole pairs. The term α is the absorption coefficient and S_0 is the incident photon flux per unit area, both of which are dependent on the frequency of the incident light. Therefore, if the spectrum of the impinging light and the absorption properties of the absorber layer are known, the photogeneration term can be calculated. Given information about the generation and recombination terms, the continuity equations and Poisson's equation along with appropriate boundary conditions can be solved for specified 5 layers of the solar cell device. For an ideal p-n junction solar cell with no series resistance and infinite shunt resistance, the total current is represented as the following well-known current-voltage characteristics from the solution of the previous equations [Sze81].

$$I = I_0\{\exp(\frac{qV}{kT}) - 1\} - I_L \tag{6-11}$$

where the saturation current, I_0, is given by

$$I_0 = qA\{\frac{D_n n_i^2}{L_n N_A} + \frac{D_p n_i^2}{L_p N_D}\} \tag{6-12}$$

and I_L is the photo-current by light injection. This relationship assumes there is no recombination at the front and back surfaces. Considering the recombination of the carriers by SRH recombination at the trap states near the midgap, which gives the maximum recombination rate, the recombination current should be added to the photo-generation current in Equation 6-11, which leads to the following equation. In this equation, I_{SRH0} is the reverse saturation current by SRH recombination, W is the width of the depletion region, n_i is the intrinsic carrier density and τ_{i0} is the carrier lifetime for each carrier type.

$$I = I_0\{\exp(\frac{qV}{kT}) - 1\} - I_L + I_{SRH} = I_0\{\exp(\frac{qV}{kT}) - 1\} - I_L + I_{SRH0}\{\exp(\frac{qV}{2kT}) - 1\},$$

$$with \quad I_{SRH0} = \frac{qAWn_i}{2(\tau_{p0} + \tau_{n0})} \tag{6-13}$$

The current-voltage characteristics of p-n junction solar cells, however, should be modified further because there are other parameters such as series resistance, R_s, and shunt resistance, R_{sh}. The series resistance includes the bulk resistance of the semiconductor as well as the resistance of the contacts and interconnections. The origins of the shunt resistance are related to the lattice defects such as grain boundaries or large precipitates. The equivalent electrical circuit of a p-n junction solar cell is drawn in Figure 6-1, where I_0 is the diffusion current and I_{SRH} is the SRH recombination current.

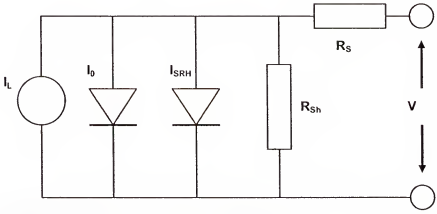

Figure 6-1 Equivalent circuit of a p-n junction solar cell

The total current including the series and shunt resistances can be represented by Equation 6-14:

$$I = I_0\{\exp(\frac{q(V - IR_s)}{kT}) - 1\} + I_{SRH0}\{\exp(\frac{q(V - IR_s)}{2kT}) - 1\} + \frac{(V - IR_s)}{R_{sh}} - I_L \tag{6-14}$$

In the device physics of the solar cells, two important device characteristics are the short circuit current, J_{SC}, (i.e., current when V = 0) and open circuit voltage, V_{OC}, (i.e., voltage when I = 0). Expressions for I_{SC} and V_{OC} can be obtained for the ideal condition. From Equation 6-14, the short circuit current is equal to the light-generated current, I_L, only if R_s is equal to zero. The following analytical expression can be obtained for the open circuit voltage when $R_s = 0$, $R_{sh} = \infty$ and $I_{SRH} = 0$.

$$V_{OC} = \frac{kT}{q} \ln\{\frac{I_L}{I_0} + 1\} \tag{6-15}$$

The general-purpose device simulation software, MEDICI, was used for the simulations of grain boundary effect in the following sections. It was developed by Avant! Co. and it has a capability of two-dimensional simulation with the consideration of SRH recombination, band-to-band recombination, and Auger recombination.

6.3 One-dimensional simulation

This section presents one-dimensional simulations that were performed to validate the codes by ensuring the results are physically reasonable results for a few well known cases. The layer structure /ZnO(transparent conducting oxide)/ZnO(n-type)/CdS(n-type)/CIS(p-type)/Mo/ was used to represent the solar cell for the simulation. The front and back contacts, ZnO and Mo, were assumed to be ohmic, each with a potential equal to the applied bias (Dirichlet boundary condition). The film thickness and physical properties of each layer are summarized in Table 6-1.

Table 6-1 The electrical properties of each layer in the device

	Thickness (nm)	Doping (cm^{-3})	E_G (eV)	ε (F/cm)	χ (eV)
CIS	2000	8×10^{16}	1.04	13.6	3.8
CdS	30	6×10^{16}	2.4	10	3.75
ZnO	50	5×10^{17}	3.3	9	4.0

To properly account for the photo-generation of carriers, the spectral distribution of incident solar energy is required. Solar spectrum depends on the air absorption that occurs before impinging the surface of the solar cell. AM0 indicates that there is no air in its path (i.e., extraterrestrial space). Non zero values of air mass are defined by the relation AM value = 1/cos(Z), where Z is the angle between the sun light and the normal of the earth's surface. Therefore, AM1 represents sun light that is impinging the surface with an angle of 90°. In this study, the solar spectrum used is the spectrum for blackbody radiation at 5800 K, which corresponds to the AM0 condition. Also, the absorption coefficient for each semiconductor layer (ZnO, CdS and CIS) is shown as in Figure 6-3.

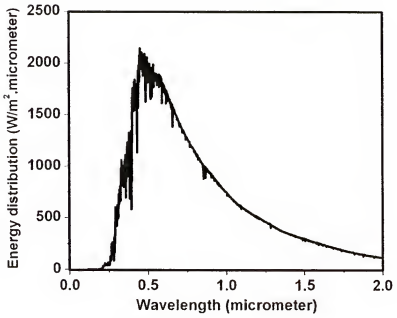

Figure 6-2. Solar spectrum for AM0 condition

As can be seen, the absorption coefficient decreases rapidly as the wavelength becomes greater than the value corresponding to the band gap energy of the semiconductor. The doping of the CIS layer was defined by acceptor states with a density of 8×10^{16} cm^{-3},

located 80 meV above the valence band, and with a carrier lifetime of 10^{-6} s both for electrons and holes. These values were selected to show the effect of the other parameters such as deeper acceptor level and compensating donors. The device model also requires the values of the electron affinity, χ, and dielectric constant, ε.

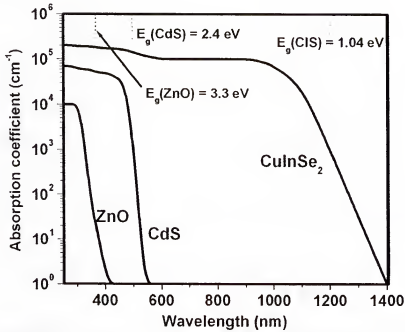

Figure 6-3 Absorption coefficient of each semiconductor layer in the device model

6.3.1 Reference Case (CIS-1)

The current continuity and Poisson's equations were solved for this case without any recombination center and trap states included in the device model. This device model is designated case CIS-Ref and will be used as the reference case to compare the influence of traps or recombination centers on the device performance. The J-V curve for this ideal case is shown in Figure 6-4 for both dark and illuminate conditions. The efficiency of the reference cell, η = 14.36%, is reasonable when compared to the experimental values for a pure CIS cell of 12% ~ 14%. The CIS cell with a record

efficiency, which was made by researchers at the National Renewable Energy Laboratory [Abu04], showed device performance parameters: V_{OC} = 0.491 V, J_{SC} = 41.1 mA/cm^2, F.F. = 0.719 and η = 19.5%. Compared to the performance parameters of the record CIS cell, the simulation results for the reference case, CIS-Ref, shows higher V_{OC} and F.F., which can be explained by the absence of trap states and a finite series resistance in the simulation. The lower value of J_{SC} for CIS-Ref can be attributed to the higher level of doping in CIS layer than that of the record cell that was not shown in their research.

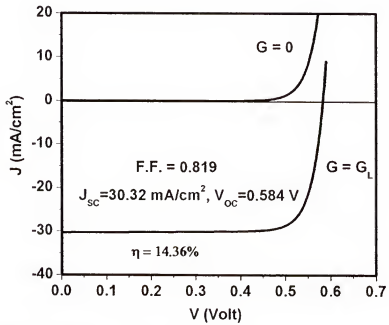

Figure 6-4 Dark and AM0 J-V curves of the reference cell, CIS-Ref

6.3.2 Impact of Deeper Acceptor and Compensating Donors in CIS Layer

The influence of compensating donors in a pure CIS cell was studied for the 3 cases summarized in Table 6-2. In the first case, the acceptor level was increased from 80 to 240 meV. This increase in energy level will change the equivalent thermally activated hole concentration. In each calculation, the hole and electron lifetimes were equal with

the value 10^{-6} s. The effect of the deeper acceptor state or the compensating donors in the absorber on the J-V characteristics is shown in the Figure 6-5. The corresponding values of V_{OC}, J_{SC}, J_0, η and Fill Factor, F.F. are shown in Table 6-3.

Table 6-2 Properties of each cell for the study of the compensation effect

	Comments
CIS-Ref	Reference cell (only acceptor states in CIS, E_A = 80 meV, $N_A = 8\times10^{16}$ cm^{-3})
CIS2	Deeper acceptor level (E_A = 240 meV)
CIS3	Compensation donor states (E_D = 240 meV, $N_D = 8\times10^{16}$ cm^{-3}, $\tau_p=\tau_n=10^{-6}$ s)
CIS4	Complete compensation by donor states (E_D = 80 meV, $N_D = 8\times10^{16}$ cm^{-3})

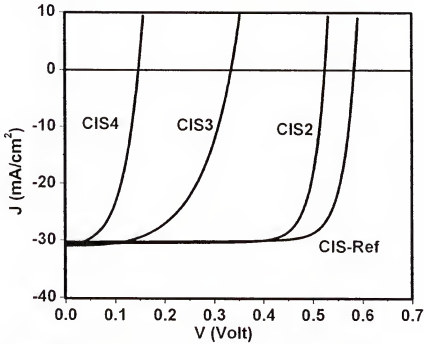

Figure 6-5 Compensation effect by donor states in the absorber layer

Table 6-3. Performances for different acceptor level and for compensating donors

	J_{SC}(mA/cm^2)	V_{OC} (V)	J_0 (mA/cm^2)	F.F	η(%)
CIS1	30.32	0.584	$\leq 10^{-10}$	0.81	14.36
CIS2	30.49	0.524	4.92×10^{-8}	0.80	12.81
CIS3	30.96	0.335	3.14×10^{-2}	0.54	5.65
CIS4	30.96	0.148	3.66×10^{-1}	0.51	2.34

As expected, each change decreased the value of V_{OC}, while there is almost no change in J_{SC}. The value of the V_{OC} is related to the dark saturation current and physically, the maximum V_{OC} is limited by the built-in potential across the p-n junction. The potential is determined by the Fermi level of the n-CdS and p-CIS layers. Thus, it is reasonable that V_{OC} decreases for a deeper acceptor state since the hole concentration decreases.

6.3.3 Impact of Electron and Hole Traps and Recombination Center in the CIS Layer

The effects of the trap states as well as the recombination centers on the device performance are also studied for the cells as in Table 6-4.

Table 6-4. Properties of each cell for the study of the effect of traps

	Comments
CIS1	Reference cell (only acceptor states in CIS, E_A = 80 meV, $N_A = 8\times10^{16}$ cm^{-3})
CIS5	Electron traps (E_t = 320 meV below CB, $N_t = 5\times10^{16}$ cm^{-3}, $\tau_p=\tau_n=10^{-6}$ s)
CIS6	Hole traps (E_t = 320 meV above VB, $N_t = 1\times10^{18}$ cm^{-3}, $\tau_p=\tau_n=10^{-6}$ s)
CIS7	Recombination center ($E_t = E_i$, $N_t = 1\times10^{17}$ cm^{-3}, $\tau_p = 8.2\times10^{-10}$ s, $\tau_n = 4.1\times10^{-10}$ s)

In Table 6-4, the energy levels of traps are located at 200 meV above midgap for electron traps and at 200 meV below midgap for hole traps. Also, the lifetime of the carriers are calculated using reasonable values for the carrier capture cross sections, $\sigma_p = \sigma_n = 10^{-15}$ cm^2 and the following equations. This value for capture cross sections is an intermediate value based on the reported range of capture cross section, $\sigma = 10^{-16} \sim 10^{-14}$ cm^{-2}, experimentally measured for silicon bicrystals [Mur91, Pal93]

$$\tau_{n,p} = \frac{1}{\sigma_{n,p} \nu_T^{n,p} N_T}, \quad \nu_T^{n,p} = (8kT/\pi m^*)^{1/2}, m_n^* = 0.2m_0, m_p^* = 0.8m_0, \quad m_0 = 9.11\times10^{-31} kg \tag{6-16}$$

where $\tau_{n,p}$ is the carrier lifetime at trap states, $\nu_T^{n,p}$ is the thermal velocity of carriers, N_T is the density of trap states, $m^*_{n,p}$ is the effective mass of the electron or hole. The

current-voltage characteristics of the cells with traps and recombination centers are shown in Figure 6-6. As shown in the figure, only the short circuit current decreased in the case of CIS5, since electron traps reduce the electron concentration and the electron is the minority carrier and contributes to the short circuit current.

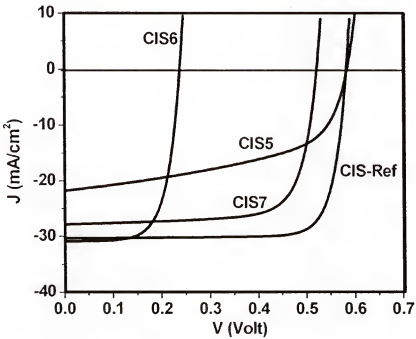

Figure 6-6 The effect of traps in the absorber layer

In contrast, for simulation CIS6, only the open circuit voltage decreased as hole traps decreased the majority carriers and the Fermi level of absorber layer, which results in decreased built-in potential. When there are recombination centers, the concentrations of both electrons and holes decrease due to the SRH recombination. Therefore, both J_{SC} and V_{OC} decrease as in simulation CIS7 in Figure 6-6. The performance parameters for each cell are summarized in Table 6-5.

Table 6-5. Performance of each solar cell for the study of the effect of traps

	J_{SC}(mA/cm^2)	V_{OC} (V)	J_0 (mA/cm^2)	F.F	η(%)
CIS-Ref	30.32	0.584	$\leq 10^{-10}$	0.81	14.36
CIS5	21.79	0.584	$\leq 10^{-10}$	0.53	6.80
CIS6	30.90	0.239	1.28×10^{-4}	0.67	4.96
CIS7	27.86	0.523	6.06×10^{-4}	0.74	10.77

6.3.4 Impact of Grain Boundaries

Considering trap states at the grain boundary of p-type material as in Figure 6-7, initially, most of the trap states will be unoccupied as the Fermi level is below most of the trap levels. Therefore, most trap states are filled with holes and there is a positive charge build-up. The positive charge build-up, in turn, results in the formation of a depletion region with higher electron density than the hole density near the grain boundary.

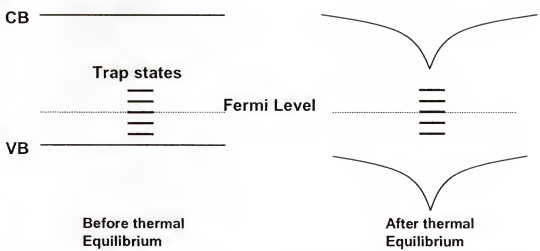

Figure 6-7. Energy band diagrams near a grain boundary region in the p-type material with trap states before and after equilibrium is obtained.

Also, electrons are attracted to the trap states filled with holes and fill the trap states by recombining with holes. This increase of the occupancy of the trap states by electrons lowers the net positive charge initially formed at the grain boundary. Therefore, the

positive charge or the potential formed at the grain boundary will find their equilibrium values depending on the doping level, light injection, and trap density. At thermal equilibrium, the Fermi level is located near midgap as in the case of the intrinsic semiconductor as in the Figure 6-7.

It is instructive to consider the impact of grain boundaries in a 1-D simulation before moving to the 2-D simulation. For the grain boundary 1-D simulation, it is assumed that a grain boundary exists at the center position of the CIS layer, which lies horizontally in the middle of the CIS layer. The localized trap state density was $3\times10^{11}cm^{-2}$ and the carrier lifetimes are $\tau_p = \tau_n = 1\times10^{-9}$ s at the midgap position ($E_t = E_i$). The recombination of carriers at these trap states as well as trapping of holes was assumed to occur by SRH recombination.

The calculated current-voltage characteristics are shown in Figure 6-8. It is observed that both J_{SC} and V_{OC} decreased compared to the values of the reference case shown in Figure 6-4 without grain boundaries. This is due to a decrease in the hole density produced by the trap states as well as the recombination of electrons with holes at the trap states that occurs to reach equilibrium as described in the explanation accompanying Figure 6-7. Energy band diagrams are shown in Figures 6-9 and 6-10 for the simulations that include light and those without light, respectively, when no bias ($V_{applied} = 0$) is applied. Band bending due to the grain boundary trap states is observed in the Figure 6-9. From the band bending, it is suggested that there positive charge has accumulated at the grain boundary and the grain boundary potential was found to be 0.358 eV.

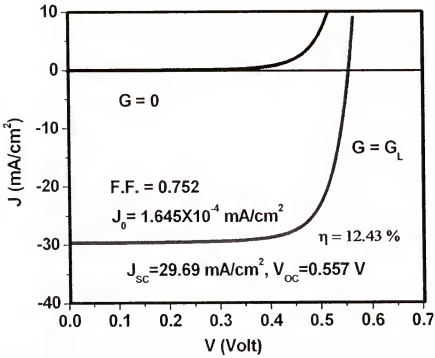

Figure 6-8 Current-voltage characteristics of a solar cell with a grain boundary at the center of the absorber layer

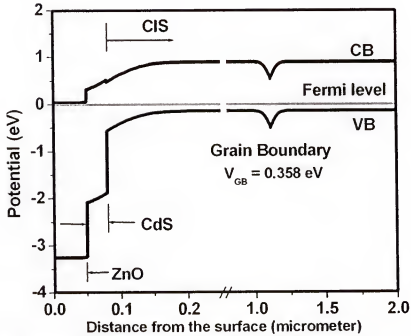

Figure 6-9 Band diagram of the solar cell with a grain boundary at the center of the absorber layer with no illumination

Figure 6-10 shows the band diagram for the case with illumination and it is observed that the grain boundary potential decreased from its value for the dark condition. The results are consistent with those by others as reviewed in Chapter 1. Also, the minority carrier current, electrons in the CIS layer, flows in the direction normal to the grain boundary as it is the direction where the potential gradient has its largest value.

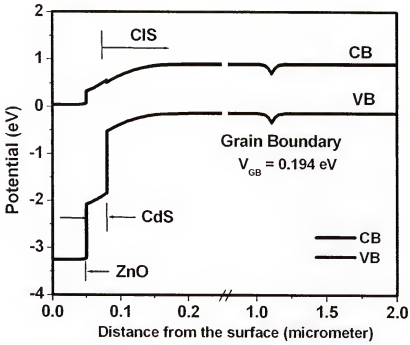

Figure 6-10 Band diagram of the solar cell with a grain boundary at the center of the absorber layer with illumination

6.4 Two-Dimensional Simulation

6.4.1 The GB Effect for a Square Rectangular Grain

The problem of a cell with rectangular GBs is a three-dimensional problem since the cell structure consists of different layers in the z-direction and GBs produce variations normal to their surfaces. The simple case of two horizontally aligned grains is the 1-D problem addressed in section 6.3.3. This case, however, does not reflect the observed

grain structures found in CIS cells. If we consider the grain boundaries as rectangular grains as schematically shown in Figure 6-11a, the problem should be solved in three-dimensions or with periodic boundary conditions on the outside boundary of the domain. It is possible to construct a 2-D problem assuming a right cylindrical geometry of the grain (Figure 6-11b). Also, if we try to solve the problem by using axi-symmetry condition, the actual grains considered in the problem are annular grains in Figure 6-11b instead of rectangular grains.

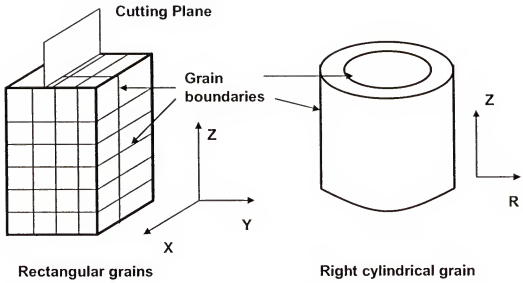

Figure 6-11 Consideration of grain boundaries in three-dimensional space

In this research, the impact of grain boundaries is simulated by using the domain formed upon slicing the structure parallel to the z-axis with a plane bisecting two grain boundaries. Therefore, the structure solved has grain boundaries that are parallel to X-Z and X-Y planes. The grain of square rectangular type explored in this research requires

specifying a characteristic length. The characteristic number is the surface area to volume ratio of the grains. Figure 6-12 shows a schematic of the actual domain solved in this study. In this problem, the boundary condition imposed at the symmetry plane was of the Neumann type boundary condition, which requires that $n \cdot \nabla V = 0$. This condition is equivalent to no surface charge on this symmetry plane and it also requires that the current not flow across this plane and the normal component of the electric field is zero.

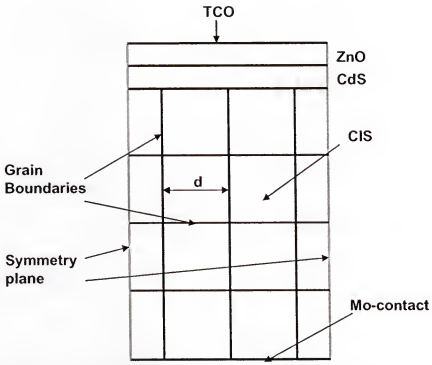

Figure 6-12. Simplification of grain boundaries solved in this study

Grain boundaries can influence device performance if they contain traps at the interfaces. This influence can be considered by evaluating the effects of the carrier lifetime at the trap state as well as the number density of the trap states and its energy level. Because there are traps at the grain boundaries, the lifetimes of the carrier at the grain boundaries decrease compared to their bulk lifetime values. The effective lifetime

is determined by the lifetime at the grain boundaries, τ_g. The lifetime associated with the trap states is defined as

$$\tau_g = \frac{1}{\sigma_g v_{th} N_t} \quad or \quad \frac{1}{\tau_g} = \sigma_g v_{th} N_t \tag{6-17}$$

where σ_g is the capture cross section of the trap state, v_{th} is the thermal velocity of carrier, and N_t is the number density of trap states. For cubic and spherical grains, the effective density of trap states in the bulk, N_t (cm^{-3}), for a given trap density at the grain boundaries, N_{ts}, can be defined by the following conservation equation:

$$SN_{ts} = N_t V, \quad 6d^2 N_{ts} = N_t d^3 (cubic) \quad or \quad \pi d^2 N_{ts} = \frac{\pi}{6} d^3 N_t (spherical), \tag{6-18}$$

where S is the surface area of a grain and V is the volume of a grain. Thus, the effective density of trap states in the bulk is defined as $N_t = 6N_{ts}/d$. The effective grain size is defined as the ratio of the volume of the grain to the surface area multiplied by 6, as $d_{eff} = 6V/S$, $d_{eff} = d$ for the case with cubic grains. In this case, from Equation 6-17 and 6-18, the following relations are obtained:

$$\tau_g = \frac{1}{\sigma_g v_{th} N_t} = \frac{d_{eff}}{\sigma_g v_{th} N_{ts}} \quad defining \quad \sigma_g v_{th} N_0 = \frac{1}{\tau_{g0}}, \quad where \quad N_0 = 10^{16} cm^{-3},$$
$$\frac{1}{\tau_{go}} \sim 10^7 s \quad then \quad \frac{\tau_{g0}}{\tau_g} = \frac{1}{d_{eff}} \frac{N_{ts}}{N_0} \tag{6-19}$$

In Equation 6-19, τ_{g0} is calculated from the values of $\sigma_g = 10^{-14}$ cm^2 and $v_{th} = 10^7$ cm/s. Therefore, the effect of grain size is also considered in the carrier lifetime through Equation 6-19. In the following two-dimensional simulations as well as the previous one-dimensional simulations, the grain boundary effect is studied by solving the continuity

and Poisson equations self-consistently with trap states at the grain boundaries and the effective life time given by Equation 6-19 instead of just specifying the recombination velocity at the grain boundaries. Therefore, the grain boundary potential as well as the carrier concentration or Fermi level was determined self-consistently.

Solar cells with square rectangular grains of 0.2 μm size (distance between the grain boundary planes), was first studied to understand the effect of GBs on the electrical properties of the cell. Figure 6-13 shows the J-V characteristics of cells with and without grain boundaries.

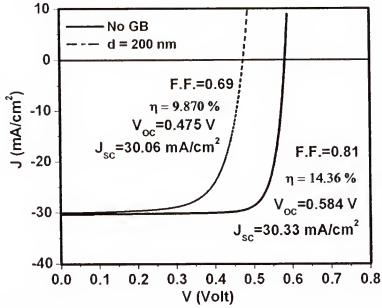

Figure 6-13 Comparison of J-V characteristics for the case with (d = 200 nm) and without grain boundaries

As shown in Figure 6-13, the trap states mainly act as the hole traps as the midgap traps are filled with holes from the adjacent p-type absorber layer. Also, a small decrease of J_{SC} is calculated, which is due to the recombination of electrons with the holes trapped at the grain boundary states. At the equilibrium state (i.e. no light injection), positive

charge is accumulated at the grain boundaries by the trapping of holes. Upon illuminating, the grain boundaries positively charged repel holes and attract electrons to the grain boundaries. Therefore, there are few holes available in the grain boundary depletion region to recombine with electrons.

The current flow lines for the solar cells with 200 nm spaced grain boundaries are shown in Figure 6-14.

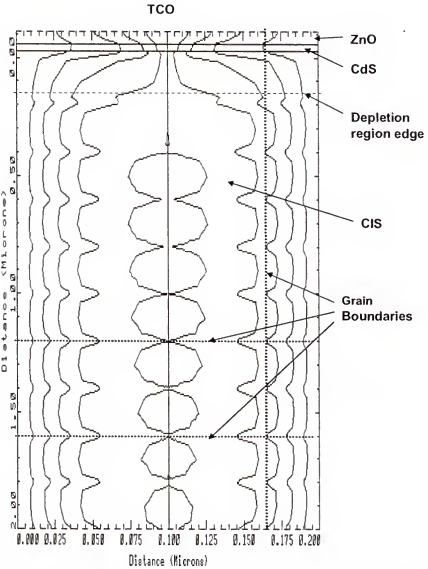

Figure 6-14 Current flow line of the solar cell with grain boundaries (d = 200 nm), the length in width direction in this figure is exaggerated

The current flow lines cross the grain boundary planes at 90°, which was previously reported [Kim01a]. The corresponding net carrier density and the potential surface are shown in the Figures 6-15 and 6-16. The depletion of carriers and potential increase along the GBs are apparent in this result. The effect is strongest where the grain boundaries intersect.

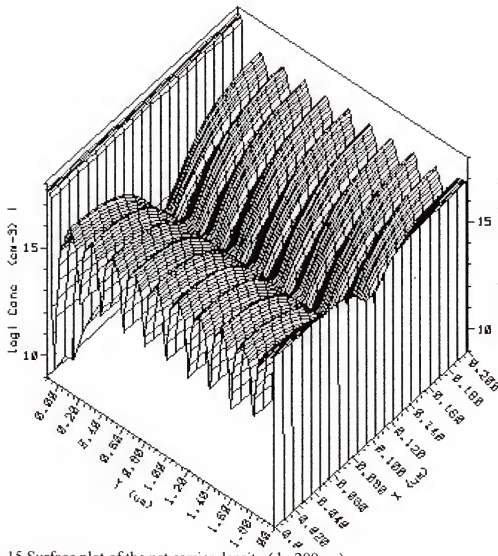

Figure 6-15 Surface plot of the net carrier density (d= 200nm)

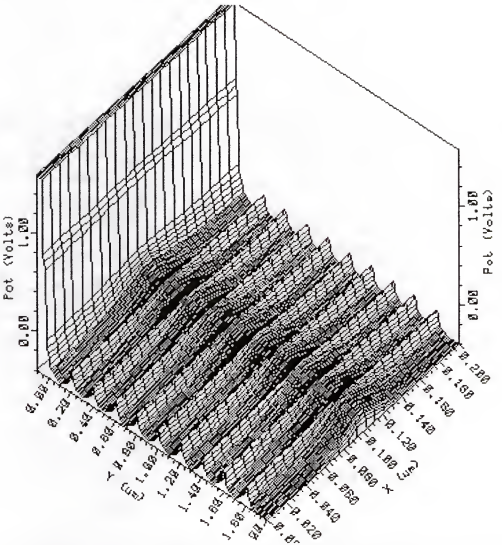

Figure 6-16 Surface plot of the potential for the cell with grain boundaries (d = 200 nm)

It is important to investigate the effect of grain boundaries as a function of grain size as grain size control has been greatly studied by the community. Therefore, in this research, the effect of grain size was studied by changing the grain size, which resulted in the change of equivalent trap density, N_t, and the carrier lifetime as in Equations 6-18 and 6-19. The simulations were performed and the resulting device performance characteristics J_{SC}, V_{OC}, F.F., η, and dark saturation current, J_0, as well as the grain boundary potential are plotted as a function of effective grain size as in Figures 6-17

through 6-21. The effective grain size is the rectangular grain size equivalent to that of spherical grains. For example, in the case of the square rectangular grain, the volume to the grain boundary surface area ratio of the grain is $d^2L/(4dL) = d/4$, where L is the length of the rectangle, which is 1.5 times the effective grain size, $d_{eff} = d/6$, as in the case of spherical grains.

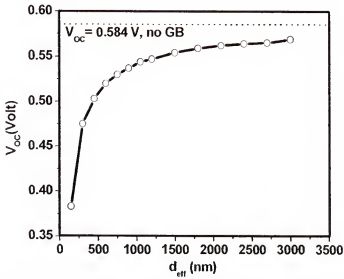

Figure 6-17. Voc of solar cells as a function of effective grain size

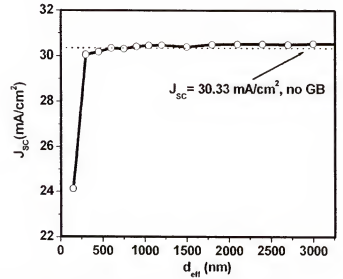

Figure 6-18. J_{SC} of solar cells as a function of effective grain size

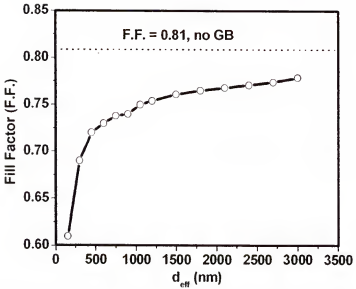

Figure 6-19. Fill factor of solar cells as a function of effective grain size

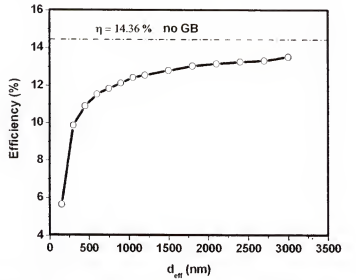

Figure 6-20. Efficiency of solar cells as a function of effective grain size.

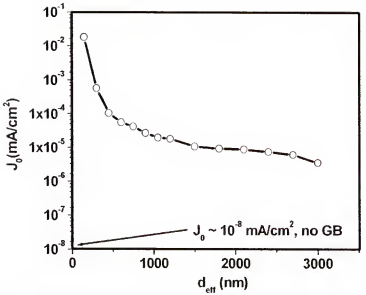

Figure 6-21. J_0 of solar cells as a function of effective grain size.

Therefore, the grain size (precisely, the distance between the grain boundaries in this case) was recalibrated by multiplying the original value by 1.5. From the figures, it is observed that V_{OC} decreases by the trapping of holes at the grain boundary states, which resulted in the decrease of efficiency. On the contrary, J_{SC} remains the same until the grain size becomes smaller than 0.3 μm. It is suggested that this grain size is related to the length of the grain boundary depletion region as $d_{critical} \sim 2L_{depletion\ region}$. The dark saturation current, J_0 is found to increase as the grain size decreases. It is suggested in Ghosh *et al.*'s work [Gho80] that the reverse saturation current, J_0, is composed of the diffusion current term and the recombination current term. They assumed that the recombination current term dominates J_0 for the small grains and suggested the relation of $J_0 \sim d^{-1}$ and this relationship showed the agreement with the experimental data. The experimental data, however, was limited. The results of this simulation did not follow this relation. Figure 6-22 is a plot of J_0 as a function of grain size in log scale.

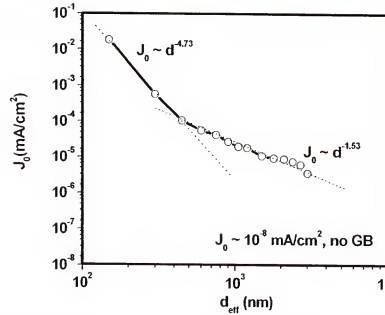

Figure 6-22. J_0 of solar cells as a function of effective grain size in log scale.

As clearly shown in Figure 6-22, there are two regions with different dependence on the effective grain size for J_0. For $d_{eff} > 450$ nm, J_0 shows the dependence on $d^{-1.53}$. For this case, it is proposed that the width of grain boundary depletion region is smaller than the half of the effective grain size, which means the depletion of the grain interior is incomplete in this case. If this is the case, there should be a diffusion of electrons to the edge of GB depletion region to be swept by the electric field and to recombine with holes at GB trap states. For this process, the diffusion process may be the rate determining step. Upon considering the expression of the dark saturation current by diffusion, the following scaling relation can be obtained.

$$J_0 \approx J_0^{diffusion} \approx 1/L_n p \sim d^{-0.5} d^{-1} \sim d^{-1.5}$$
$$, where \quad L_n = (D_n \tau_n)^{1/2} \quad , \quad \tau_n \approx \tau_g \sim d \quad and \quad p \sim N_t^{-1} \sim d \qquad (6\text{-}20)$$

In Equation 6-20, L_n is the diffusion length of electrons in CIS layer, p is the hole density in CIS layer, D_n is the diffusion constant for electrons in CIS layer, τ_n is the electron lifetime in CIS layer, which is determined by the smallest value, τ_g, and N_t is the equivalent density of GB trap states in the bulk of CIS layer. The scaling relation between J_0 and d, $J_0 \sim d^{-1.5}$, obtained shows good agreement with the exponent of d form the results by simulation.

When the effective grain size is smaller than 450 nm, the grain size can be smaller than $2L_{\text{GB depletion region}}$, which results in the total depletion of the grain interior and the electrons will be instantly swept by the electric field and recombine with the holes. In this case, the dark saturation current is determined by the recombination current term and can be represented in Equation 6-21 as in Chen *et al.*'s study [Che90].

$$J_0 \approx J_0^{recmbination} \approx 2qS_n(W)n(W), \quad where \quad S_n(W) = \frac{1}{2}v\sigma N_{tt} \exp(qV_{GB}/kT) \tag{6-21}$$

where q is a charge of electron, $S_n(W)$ is the recombination velocity at the edge of GB depletion region, n(W) is the electron density at the edge of GB depletion region, v is the velocity of electrons that is not necessarily the same as the thermal velocity, σ is the capture cross section of electrons at GB trap states, and V_{GB} is the GB potential. Upon considering Equation 6-21, it can be suggested that only v and V_{GB} are strong functions of the grain size. Therefore, it is suggested that the exponent of $d^{-4.73}$ comes from the dependence of the term, $v\exp(qV_{GB}/kT)$, on the grain size. To find the value for the width of the grain boundary depletion region, the net carrier density is plotted from top surface of the cell along the depth as in Figures 6-23and 6-24. From the result for the case

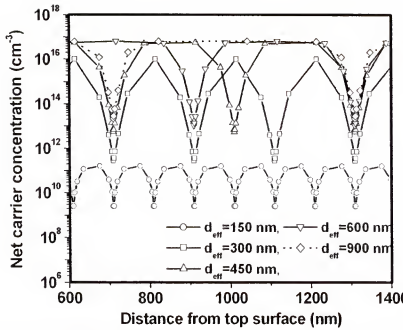

Figure 6-23 Net carrier distribution along the depth of the cell without illumination

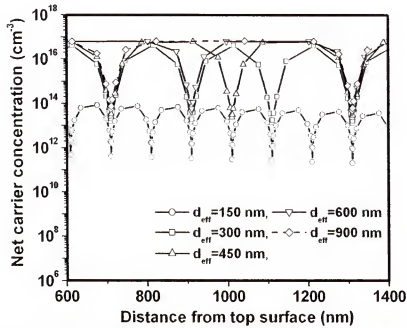

Figure 6-24 Net carrier distribution along the depth of the cell with illumination

without illumination, the critical effective grain size, where d_{eff} is equal to the twice the width of the grain boundary depletion region, $2L_{GB\ depletion\ region}$, was found to be between 300 nm and 450 nm. This value is close to the effective grain size, d_{eff} = 450 nm, where

the dependence of J_0 on d_{eff} changes. Therefore, it makes the previous assumption that the change of J_0 dependence on d_{eff} can be explained by the change of carrier transport mechanism for the recombination process reasonable. The critical effective grain size decreases to the value of 300 nm with illumination as in Figure 6-24 since the grain boundary potential and the resulting depletion region decreases with illumination from the supply of excess carriers by photogeneration.

The potential along the depth of the solar cell at the center of the grain is plotted in Figures 6-25 and 6-26. It is observed that the grain boundary potential decreased almost by 100 meV with light injection for the case with 300 nm grains while there is very slight decrease in the case of large grain size (d = 1200 nm).

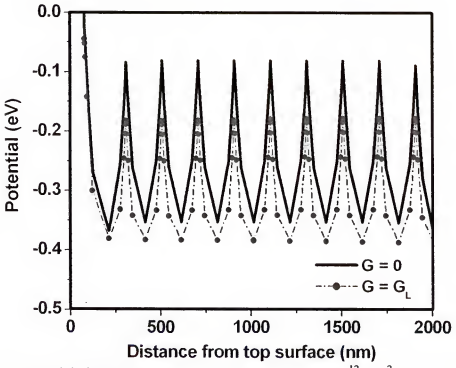

Figure 6-25 Potential along the depth of the solar cells ($N_T = 10^{12}$ cm^{-2}, d_{eff} = 300 nm)

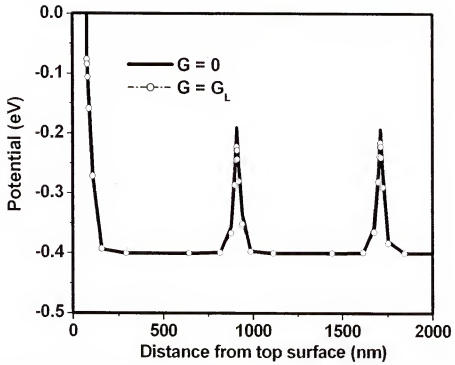

Figure 6-26 Potential along the depth of the solar cells ($N_T = 10^{12}$ cm^{-2}, d_{eff} = 1200 nm)

This difference is a result of the grain being nearly fully depleted at small grain size since the impact of adjacent grains overlap. Thus the supply of the holes as well as electrons with illumination decreases the charge accumulation at the grain boundaries and produces a new steady state charge distribution. It is also observed in the figure that the grain boundary potential increases with decreasing grain size. When the grain size decreases, the probability of filling the trap states with holes increases as the equivalent trap density in the bulk CIS layer, N_t, increases. Therefore, there is more positive charge build-up and the increase of grain boundary potential at GBs.

Figure 6-27 shows the effect of the trap density at the grain boundaries on the potential profile of the solar cell.

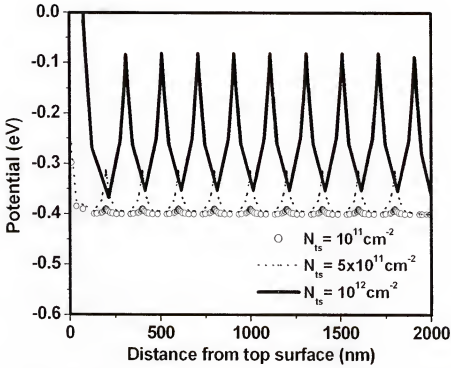

Figure 6-27 Potential variation for different trap density along the grain boundaries (d = 200 nm)

The calculation shows that the grain boundary potential or the barrier height for hole transport decreases with decreasing trap density as the probability of filling the trap states with holes decreases with decreasing trap density.

6.4.2 Effect of the GB orientation

In the real solar cells, the absorber layers of the best cells are known to have the columnar grain structures or vertically oriented GBs. Also, it is required to have the minority carrier transport in the thickness direction of the absorber layer to obtain the solar cells with good performance. Therefore, it is expected that GBs with different orientation affect the device performance in a different manner.

In this section, the orientation of GBs were studied by considering the GBs with only one orientation, which are vertical only GBs (VGB) and horizontal only GBs (HGB) as in Figure 6-28.

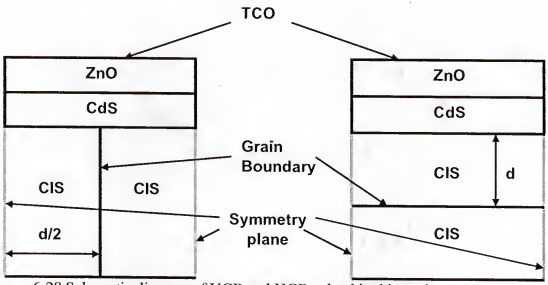

Figure 6-28 Schematic diagram of VGB and HGB solved in this study

As in Figure 6-28, the effective grain size in VGB and HGB are defined as the ratio of the volume of the grain to the grain boundary surfaces multiplied by 6 as before.

$$d_{eff} = 6V/S = 6dWL/(2WL) = 3d = 3d_{cubic} = 2d_{square\ rectangular} \tag{6-22}$$

Figures 6-29 through 6-33 are the device performance characteristics J_{SC}, V_{OC}, F.F., η, and dark saturation current, density J_0, (as well as the grain boundary potential) as a function of effective grain size. The results for the case with square rectangular grains are also included in the figures for the comparison purpose. Figure 6-29 shows that VGB shows more effect on V_{OC} than HGB and the value of V_{OC} when the grain size is large is also small for the case of VGB. From the calculation, it was found that the length of the depletion region in CIS layer is 88 nm as in section 6.4.2.

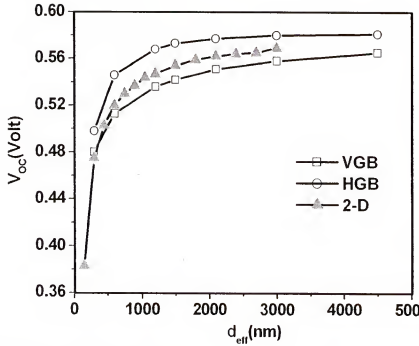

Figure 6-29 The effect of GB orientation on V_{OC}

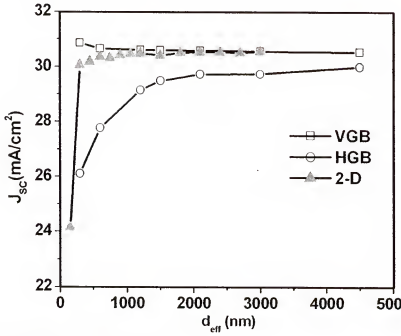

Figure 6-30 The effect of GB orientation on J_{SC}

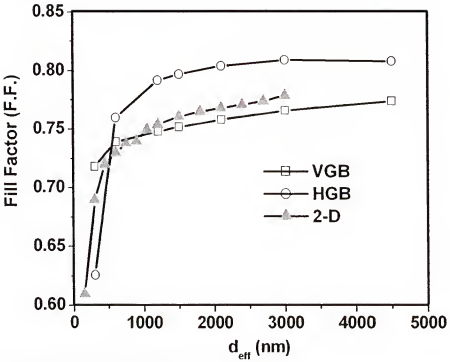

Figure 6-31 The effect of GB orientation on Fill Factor

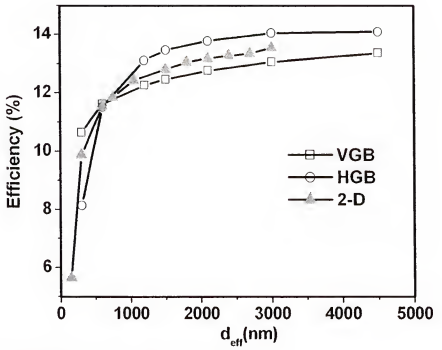

Figure 6-32 The effect of GB orientation on efficiency

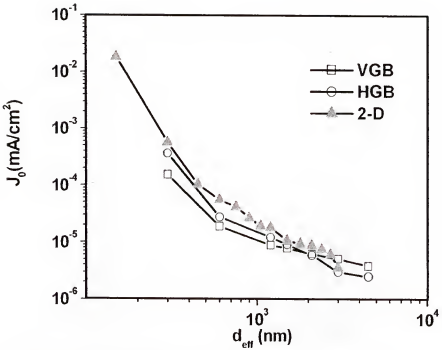

Figure 6-33 The effect of GB orientation on J_0

Therefore, even when d has the smallest value (d = 100 nm), there is no GBs in the junction depletion region in the case of HGB while there are always GBs in the case of the VGB regardless of the grain size. When the GBs are in the junction depletion region where the carriers are depleted, the effect of GBs is enhanced by the increased recombination velocity due to the electric field and the built-in potential that is related to V_{OC} decreases.

The short circuit current, J_{SC} shows different behavior from that of V_{OC} for the GB orientation effect. While VGB remains almost constant with grain size, HGB shows lower value compared to the values in the case of VGB and decreases with grain size below the effective grain size of ~ 2000 nm. Contrary to the case of VGB, the minority carrier electrons should surmount the barrier at GBs to reach the junction depletion

region and to contribute J_{SC}. The decrease of J_{SC} in the case of HGB, therefore, can be attributed to the barrier effect of HGB that are normal to the transport of the electrons.

The efficiency as well as F.F. shows the combined behavior. When the grain size is large, VGB shows lower efficiency since the V_{OC} is lower in the case of VGB while the differences in J_{SC} are not large. When the grain size is small, J_{SC} decreases rapidly in the case HGB and the differences of V_{OC} between VGB and HGB become negligible, which results in the lower efficiency for the case of HGB. The dark saturation current, J_0, shows the similar behavior as the 2-D case with square rectangular grains.

6.4.3 Effect of the Junction Depletion Region on the GB Effect

As discussed in the section 6.3.4, the grain boundary potential at thermal equilibrium is determined by the trapping of the holes at GB states, and the resulting recombination of the trapped holes with the electrons. As the carrier density and the transport process of the carriers are different for the quasi-neutral region and the junction depletion region, it is expected that the effect of GBs is different when the fraction of GBs in the junction depletion region is different or the width of the junction depletion region changes.

In this section, the effect of the junction depletion region on the GB effect was studied by considering the effect of GBs for the cases with VGB and HGB with higher CdS/CIS doping ratio of 15 ($/6\times10^{17}$ cm^{-3}/4×10^{16} cm^{-3}/) than the reference case with a ratio of 0.75 ($/6\times10^{16}$ cm^{-3}/8×10^{16} cm^{-3}/) doping ratio. This higher CdS/CIS doping ratio indicates the increase of the junction depletion region. The length of the depletion region in the p-side, x_p of the homojunction p-n diode, is represented as Equation 6-23 from the solution of the Poisson equation.

$$x_p = [\frac{2K_s\varepsilon_0}{q}\frac{N_D}{N_A(N_A+N_D)}V_{bi}]^{1/2} \quad , where \quad V_{bi} = \frac{kT}{q}\ln(\frac{N_A N_D}{n_i^2}) \tag{6-23}$$

In equation 6-23, K_s is the dielectric constant of the CIS layer, ε_0 is the dielectric constant of the vacuum (8.85×10^{-14} F/cm), q is the charge of a electron, N_A is the doping of the p-type CIS layer, N_D is the doping of the n-type CdS layer, V_{bi} is the built-in potential of the p-n diode, n_i is the intrinsic carrier concentration for p-side and n-side, respectively. From Equation 6-23 and the values of the parameter, x_p and V_{bi} for each case were calculated as in Table 6-6. In Table 6-6, the doping density of CIS layer for each case was calculated from the acceptor energy level of 80 meV from the valence band, and the density of acceptor state 8×10^{16} cm^{-3}, 4×10^{16} cm^{-3} for each doping ratio from the simulation.

Table 6-6 The length of the depletion region in the CIS layer and built-in potential in each doping ratio

	Doping ratio (CdS/CIS)	V_{bi} (V)	x_p (nm)
Reference	(6×10^{16} cm^{-3}/6.6×10^{16} cm^{-3})	0.798	93
High doping ratio	(6×10^{17} cm^{-3}/3.6×10^{16} cm^{-3})	0.842	183

However, Equation 6-23 can be only applied for the homojunction diode. For the heterojunction p-n diode, Equation 6-23 can be modified as Equation 6-24 [Wol89].

$$x_p = [\frac{2\varepsilon_{s,n}\varepsilon_{s,p}}{q}(\frac{N_D}{N_A(N_a\varepsilon_{s,p}+N_D\varepsilon_{s,n})})V_{bi}]^{1/2} \quad ,$$
$$where \quad V_{bi} = \frac{1}{q}[\frac{\Delta E_C - \Delta E_V}{2} + kT\ln(\frac{N_A N_D}{n_i^p n_i^n})] \tag{6-24}$$

In Equation 6-24, $\varepsilon_{s,n}$ and $\varepsilon_{s,n}$ are the dielectric constant of CdS and CIS, K_s multiplied by ε_0 respectively, ? E_C is the difference of the electron affinity, χ_p - χ_n, and ? E_V is defined as χ_n - χ_p + E_g(CdS) - E_g(CIS). The values for each parameter are shown in Table 6-7, and V_{bi} and x_p are calculated as in Table 6-8.

Table 6-7 The parameters for the calculation of the depletion region in the CIS with heterojunctions equations

	χ (eV)	E_g (eV)	n_i (cm^{-3})	K_S	$N_{A,D}$ (cm^{-3})
CdS	3.75	2.4	1.28×10^{10}	13.6	6×10^{16}
CIS	3.8	1.04	0.04778	10.0	6.6×10^{16}/3.6×10^{16}

Table 6-8 The length of the depletion region in the CIS layer and built-in potential in each doping ratio with heterojunctions equations

	Doping ratio (CdS/CIS)	V_{bi} (V)	x_p (nm)
Reference (HGB,VGB)	(6×10^{16} cm^{-3}/6.6×10^{16} cm^{-3})	0.850	88
High doping ratio (HGB_H, VGB_H)	(6×10^{17} cm^{-3}/3.6×10^{16} cm^{-3})	0.894	186

The values, x_p in each case obtained by Equation 6-24 are not much different from those by Equation 6-23 and it is observed that the width of p-side depletion region increased from 88 nm to 186 nm by increasing the doping ratio. The device performance parameters for the reference cases, HGB and VGB, and the cases with high doping ratio (HGB_H and VGB_H) are shown as in Figures 6-34 through 6-38.

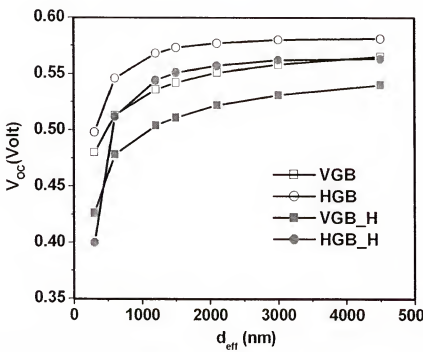

Figure 6-34 The effect of the depletion region width on the GB orientation effect on V_{OC}

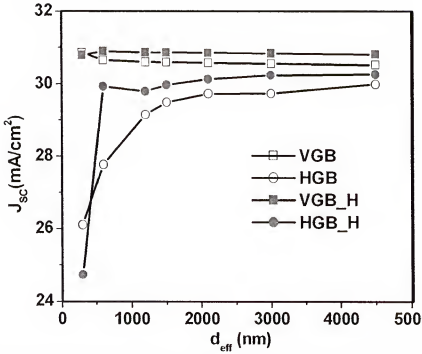

Figure 6-35 The effect of the depletion region width on the GB orientation effect on J_{SC}

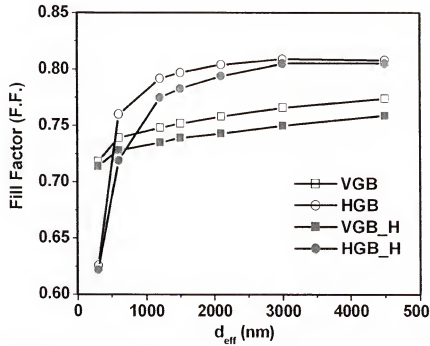

Figure 6-36 The effect of the depletion region width on the GB orientation effect on F.F.

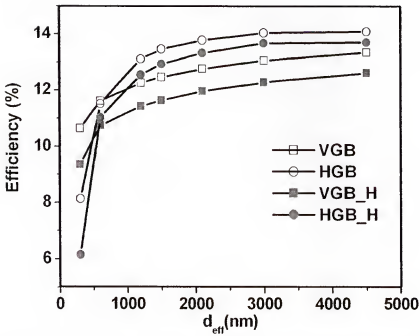

Figure 6-37 The effect of the depletion region width on the GB orientation effect on η

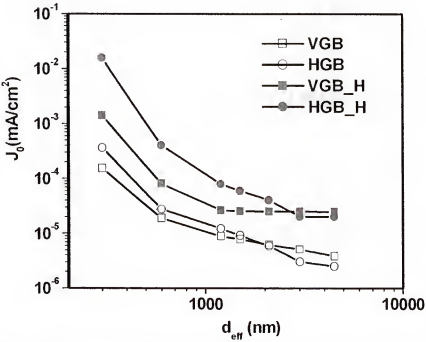

Figure 6-38 The effect of the depletion region width on the GB orientation effect on J_0

First, considering V_{OC}, VGB_H shows lower V_{OC} than VGB for all grain sizes. As shown in the calculation before, the length of the p-side depletion region is larger in the case of the high doping ratio, VGB_H than VGB. Therefore, more fractions of the vertical GBs will be located in the junction depletion region where the GB effect is enhanced, in the case of VGB_H. While HGB shows higher V_{OC} values for all grain sizes in the case of the reference doping ratio, HGB_H shows lower V_{OC} value than that of VGB_H for the smallest grain size (d = 100 nm). As x_p for the case with high doping ratio was calculated as 186 nm, it is obvious that when the grain size is the smallest, the first GB in CIS layer is completely located inside of the junction depletion region. Therefore, this behavior can be explained as the depletion region becomes larger enough to include one GB in the case of HGB_H.

In the case of J_{SC}, the cases with the high doping ratio show the same behavior as the reference cases, which showed lower values for the case of HGB due to the barrier effect to the transport of electrons. The values of J_{SC} for the high doping ratio cases, however, are larger than the reference cases. It can be attributed to the lower doping level of the CIS layer (3.6×10^{16} cm^{-3}) compared to the doping level (6.6×10^{16} cm^{-3}) in the case with reference doping. However, J_{SC} of HGB_H shows smaller value than that of HGB when the grain size is 100 nm, and one GB is completely included in the junction depletion region as shown in Table 6-6.

The cases with the high doping ratio show lower values of the efficiencies compared to the cases with the reference doping. This decrease of the efficiencies is mainly attributed to the decrease of V_{OC} that results from the reduction of the hole densities with more GBs in the junction depletion region and the increased recombination.

This increase of the recombination for the cases with high doping ratio (HGB_H, VGB_H) is also observed in the Figure 6-38 as both HGB_H and VGB_H show higher J_0 values than HGB and VGB, respectively.

6.5 Summary and Conclusions

The effect of grain boundaries on solar cell performance was investigated using two-dimensional simulation for a /ZnO/CdS/CIS/ cell structure. The influence of grain size and localized trap density was studied for square rectangular GBs. The grain boundary was simulated by placing hole trap states at the grain boundaries. SRH recombination of trapped holes at grain boundary trap states with electrons was allowed and the decrease of the minority carrier lifetime with decreasing grain size was also considered. The continuity equation and Poisson equation were solved self-consistently to determine the grain boundary potential as well as the Fermi-level at the grain boundary.

The calculation results indicate that the grain boundaries strongly influence V_{OC} through the trapping of holes. This drop on V_{OC} decreases the fill factor and the efficiency of the cell. If the grain size is smaller than a critical effective grain size, however, it appears that the entire region of the absorber layer becomes depleted and J_{SC} sharply decreases. The dark saturation current is also observed to increase with decreasing grain size. As the dark saturation current is composed of the recombination current and the diffusion current, it can be explained by the increasing recombination current due to the increase of effective trap density as well as the increase of the diffusion current from the reduced majority carrier density in the absorber layer. From the dependence of dark saturation current, J_0, on the effective grain size, d_{eff}, two regions of J_0 were found to have a different carrier transport mechanism for the recombination of

electrons with trapped holes at GBs. For the grain size larger than the critical grain size, $d_{critical}$ (450 nm in this study) the diffusion of electrons to the edge of the depletion region determines the rate of recombination and the dark saturation current. In this case, J_0 is found to depend on $d_{eff}^{-1.5}$ from the scaling of the variables for J_0 and it agrees very well with the dependence of $J_0 \sim d_{eff}^{-1.53}$ obtained form the simulation results. For d_{eff} smaller than $d_{critical}$, it appears that the interior of the grain is completely depleted and the electric field in the grain and the GB potential increases the rate of electron transport to the trap states at GBs. Therefore, it is proposed that this change of electron transport mechanism gave the different dependence of J_0 on d_{eff}, $J_0 \sim d_{eff}^{-4.73}$, obtained from the simulation results. The critical grain size was also calculated from the plot of the net carrier density in the grain and the value, d_{eff} (300 ~ 450 nm) from the carrier distribution in the cell, shows good agreement with the value from the analysis of J_0. The decrease of grain boundary potential with light injection is observed only for cells with small grains. It is because, for large grain size, there are sufficient carriers to fill the traps (lower effective trap density) even without illumination. The increase of grain boundary potential with trap density at GBs was observed and it indicates that as the trap density increases, the effective trap density increases, which results in the increase of filling probability of traps and the positive charge build-up at trap states.

The orientation of GBs (VGB and HGB) has different effect on each performance parameter. The case, VGB shows lower V_{OC} values for all grain sizes. With the length of the depletion region of 88 nm in CIS layer, all GBs in the case of HGB are outside of the junction depletion region while part of the GBs are always in the junction depletion region in the case, VGB. The existence of GBs in the junction depletion region results in

the decrease of V_{OC} from the reduction of the carrier density since the recombination at GBs is enhanced due to the electric field in junction depletion region.

Contrary to the effect of GB orientation on V_{OC}, HGB shows lower J_{SC} values than VGB and decrease rapidly below the grain size of ~ 2000 nm while VGB shows no dependence on the grain size. It indicates that the horizontally oriented GBs in the case of HGB act as the barriers to the transport of electrons that contribute to J_{SC}. Also, the rapid decrease of J_{SC} for small grain size can be explained as the decrease of electron density by the increased recombination.

Fro the efficiency and F.F., VGB shows lower efficiencies due to the decrease of V_{OC} with the enhanced GB effect in the junction depletion region. For small grain sizes, HGB shows lower values both for the efficiency and fill factor than VGB as J_{SC} decreases rapidly with negligible differences of V_{OC} between VGB and HGB.

When the doping ratio of the CdS layer to the CIS layer increases, the length of the depletion region in the p-side CIS layer increases. With the increase length of the p-side depletion region (186 nm), HGB_H shows lower V_{OC} value than that of VGB_H for the smallest grain size (d = 100 nm) while HGB showed higher V_{OC} values for all grain sizes than VGB. It indicates that the junction depletion region can affect the GB orientation effect when the depletion region width is large enough to include the whole horizontal GB. In other word, it appears that V_{OC} mainly depends on the fraction of the GBs in the junction depletion region through the increased recombination.

For the cases with high doping ratio, J_{SC} shows the same behavior as in HGB and VGB, which means that HGB_H shows lower values of J_{SC} than VGB_H. The larger values of J_{SC} for HGB_H and VGB_H, however, than the reference cases is attributed to

the fact that the doping level of the CIS layer (3.6×10^{16} cm^{-3}) is lower than that of CIS (6.6×10^{16} cm^{-3}) in the cases, HGB and VGB, which results in the increased minority carrier current. Also, the smaller value of J_{SC} in the case of HGB_H than the J_{SC} of HGB indicates that the complete inclusion of one horizontal GB with the small grain size (100nm) resulted in the increased GB effect in this case.

The lower efficiencies for the cases with the high doping ratio mainly result from the decreased V_{OC} due to the reduction of hole density than the reference doping ratio. It can be explained due to the increased recombination with more GBs in the junction depletion region. The increase of the recombination current was also observed for the cases with high doping ratio (HGB_H, VGB_H) from the increase J_0 values and it indicates the increased recombination rate due to the more GBs in the junction depletion region.

CHAPTER 7
CONCLUSIONS

7.1 Epitaxial Growth of $CuInSe_2$ at Low Temperature

The role of Cu-Se secondary phase in the epitaxial growth of CIS films was investigated in this research. The presence of a Cu-Se secondary phase in Cu-rich CIS films assists in the epitaxial growth of CIS on (100) GaAs by increasing the mobility of adatoms and making the growth adopt a Stranski-Krastanov mode. Three films were studied in detail, which were grown under identical conditions except that the Cu/In atomic ratio was varied from In-rich to Cu-rich. The surface morphology of Cu-rich CIS films showed an almost featureless matrix region surrounding island-like areas of high roughness. The segregation of a Cu-Se secondary phase on the surface of island and matrix regions of Cu-rich CIS films was observed in both SEM images, EPMA composition analysis and confirmed by TEM-EDX line scan. TEM-EDX scan showed that a Cu-Se phase mainly exist on the surface of the film and at the grain boundaries.

Pole figure analysis showed that the matrix region of the Cu-rich CIS films grew epitaxially with the same orientation as that of the GaAs substrate. In addition, CuAu (CA)-like CIS was observed in Cu-rich CIS films and it is believed from GIXRD analysis that the CA-like CIS phase is present in the island regions of the film. There was no epitaxial growth observed in the In-rich CIS film, which supports that a Cu-Se phase plays a key role in enhancing adatom mobility and producing the epitaxial growth of Cu-rich CIS films. From TEM SAD patterns, it is shown that island region consists of large

grains, which are single crystals individually and have the same orientation as the matrix region but slightly rotated.

From the lattice parameter calculation, it was shown that the epitaxially grown Cu-rich CIS films were nearly fully relaxed and it was also observed by SEM micrographs that the thickness of the matrix layer right below the island region was thicker than that without islands on top of it.

From those observations, the following growth model is suggested. For Cu-rich CIS films, it is proposed that during the initial stage of the growth, there is a formation of nucleation sites with the increased mobility of adatoms by the Cu-Se phase. The film continues to grow with 2-D growth mode until its thickness is less than the critical thickness with increased adatom mobility to the nucleation sites. At this stage, the nucleation sites have grain boundaries formed from the nucleation process, and they can relieve the heteroepitaxial strain between the film and the GaAs. Also, the Cu-Se phase is segregated on the surface at this stage. After a critical thickness of CIS film is deposited, the matrix region forms the surface undulation structure with {112} surfaces to release the heteroepitaxial stress by forming the surfaces with the lowest surface energy. Also, as the chemical potential of the nucleation sites where grain boundaries are concentrated is lower than the matrix region, there is a driving force of the material transfer to these nucleation sites, which results in the faster growth rate and the formation of the island structures. Therefore, the Cu-rich CIS films grow with island structures of larger thickness on two-dimensional matrix layer.

For In-rich CIS film, the increase of the surface mobility of adatoms introduced by the Cu-Se phase is not sufficient to induce two-dimensional layer growth at this relatively

low growth temperature. It is also possible there is insufficient Cu to form the Cu-Se surfactant layer, and thus only the domains with larger grain size are formed. Hence, the In-rich CIS film grow as a three-dimensional layer, following a Völmer-Weber (V-W) mode at this low growth temperature.

7.2 Epitaxial Growth of $CuInSe_2$ and $CuGaSe_2$ at High Temperature

In this research, the growth mode and the crystal structures of each phase in the epitaxial CIS and CGS film were studied.

At high growth temperature, CIS films were grown heteroepitaxially with fully relaxed state as in the case of low temperature growth. With increased growth temperature, it appears that there is no need for a Cu-Se secondary phase to increase the mobility of adatoms. Two-dimensional layer-by-layer growth was observed for In-rich CIS films with very few island structures on the surface, while the Cu-rich films showed the island structures, which are elongated and oriented in the same [01 -1] direction as in the case of low temperature growth. All as-grown CIS films showed good crystal qualities and it appears that with enough adatom mobility, a Cu-Se secondary phase does not help to get a good crystal quality from the larger FWHM value for Cu-rich CIS films than In-rich CIS films. From the XRD space map, all films are confirmed to have grown fully relaxed state. Cu diffusion from the film to the substrate was observed in the CIS films and it is suggested that this Cu diffusion led to the formation of a buffer layer near the interface region that is responsible for the small bump in XRD θ–2θ scan near GaAs (400) peak. The fully relaxed growth was also confirmed by TEM SADP at the interface between CIS film and the GaAs substrate for all CIS films and it is also confirmed that the orientation of all epitaxial CIS films is the same as that of GaAs substrate. Diffraction

spots for twins were observed in the SADP of island structures of CIS films and it is suggested that the strain form lattice mismatch is relieved by the formation of twins. It is observed that the growth mode of CIS films did not change by Na dosing. However, with increased adatom mobility by Na dosing, the segregation of the epitaxial $Cu_{1.5}Se$ phase was observed in the top part of the island structure in the Cu-rich CGS film with Na dosing. The in-plane lattice constant of $Cu_{1.5}Se$ phase, which is also grown heteroepitaxially on the epitaxial CIS in the island region, was also calculated as 5.784 Å from the TEM-SADP analysis.

The morphologies of Cu-rich CGS films were similar to those of Cu-rich CIS films grown at low temperature, which have island-matrix structures. The increased adatom mobility by Na dosing as in the case of CIS film, led to the more elongation of the island structures in the Cu-rich CGS film with Na dosing in the [01-1] direction, which can be explained by the surfactant effect of Na. The excess Cu in Cu-rich CGS films was segregated to form the top part of the faceted island structure and it was identified as $Cu_{1.5}Se$ phase. Regardless of Na dosing, spherical island structures were observed on the epitaxial matrix region in Ga-rich CGS films. While all CGS films grew epitaxially, the spherical island structures were observed to consist of many grains and twin structures were also observed in the island region. Nearly pseudomorphic growth of all CGS films were observed by XRD space map and the best crystal quality of Cu-rich, Na dosed CGS film was observed by the lowest FWHM value for XRD rocking curve ever reported. The bump observed in the case of CIS films grown at high temperature was also observed in the XRD θ–2θ spectra of Cu-rich CGS films. This bump indicates the formation of the buffer layer with smaller in-plane lattice constant than the GaAs (better lattice match to

the in-plane lattice constant of CGS) near the interface region and it is suggested to reduce the heteroepitaxial strain, which led to the nearly pseudomorphic growth of Cu-rich CGS films. Contrary to the case of CIS films, it appears that the adatom mobility was not enough in the case of CGS films growth and the surfactant effects of Cu-Se secondary phase and Na dosing were necessary for the epitaxial growth.

Pseudomorphic growth of all CGS films was also confirmed by TEM –SADP analysis. The Cu-Se phase in the top part of the island structure of Cu-rich CGS films was identified as a $Cu_{1.5}Se$ phase by TEM-EDX. The epitaxial growth of $Cu_{1.5}Se$ phase to the below CGS region, was also confirmed by TEM-SADP analysis. The in-plane lattice constant of the $Cu_{1.5}Se$ phase observed in both Cu-rich CGS films was calculated as 5.764 Å (Cu-rich CGS without Na-dosing) and 5.753 Å (Cu-rich CGS film with Na-dosing), respectively and it was found the $Cu_{1.5}Se$ phase was strained to CGS below it. Many grains and twin structures were observed in the spherical island structure of Ga-rich CGS films. Twin structures were also observed in the island structure of Cu-rich CGS films, which are again though to relieve the stains in the film.

From the fact that all CIS films grew with relaxed state while all CGS films showed nearly pseudomorphic growth, it is postulated as follow. If we compare the in-plane lattice constants of CIS film (a = 5.782 Å) and CGS film (a = 5.614 Å) with that of GaAs (a = 5.654 Å), the inter-atomic distance should decrease for the case of CIS film, while that of CGS film should increase to match the lattice constant of GaAs for pseudomorphic growth. It is well known that the inter-atomic potential is anharmonic and increases more rapidly as the inter-atomic distance decreases than the inter-atomic distance increases from its equilibrium value [Mar95]. Therefore, it can be assumed that

CIS film is likely to maintain their in-plane lattice constant during the epitaxial growth while CGS films is likely to be deformed (expanded) to match the lattice constant of GaAs, which resulted in the pseudomorphic growth. Also, from the observation of the bump in the XRD spectra for both CIS and CGS films (as in sections 3.4.1 and 4.4.1), it was proposed that a very thin buffer layer exists in the GaAs substrate, which resulted in the reduction of the heteroepitaxial strain. The formation of this buffer layer is attributed to the diffusion of Cu atoms into the GaAs substrate that is observed by TEM-EDX line scans of the cross section of In-rich CIS film without Na-dosing (W560) and Cu-rich CGS film without Na-dosing (W552). The diffusion of Cu atoms into the GaAs in all CGS films were also confirmed by the observation of the bound exciton ($Cu_{Ga} - V_{Se}$ related) related peak by photoluminescence in Chapter 5.

7.3 Photoluminescence Study of Epitaxial $CuGaSe_2$ Films

The effects of Cu/Ga ratio, Na dosing and Se-annealing on the defect structure of CGS films were investigated by low temperature PL and the temperature quenching of the specific peaks involved in the selected transitions.

PL peak observed near 1.5 eV in all CGS films was assigned to the transition by the excitons bound to the $Cu_{Ga} - V_{As}$ defect pair. This result confirms the diffusion of Cu atoms into the GaAs substrate in all CGS films, and supports the postulation of the formation of a buffer layer in the GaAs substrate as in Chapter 4.

PL peaks near 1.67 eV and 1.647 eV for CGS films were identified as the V_{Cu}-CB transition and the V_{Ga}-V_{Se} transition, respectively, from the previous studies and the thermal quenching. Energy levels of 10 meV and 21 meV were calculated for the Cu_{Ga} and V_{Ga} defect states from the thermal quenching of the peak at 1.667 eV of Ga-rich CGS film and the peak at 1.647 eve of Cu-rich CGS film, respectively. Defect state at 20 meV

above valence band was observed from the thermal quenching of the peak at 1.656 eV for the Na-dosed, Cu-rich CGS film after Se-annealing and it was tentatively assigned to the Na_{Ga} acceptor state. The diffusion of Na into the GaAs substrate was also postulated from the observation of the PL transition peak related to the Cu_{Ga}-Na_I-related transition peak in the PL spectra of Ga-rich and Na-dosed CGS film after Se annealing

7.4 Study of the Grain Boundary Effect on $CuInSe_2$ Solar Cell

The effect of grain boundaries (GBs) on the cell performance parameters was studied by performing two-dimensional simulation using software MEDICI (Avant! Co.). The solar cell with a structure of /ZnO/CdS/CIS/Mo-glass was used for the study of the GB effect. The grain boundary effect was considered through the trapping of holes at the trap states located at GBs and the SRH recombination of trapped holes with the electrons. The decrease of minority carrier lifetime with decreasing grain size was also considered. Both continuity equation and the Poisson equation were solved self-consistently in this study.

V_{OC}, fill factor and the efficiency of the solar cell were decreased with decreasing grain size by GB effect, which is the trapping of holes and the recombination at GB states, while there was not much change in J_{SC}. After the grain size becomes smaller than the critical size, which is related to the length of the GB depletion region, the entire region of the grain interior becomes depleted and J_{SC} decreases rapidly after that point. The dark saturation current is observed to increase with decreasing grain size and it indicates the increasing recombination current from the increase of the effective trap density and the increase of the diffusion current from the reduced majority carrier density in the absorber layer.

Two regions were found for the dependence of J_0 on d_{eff} by the analysis of the simulation results. For d_{eff} smaller than $d_{critical}$, the dependence was found as $J_0 \sim d_{eff}^{-4.73}$ while it was found as $J_0 \sim d_{eff}^{-1.53}$ for d_{eff} larger than $d_{critical}$. It was proposed that the diffusion process to the GB depletion edge dominates the recombination when the grain size is large and the depletion of the grain interior is incomplete. From the scaling analysis of the diffusion current, it was found that J_0 depends on $d_{eff}^{-1.5}$, which showed good agreement with the exponent $d_{eff}^{-1.53}$ obtained form the simulation results. From the equation that shows the recombination velocity at the edge of the GB depletion region depends on the product of carrier velocity and the exponential of the GB potential, it is proposed that the dependence of $J_0 \sim d_{eff}^{-4.73}$ results from the carrier velocity that depends on the electric field in GB depletion region and the GB potential though the detailed relation was not revealed in this study. The critical effective grain size was explained as a grain size where the dominant process for the carrier transport to GB states changes from the diffusion to the electric field. The critical grain size was suggested as 450 nm from the grain size where the dependence J_0 on d_{eff} changes. The critical grain size was also calculated from the plot of the net carrier density in the grain interior. It was suggested as 300 ~ 450 nm from the grain size when the grain size is equal to the twice of the GB depletion region.

The illumination was turned out to decrease the GB potential by supplying enough carriers for the GB state and leading to a new steady state potential. The illumination effect decreases with increasing grain size since there are already enough carriers for GB states even without illumination when the grain size is large. The increasing density of GB trap states increases the GB potential as well as the GB depletion region.

The effect of GB orientation and the effect of the junction depletion region were studied by using GBs with single orientation (VGB and HGB) and the different CdS/CIS doping ratio. The cases with high doping ratio (HGB_H and VGB_H) were used to increase the junction depletion region in CIS layer and to investigate its effect on the GB orientation effect. The orientation of GBs affects each device performance parameter in a different manner. It was observed that VGB shows lower V_{OC} values than those of HGB for all grain sizes unless the depletion is large enough to include the GBs as in the cases of the high doping ratio. From this observation, it appears that the effect of GBs on V_{OC} appears is determined by the fraction of GBs in the junction depletion region where the recombination is enhanced due to the electric field in junction depletion region.

The HGB was proposed to act as a barrier to the transport of electrons from the observation of lower J_{SC} values in the case of HGB than those in the case of VGB. It is also observed that in the case of HGB, J_{SC} deceases rapidly when the grain size becomes small due to the increased recombination with the trapped holes at GBs. Also, the increase of J_{SC} for the cases with high doping ratio (HGB_H and VGB_H) is due to the decrease of the doping level in CIS layer that leads to the increased minority carrier current. The HGB_H, however, shows smaller J_{SC} when the grain size is small and the whole GB is included in the junction depletion region. This observation, again, shows that GB effect on device performance parameter is the largest when the GBs are present in the junction depletion region as in the case of V_{OC}.

For the most important device performance parameter, η as well as F.F., VGB shows lower values than HGB, which are mainly due to the lower V_{OC} values from the larger GB effect for the GBs in the junction depletion region. Also, with increased

junction depletion region, VGB_H shows lower η and F.F. from the decreased V_{OC} due to the reduction of doping level in CIS layer than VGB. For small grain sizes, however, HGB shows lower η and F.F. due to the rapid decrease of J_{SC} with negligible differences of V_{OC} between VGB and HGB. With larger junction depletion region, HGB_H and VGB_H show lower η and F.F. than VGB and HGB as more GBs are in the junction depletion region in the cases of VGB_H and HGB_H. This increased recombination current is also observed from larger J_0 values for the cases, HGB_H and VGB_H.

In summary, to obtain high efficiency, it appears that HGB is better when the grain size is large or the junction depletion is small. When the grain size is small or the junction depletion region is large, however, it is better to have VGB to obtain good performance.

LIST OF REFERENCES

Abu04 J.A.M. Abushama, S. Johnston, R. Noufi, K. Ramanathan, G. Teeter, and T. Moriarty, *Prog. Photovolt. Res. Appl.* **12**, 39 (2004)

Aru94 E. Arushanov, Ch. Loc, and E. Bucher, *Phys. Rev. B* **50(4)**, 2653 (1994)

Bau00 A. Bauknecht, S. Siebentritt, A. Gerhard, W. Harneit, S. Brehme, J. Albert, S. Rushworth, and M.Ch. Lux-Steiner, *Thin Solid Films* **361-362**, 426 (2000)

Beb72 H.B. Bebb and E.W. Williams, *Semiconductors and Semimetals in Transport and Optical Phenomena* (Academic Press, New York, 1972) p. 182

Bra00 D. Braunger, D. Hariskos, G. Bilger, U. Rau, and H.W. Schock, *Thin Solid Films* **361-362**, 161 (2000)

Car77 H.C. Card, and E. Yang, *IEEE Trans. Electron Devices* **ED-29**, 397 (1977)

Cas51 R. Castaining, *Ph.D. Thesis*, University of Paris (1951)

Cha54 D.M. Chapin, C.S. Fuller, and G.L. Pearson, *J. Appl. Phys.*, **25**, 676 (1954)

Cha96a C.H. Chang, A. Davydov, B.J. Stanbery, and T.J. Anderson, *The Conference Record of the 25th IEEE Photovoltaic Specialist Conference* 849 (IEEE, Piscataway, 1996)

Cha96b C.H. Chang, A. Davydov, B.J. Stanbery and T.J. Anderson, *Proc. 25th IEEE Photovoltaic Specialists Conference* New York: IEEE, 1996, p849.

Cha99 C.H. Chang, Dissertation, University of Florida, 1999

Cha03 C.H. Chang, S.H. Wei, J.W. Johnson, S.B. Zhang, N. Leyarovska, G. Bunker, and T.J. Anderson, *Phys. Rev. B* **68**, 054108 (2003)

Che90 Z. Chen, and L.C. Burton, *21st IEEE Photovoltaic Specialist Conference* 731 (1990)

Chi94 S. Chichibu, Y. Harada, M. Uchida, T. Wakiyama and S. Matsumoto, S. Shirakata, and S. Isomura, H. Higuchi, *J. Appl. Phys.* **76**, 3009 (1994)

Cli75 G. Cliff, and G.W. Lorimer, *J. Microscopy* **103**, 203 (1975)

Con55 E.M. Conwell, *Phys. Rev.* **98**, 1178 (1955)

Con97 M.A. Contreras, B. Egaas, P. Dippo, J. Webb, J. Granata, K. Ramanathan. S. Asher, A. Swartzlander, and R. Noufi, *26th IEEE PVSC*, 359 (1997)

Dea67 P.J. Dean, *Phys. Rev.*, **157**, 655 (1967)

DES96 DESSIS 3.0 Manual (ISE Integrated Systems Engineering AG, Zurich, Switzerland, 1996)

Edm96 S.A. Edmiston, G. Heiser, A.B. Sproul, and M.A. Green, *J. Appl. Phys.*, **80** (12), 6783 (1996)

Fon98 P. Fons, S. Niki, A. Yamada, and H. Oyanagi, *J. Appl. Phys.* **84**, 6926 (1998)

Fra56 F.C. Frank, and D. Turnball, *Phys. Rev.* **104**, 617 (1956)

Fra78 L.M. Fraas, *J. Appl. Phys.* **49** (2), 871 (1978)

Fri85 C.E. Fritts, *Lumiere Electr.*, **15**, 226 (1985)

Gho80 A.K. Ghosh, C. Fishman, and T. Feng, *J. Appl. Phys.* **51** (1), 446 (1980)

Gib80 P. Gibart, L. Goldstein, and J.L. Dormann, *Proc. 4th International Conference On Ternary and Multinary Compounds, Jpn. J. Appl. Phys.* **19-3**, 184 (1980)

Gis85 H.P. Gislason, Z.G. Wang, and B. Monemar, *J. Appl. Phys.*, **58** (1), 240 (1985)

Gra00 K. Granath, M. Bodegard, and L. Stolt, *Solar Energy Materials & Solar Cells* **60**, 279 (2000)

Gre96 M.A. Green, *J. Appl. Phys.* **80** (3), 1515 (1996)

Gre99 M.A. Green, K. Emery, K. Bücher, D.L. King, and S. Igari, *Prog. Photovolt.:Res. Appl.* **7**, 31 (1999)

Hal64 R.N. Hall, and J.H. Racette, *J. Appl. Phys.* **35**, 379 (1964)

Hay60 J.R. Haynes, *Phys. Rev. Lett.* **4**, 361 (1960)

Hol94 J. Holz, F. Karg, and H.V. Philipsborn, *Proc. 12th EC PVSEC*, 159 (1994)

Hön88 W. Hönle, G. Kühn, and U.C. Boehnke, Crystal Research and Technology, **23**, 1347 (1988)

Hor96 M. Hornung, *Ph.D. Thesis University of Freiburg* (Shaker-Verlag, Aachen,1996)

Hun50 C.S. Hung, and J.R. Gliessman, *Phys. Rev.* **79**, 726 (1950)

Ide03 M. Ider, Dissertation, University of Florida, 2003

Ish01 Y. Ishikawa, Y. Yamamoto, T. Hatayama, Y. Uraoka, and T. Fuyuki, *Jpn. J. Appl. Phys.*, **40**, 6783 (2001)

Iso80 S. Isomura, H. Kaneko, S. Tomioka, I. Nakatani, and K. Masumoto, *Jpn. J. Appl. Phys.*, **19**, 23 (1980)

Jit98 H. Jitsukawa, H. Matsushita, and T. Takizawa, *J. Cryst. Growth* **186**, 587 (1998)

Kar93 F. Karg, V. Probst, H. Harms, J. Rimmasch, W. Riedl, J. Kotschy, J. Holt, R. Trichler, O. Eibl, A. Mitwalsky, and A. Kiendl, *23th IEEE PVSC*, 441 (1993)

Ker02 L.L. Kerr, S. Kincal, M. Ider, S. Yoon, T.J. Anderson, *29th IEEE PVSC*, 676 (2002)

Key97 B.M. Keyes, F. Hasson, P. Dippo, A. Balcioglu, and F. Abulfotuh, *26th IEEE PVSC*, 479 (1997)

Kel84 R. Klenk, T. Walter, H.W. Schock, and D. Cahen, *Solid State Phenom.* **37-38**, 509 (1984)

Kim01a M. Kimura, S. Inoue, T. Shimoda, and T. Sameshima, *Jpn. J. Appl. Phys.*, **40**, L97 (2001)

Kim01b M. Kimura, S. Inoue, T. Shimoda, and T. Sameshima, *Jpn. J. Appl. Phys.*, **40**, 49 (2001)

Kle93 R. Klenk, T. Walter, H.W. Schock, and David Cahen, *Advanced Materials* **5**, 114 (1993)

Kur87 K. Kuriyama, and F. Nakamura, *Phys. Rev. B* **36**, 4449 (1987)

Lia02 D. Liao, and A. Rockett, *J. Appl. Phys.* **91**, 1978 (2002)

Man79 A. Manoogian, and A. Leclerc, *Phys. Status Solidi B.* **92**, K23 (1979)

Mar95 I.V. Markov, *Crystal Growth for Beginners* (World Scientific, Singapore, 1995), p. 78.

Mar04 M. Symko-Davies, *Progress Report in High Performance Photovoltaics* (2004)

Mat01 T. Matsui, T. Yamazaki, A. Nagatani, K. Kino, H. Takakura, and Y. Hamakawa, *Solar Energy Materials & Solar Cells* **65**, 87 (2001)

Mic80 R.A. Mickelsen, J.M. Stewart, and W.S. Chen, *Technical Report* (Boeing Aerospace Co., Seattle, WA, 1980)

Mur91 M.R. Murti, and K.V. Reddy, *J. Appl. Phys.* **70**, 3683 (1991)

Neu90 H. Neumann, and R.D. Tomlinson, *Solar Cells* **28**, 301 (1990)

Neu02 W. Neu, A. Kress, W. Jooss, P. Fath, and E. Bucher, *Solar Energy Materials & Solar cells* **74**, 139 (2002)

Nik94 S. Niki, Y. Makita, A. Yamada, A. Obara, and S. Misawa, O. Igarashi, K. Aoki and N. Kutsuwada, *Jpn. J. Appl. Phys.* **33**, L500 (1994)

Nik95 S. Niki, H. Shibata, P.J. Fons, A. Yamada, A. Obara, and Y. Makita, T. Kurafuji, S. Chichibu and H. Nakanishi, *App. Phys. Lett.* **67**, 1289 (1995)

Nik99 S. Niki, P. Fons, A. Yamada, Y. Lacroix, H. Shibata, and H. Oyanagi, *J. Appl. Phys.* **74**, 1630 (1999)

Nik01 S. Niki, R. Suzuki, S. Ishibashi, T. Ohdaira, P.J. Fons, A. Yamada, H. Oyanagi, T. Wada, R. Kimura, and T. Nakada, *Thin Solid Films* **387**, 129 (2001)

Nik02 S. Niki, A. Yamada, R. Hunger, P.J. Fons, K. Iwata, K. Matsubara, A. Nishio, and H. Nakanishi, *Journal of Crystal Growth* **237-239**, 1993 (2002)

Nil97 D.W. Niles, K. Ramanathan, F. Hasoon, R. Noufi, B.J. Tielsch, and J.E. Fulghum, *J. Vac. Sci. Technol. A* **15**, 3044 (1997)

Nil99 D.W. Niles, and M. Al-Jassim, *J. Vac. Sci. Technol. A* **17**, 291 (1999)

Oua84 J. Oualid, C.M. Singal, J. Dugas, J.P. Crest, and H. Amzil, *J. Appl. Phys.* **55** (4), 1195 (1984)

Pal67 L.S. Palatnik, and I.K. Belova, *IZvestiya Akademii Nauk SSSR, Neorganicheskie Materialy* **12**, 2194 (1967)

Pal93 J. Palm, *J. Appl. Phys.* **74**, 1169 (1993)

Pan71 J.I. Pankove, *Optical Processes in Semiconductors* (Dover, New York, 1971), p. 12.

Ram03 K. Ramanathan, M.A. Contreras, C.L. Perkins, S. Asher, F.S. Hasoon, J. Keane, D. Young, M. Romero, W. Metzger, R. Noufi, and A. Duda, *Prog. Photovolt. Res. Appl.,* **11**, 225 (2003)

Rau96 U. Rau, M. Schmitt, D. Hilburger, F. Engelhardt, O. Seifert, and J. Parisi, *25th IEEE Photovoltaic Specialist Conference* 1005 (1996)

Rav01 B. Ravel, *J. Synchrotron Rad.* **8**, 314 (2001)

Ray54 D.C. Raynolds, G. Leies, L.L. Antes, and R.E. Marburger, *Phys. Rev.* **96**, 533 (1954)

Rin83 C. Rincón, J. González, and G. Sanchez Pérez, *J. Appl. Phys.* **54**, 6634 (1983)

Roc94 A. Rockett, F. Abou-Elfotouh, D. Albin, M. Bode, J. Ermer, R. Klenk, T. Lommasson, T.W.F. Russell, R.D. Tomlinson, J. Tuttle, L. Stolt, T. Walter, and T.M. Peterson, *Thin Solid Films* **237**, 1 (1994)

Roc00 A. Rockett, *Thin Solid Films* **361-362**, 330 (2000)

Ruc94 M. Ruckh, D. Schmid, M. Kaiser, R. Schaffler, T. Walter, and H.W. Schock, *1st WEPEC*, Hawaii (1994)

Sch28 W. Schottky, W. Deutschmann, *Phys. Z.* **30**, 839 (1928)

Sch30 W. Schottky, *Phys. Z.* **11**, 460 (1930)

Sch95 J.H. Schön, and E. Bücher, *App. Phys. Lett.* **67**, 1289 (1995)

Sch96 J.H. Schön, F.P. Baumgartner, E. Arushanov, H. Riazi-Nejad, C. Kloc, and E. Bucher, *J. Appl. Phys.* **79**(9), 6961 (1996)

Sch97a J.H. Schön, E. Arushanov, C. Kloc, and E. Bucher, *J. Appl. Phys.* **81**(9), 6205 (1997)

Sch97b D.J. Schroeder, and A. Rockett, *J. Appl. Phys.* **82** (10), 4982 (1997)

Sch98 J.H. Schön, and E. Bucher, *Appl. Phys. Lett.* **73**, 211 (1998)

Sch98 D.J. Schroeder, J.L. Hernandez, G.D. Berry, and A. Rockett, *J. Appl. Phys.* **83**(3), 1519 (1998)

Sch99 J.H. Schön, and E. Bucher, *Solar Energy Materials & Solar Cells* **57**, 229 (1999)

Sch00a D.J. Schröeder, E. Arushanov, and E. Bucher, *Solar Energy Materials and Solar Cells* **61**, 417 (2000)

Sch00b J.H. Schön, *J. Phys. D : Appl. Phys.* **33**, 286 (2000)

Sch00c J.H. Schön, Ch. Kloc, and E. Bucher, *Thin Solid Films* **361-362**, 411 (2000)

Sea81 C.H. Seager, *J. Appl. Phys.* **52** (6), 3960 (1981)

Sha85 A.V. Shahidi, I. Shih, T. Araki and C.H. Champness, *J. Electron. Mater.* **14**, 297 (1985)

Shi93 S. Shirakata, S. Chichibu, R. Sudo, A. Ogawa, S. Matsumodo and S. Isomura, *Jpn. J. Appl. Phys.* **32**, L1304 (1993)

Sho52 W. Shockley, T. Read and R.N. Hall, *Phys. Rev. Lett.* **87**, 835 (1952)

Sit60 J.R. Sites and R.E. Hollingsworth, *Solar Cells.* **4**, 361 (1960)

Slu93 P. Sluis, *J. Phys.D* **26** (4A), A188 (1993)

Smi73 W. Smith, *Nature* **20**, Feb. (1973)

Spi 74 H.W. Spiess, U. Haeberln, G. Brandt, A. Räuber, and J. Schneider, Phys. Status Solidi B 62: 183, 1974.

Sta01 B. J. Stanbery, *Ph.D. Thesis*, University of Florida (2001)

Sta02 B.J. Stanbery, S. Kincal and S. Kim, C.H. Chang, S.P. Ahrenkiel, G. Lippold, H. Neumann, T.J. Anderson and O.D. Crisalle, *J. Appl. Phys.* **91**, 3598 (2002)

Sto93 L. Stolt, J. Hedstrom, J. Kessler, M. Ruckh, K.O. Velthaus and H.W. Schock, *Appl. Phys. Lett.* **62**, 597 (1993)

Su98 D.S. Su, W. Neumann, R. Hunger, P. Schubert-Bischoff, M. Giersig, H.J. Lewerenz, R. Scheer and E Zeitler, *App. Phys. Lett.* **73**, 785 (1998)

Sur05 T. Surek, *J. Cryst. Growth*, (2005), **275**, 292 (2005)

Sze81 S.M. Sze, *Physics of Semiconductor Devices*, New York: Wiley & Sons, 1981, p. 790.

Tan92 H. Tanino, *Phys. Rev. B* **45**, 13323 (1992)

Tel72 B. Tell, J.L. Shay and H.M. Kasper, *J. Appl. Phys.* **43**, 2469 (1972)

Tiw94 A.N. Tiwari, S. Blunier, K. Kessler, V. Zelezny and H. Zogg, *App. Phys. Lett.* **65**, 2299 (1994)

Tu92 K. Tu, J.W. Mayer, and L.C. Feldman, *Electronic Thin Film Science for Electrical Engineers and Materials Scientists*, New York: Macmillan Publishing Company, 1992.

Tut95 J.R. Tuttle, M. Contreras, M.H. Bode, D. Niles, D.S. Albin, R. Matson, A.M. Gabor, A. Tennant, A. Duda, and R. Noufi, *J. Appl. Phys.* 77, 153 (1995)

Wad97 T. Wada, N. Kohara, T. Negami and M. Nishitani, *J. Mater. Res.* **12**, 1456 (1997)

Wan85 Z.G. Wang, H.P. Gislason and B. Monemar, *J. Appl. Phys.* **58**, 230 (1985)

Was86 S. M. Wasim, *Solar Cells* **16**, 289 (1986)

Wei88 I. Weinberg, C.K. Swartz, R.E. Hart and T.J. Coutts, *Proc. 20th IEEE Photovoltaic Specialists Conference* New York: IEEE, 1988, p893.

Wei92 S.H. Wei, L.G. Ferreira and A. Zunger, *Phys. Rev. B* **45**, 2533 (1992)

Wei98 S.H. Wei, S.B. Zhang and A. Zunger, *Appl. Phys. Lett.* **72**, 3199 (1998)

Wei99 Su-Huai Wei, S.B. Zhang and A. Zunger, *J. Appl. Phys.* **85** (10), 7214 (1999)

Wol89 C. Wolfe, N. Holonyak, and G. Stillman, *Physical Properties of Semiconductors,*: Prentice Hall, 1989, Chapter 2

Yam96 A. Yamada, Y. Makita, S. Niki, A. Obara, P. Fons and H. Shibata, *J. Appl. Phys.* **79**, 4318 (1996)

Yam97 A. Yamada, P. Fons, S. Niki, H. Shibata, A. Obara, Y. Makita and H. Oyanagi, *J. Appl. Phys.* **81**(6), 2794 (1997)

Yos00 K. Yoshino, H. Yokoyama, K. Maeda and T. Ikari, *Journal of Crystal Growth* **211**, 476 (2000)

Zha98 S.B. Zhang, Su-Huai Wei and A. Zunger, *Phys. Rev. B* **57**, 9642 (1998)

Zha02 S.B. Zhang and S. H. Wei, *Phys. Rev. B* **65**, 081402(R) (2002)

BIOGRAPHICAL SKETCH

Seokhyun Yoon was born in Seoul, Korea, on October 20, 1968, to Gumja Park and Sungjoong Yoon. He received his Bachelor of Science degree from the department of chemical engineering, Seoul National University in February 1991. He joined the rheology and processing labs in the department of chemical engineering, Seoul National University in 1991 for his master's study. His master's research, from 1991 to 1993, involved the study of the dynamics of the dilute polymer solution by using the elastic dumbbell model. In his research, he studied the rheological behavior of dilute polymer solutions under simple shear flow and simple elongation flow by representing polymers as elastic dumbbells. After receiving his master's degree in 1993, he joined LG Chemical Research Park (Taejon, Korea) as a research engineer. While employed at LG, he worked in many areas including the plastic extrusion process, simulation of momentum and heat transfer for the design of extrusion dies, heat transfer for the design of plastic automotive parts, and the experimental and simulation study of the plastic blow-molding process. He was also involved in developing polarizing film based on the PVA material for thin film transistor liquid crystal display and he played a key role in the development from laboratory experiment to the launching of the pilot plant. He left LG to pursue a doctorate in chemical engineering from the University of Florida in 1999.

I certify that I have read this study and that in my opinion it conforms to acceptable standards of scholarly presentation and is fully adequate, in scope and quality, as a dissertation for the degree of Doctor of Philosophy.

Timothy J. Anderson, Chairman
Professor of Chemical Engineering

I certify that I have read this study and that in my opinion it conforms to acceptable standards of scholarly presentation and is fully adequate, in scope and quality, as a dissertation for the degree of Doctor of Philosophy.

Paul Holloway
Distinguished Professor of Materials Science and Engineering

I certify that I have read this study and that in my opinion it conforms to acceptable standards of scholarly presentation and is fully adequate, in scope and quality, as a dissertation for the degree of Doctor of Philosophy.

Fan Ren
Professor of Chemical Engineering

I certify that I have read this study and that in my opinion it conforms to acceptable standards of scholarly presentation and is fully adequate, in scope and quality, as a dissertation for the degree of Doctor of Philosophy.

Oscar D. Crisalle
Professor of Chemical Engineering

I certify that I have read this study and that in my opinion it conforms to acceptable standards of scholarly presentation and is fully adequate, in scope and quality, as a dissertation for the degree of Doctor of Philosophy.

Sheng S. Li
Professor of Electrical and Computer Engineering

This dissertation was submitted to the Graduate Faculty of the College of Engineering and to the Graduate School and was accepted as partial fulfillment of the requirements for the degree of Doctor of Philosophy.

May 2005

Pramod P. Khargonekar
Dean, College of Engineering

Kenneth Gerhardt
Dean, Graduate School